Edith Cowan University

Research Online

Theses: Doctorates and Masters

Theses

2002

Design and analysis of optical layouts for free space optical switching

Kung-meng Lo
Edith Cowan University

Follow this and additional works at: https://ro.ecu.edu.au/theses

 Part of the Electrical and Computer Engineering Commons

Recommended Citation

Lo, K. (2002). *Design and analysis of optical layouts for free space optical switching.* https://ro.ecu.edu.au/theses/1645

This Thesis is posted at Research Online.
https://ro.ecu.edu.au/theses/1645

Edith Cowan University

Copyright Warning

You may print or download ONE copy of this document for the purpose of your own research or study.

The University does not authorize you to copy, communicate or otherwise make available electronically to any other person any copyright material contained on this site.

You are reminded of the following:

- Copyright owners are entitled to take legal action against persons who infringe their copyright.

- A reproduction of material that is protected by copyright may be a copyright infringement. Where the reproduction of such material is done without attribution of authorship, with false attribution of authorship or the authorship is treated in a derogatory manner, this may be a breach of the author's moral rights contained in Part IX of the Copyright Act 1968 (Cth).

- Courts have the power to impose a wide range of civil and criminal sanctions for infringement of copyright, infringement of moral rights and other offences under the Copyright Act 1968 (Cth). Higher penalties may apply, and higher damages may be awarded, for offences and infringements involving the conversion of material into digital or electronic form.

EDITH COWAN UNIVERSITY
LIBRARY

Design and Analysis of Optical Layouts for Free Space Optical Switching

By

Kung-meng Lo

A thesis submitted for the degree of
Master of Engineering Science
at
School of Engineering and Mathematics
Edith Cowan University

Principal Supervisor: Dr. Daryoush Habibi

Co-Supervisor: Prof. Rafie Mavaddat

Sep 2002

USE OF THESIS

The Use of Thesis statement is not included in this version of the thesis.

Declaration

I certify that this thesis does not incorporate without acknowledgement any material previously submitted for a degree or diploma in any institution of higher education; and that to the best of my knowledge and belief it does not contain any material previously published or written by another person except where due reference is made in the text.

To My Wife and Son

Acknowledgements

First and foremost, I would like to express my sincerest gratitude to my principal supervisor Dr. Daryoush Habibi who has been the main source of inspiration and motivation behind my Master, and co-supervisor Professor Rafie Mavaddat, for his encouragement, advice, open-mindedness and suggestions to my work. I would like to thank them particularly for the independence they gave me the freedom to explore, discover, and experiment, so ensuring my master research was fulfilling, stimulating and more enjoyable.

I would like to thank my parents Yunghsin Lo and Chuntsu Shin Lo, my wife Shwuhuey Tsai and my son Brendan Lo for their love, support and encouragement they have shown me throughout my time at ECU.

Many thanks for school staff at ECU: Pr. Kamran Eshraghian, Dr. Kamal E. Alameh, and Dr. Wlodzimierz Gornisiewicz for their kind assistance and useful discussion. I would also like to thank Guoqiang, Selam, Mehrdad, and Rong who made the past two years so enjoyable, exciting, fun, and who have left me with so many memories.

Finally, I would like to thank the Postgraduate School and the School of Engineering and Mathematics at Edith Cowan University for providing a friendly and creative environment.

This work would not have been possible without the financial support of the following organizations:

- Faculty of Communications, Health & Science, ECU, through the postgraduate student research scholarship.

- Faculty of Communications, Health & Science, ECU, through the special postgraduate research scholarship.

Abstract

The Intelligent Reconfigurable Optical Switch (IROS) is an $N \times N$ optical switch that uses two reflective Liquid Crystal (LC) Spatial Light Modulators (SLM) in a "Z" configuration to steer the incoming beams from the input ports to the designated output ports. Currently, the maximum steering capacity of practical SLM is limited to few degrees. For a dense optical switch, this makes the optical path between the input and output fiber ports relatively long. When a Gaussian beam is switched from an input fiber port to an output fiber port in a long free space interconnection topology, the beam's illumination undergoes significant divergence, which contributes to power loss and induces cross talk on the output ports. A possible method to minimize these problems is to design an optical system to collimate divergent beams.

The aim of this research is to provide and evaluate a number of design alternatives for the optical systems used to route Gaussian beams from an input fiber array to the first SLM. In this thesis, a microlens array is designed and four possible lens combinations are investigated. Due to explore the beam performances and analyze the aberration effects, one possible layout is selected. And then the selected optical system is optimized. The results show that the optimized optical system has achieved the required beam performance criteria of alignment, collimation, magnification and low aberrations on the first SLM. Finally, the Modulation Transfer Function (MTF) is introduced and verified that the performance of the optimized optical system is achieved the diffraction limited on the first SLM.

Keywords

Optical switch; phase holograms; spatial light modulator; Gaussian beam; aberration; Modulation Transfer Function (MTF); diffraction limited

Contents

List of Tables

List of Figures

Chapter 1

Introduction

The continuous growth in the global data traffic and the proliferation of corporate data networks has created an unprecedented demand for bandwidth. In order to satisfy the demands for wide bandwidth, the use of multiple wavelengths in the same optical fiber has been introduced. Optical fiber is replacing wire as the information transmission medium, and many countries are installing substantial numbers of single-mode fiber telecommunication links [1~3].

The development of optical networks requires dynamic wavelength routing that can reconfigure the network while maintaining its non-blocking nature. Therefore, optical signals on network can be freely set up and taken down as needed, without having to be statically provisioned. This functionality is provided by optical crossconnect (OXC) [4-7]. Moreover, OXC is a useful network element to handle complex network topologies and large numbers of wavelengths, particularly at hub locations handling a large amount of traffic. Thus, OXC plays an important role as optical networks become more agile [8].

1.1 Optical Crossconnect (OXC) Overview

An OXC enables inbound optical signals to be switched to output ports at optical carrier-level speeds and with similar granularity. Figure 1.1 shows the general configuration of the prototype OXC node [9]. The prototype system consists mainly of optical switches (OSWs), wavelength multiplexers (WMUXs), demultiplexers (WDMXs), optical pre-amplifiers (Pre-OAs) and post-amplifiers (Post-OAs) [5]. The optical switch is the core of an OXC. If the insertion loss of the optical switch is large, optical amplifiers (OAs) will be required to compensate for the loss inside the node. If the loss variation at each switch port is large, the optical receiver (OR) at the termination or regenerating nodes cannot receive the optical signals, as the dynamic range of the OR is exceeded. If the crosstalk of the optical switch is large, optical signals will be disturbed by other optical signals. For these reasons, low loss, small loss variation, and low crosstalk are important considerations in the design of optical switches, which are used in constructing large-capacity OXC nodes. This approach allows any input channel to be routed to any output channel. This characteristic is known as “fully non-blocking” architecture.

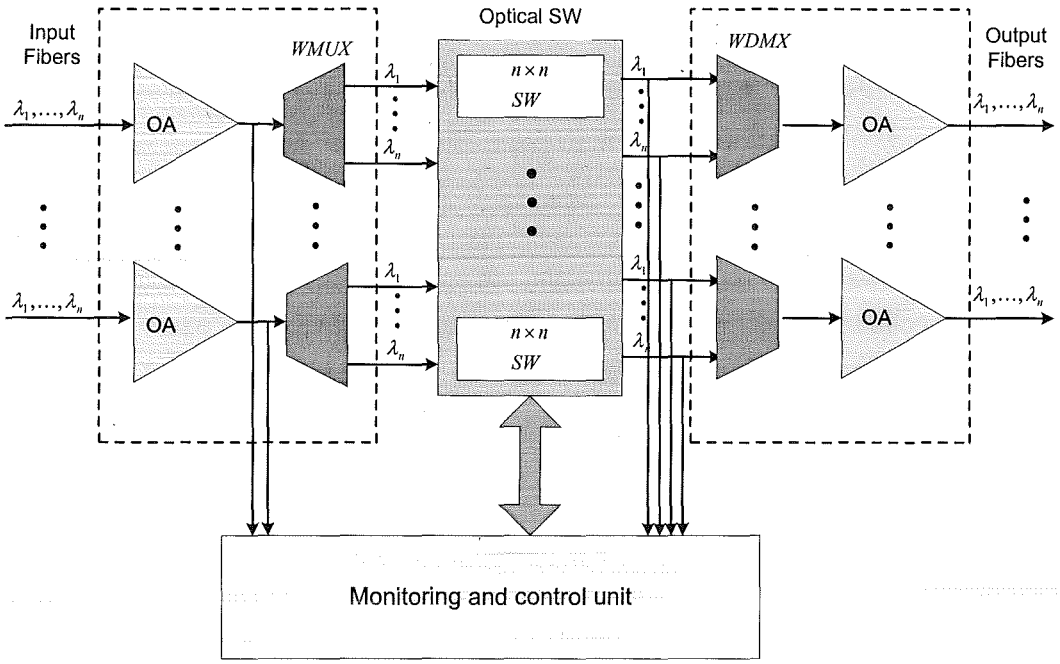

Figure 1.1: General configurations of an OXC [9]

Optical switches are the core of OXCs. Optical switches are used in optical networks for a variety of applications [4]. One application of optical switches is in the provision of lightpaths. Switches are utilized inside wavelength crossconnects to reconfigure them to support new ligthpaths in this application. Switches with millisecond switching times are satisfactory for this application. However, the challenge here is to realize a large switch size. Another application is that of protection switching. Switches are used to switch the traffic stream from a primary fiber onto another fiber in case the primary fiber fails. The entire operation (switching time) required is in the order of a few milliseconds. This includes the time to detect the failure, communicate the failure to the appropriate network elements handling the switching, and the actual switching time. Based on different types of protection switching and their schemes, the required number of switch ports can be from two ports to several hundreds or even a thousand. Another use for optical switches is in high-speed optical packet-switched networks. Here switches are used to switch signals on a packet-by-packet basis. The switching time is smaller than a packet duration, so that the efficient operation is of the order of a few nanoseconds. Yet another application for optical switches is that of external modulators to turn on and off the data in front of a laser source. In this application, the switching time must be a small fraction of the bit duration, so the switching time has the order of about 10 ps. Different applications require different switching times and different number of ports as listed in Table 1.1 [4].

Table 1.1: Applications for optical switches and their switching time and port count requirements [4].

Application	Switch time required	Number of ports
Provisioning	1 – 10 ms	> 1000
Protection switching	1 – 10 ms	2 - 1000
Packet switching	1 ns	> 100
External modulation	10 ps	1

Currently, several different technologies are implementing such optical switches. OXC is expected to make it possible to realize powerful provisioning, reconfiguration, and path restoration functions in photonic networks. Optical cross connection may be accomplished in two ways [5]:

Hybrid approach: Convert optically encoded data streams in an optical fiber into electronic data by means of a photo-detector; and then use electronic cross-connection technology to switch between electronic data streams, and finally convert electronic data streams back into optical data in an output fiber.

All-optical approach: Cross-connect optical channels directly in the photonic domain. Since the actual light beams from the input ports are directed (or steered) into output ports, this approach is also called "optically-transparent" switching.

Both approaches have inherent strengths to make them suitable for differing requirements in an optical network. In general, it is fair to expect that the hybrid approach would be suitable for low bit rate communication links. The drawback of hybrid approach is that it cannot cope with ultra-high bandwidth; and the optic-electronic-optic conversion at each node is cumbersome. Furthermore, the speed of the electronic circuitry becomes the bottleneck. However, an all-optical approach can be used in a high bandwidth, scalable with low crosstalk, and large number ports of cross-connecting fabrics. In addition, as the bandwidth of optical networks increases, electronic switches prove to be less feasible, and optically transparent switches become more attractive. The literature reveals two distinct all-optical crossconnect approaches [10]:

- Optical solid-state devices [11-14]
- Free-space optical switching [4,15-21]

Solid-state devices are semiconductor directional wave-guided couplers. Couplers, as the name suggests, are used to combine and split signals in an optical network. They can be categorized into two types: Mach-Zehnder interferometers (MZI) and directional couplers

(DC). These devices can selectively change one of their optical properties on a path upon the application of a control signal. The optical property may be polarization, propagation constant, absorption, or index of refraction, depending on the type of material. These optical properties may change upon the application of heat, light, mechanical pressure, electric current, or an electric field (voltage) [5]. For example, the refractive index of *Lithium Niobate* ($LiNbO_3$) changes when an electric field is applied across it. Advances in $LiNbO_3$ modulator device technology have enabled stable operation over temperature, very low bias-voltage drift rates, and bias-free devices [11]. However the change in refractive index is small. Therefore in order to achieve sufficient modulation, a large voltage or a long wave-guide is needed [12]. Another material is *Indium Gallium Arsenide Phosphide* ($InGaAsP$), which is applied in integrated optics (IO) planar waveguide elelctrooptic Mach-Zehnder interferometer (MZI) [13]. This material exhibits a fast electro-optic response to applied voltage. However, the crystal is anisotropic, hence the drawbacks are difficulties in achieving polarization insensitive, limited expandability, and high loss in the wave-guide at telecommunication wavelengths [14].

A free-space optical switch is a switch that has a matrix of input beams facing a matrix of fibers and one of the source beams and a receiving fiber would be steered so that they faced each other to achieve connectivity in space. Upon redirecting the source (by a small degree) to face another fiber space, switching would be accomplished. The key performance parameters of free-space optical switches are insertion loss, crosstalk, repeatability, polarization dependant loss, and switching time. Typically, two main mechanisms to reconfigurable beam steering in this class of device are *mechanical steering* and *holographic diffraction* [10].

Micro-electro-mechanical system (MEMS) [15-21] is a type of mechanical steering switch. There are two architectures in MEMS switches: *Matrix Switches* (often known as 2D switching), i.e., Free-Space Micromachined Optical Switch (FS-MOS) and *Beam-steering Optical Switches* (3D switching), eg. Lucent LambdaRouter.

In 2D switching a square array of $N \times N$ mirrors is used to couple light from a linear array of N fibers on one side of the square to a second linear array of N fibers on an adjacent side of square. It is designed such that only one of *N* mirrors on the path of the beam is active, the rest are folded down of the light's way. Mirror control for these 2D switches is binary (on or off) and thus straightforward, but the trade-off for this simplicity is optical loss. As the path length grows linearly with N, the number of ports, the optical loss also grows rapidly due to the Gaussian divergent nature of light. Therefore, 2D architectures are impractical beyond 32 inputs and 32 output ports [15-17].

3D switching makes use of 3D space as an interconnection region, allowing scalability far beyond 32 ports with acceptable optical losses (< 10 dB). The system uses a pair of mirror-arrays between input and output ports. The first set of mirror array is to redirect each input beam towards the second set of mirror array, which are the output mirrors. The output mirrors align their incoming beams to assigned output fibers [18]. In this architecture, there is a dedicated movable mirror for each input and each output. Each mirror operates in an analog mode (rather than binary). Thus the virtue of this architecture allows the optical path length to scale only as $\sqrt{N}$ instead of N. Therefore, port counts of several hundred are achievable with low loss. Recently, Lucent LambdaRouter, which is based on Bell Labs' 3D MEMS technology, has assembled a switch of 256 X 256 ports. The average loss of this switch is 1.25 dB [21]. Currently, there are some challenges for 3D MEMS switches, especially in fabricating and packaging large array of elements, as explained below [19-21]:

- Mechanical and Optical reliability issues: The strict requirements for a MEMS mirror system can be characterized by the mirror quality, the mirror spring constant, and the damping coefficient. The qualities of the mirror, such as its reflectivity, surface flatness, thickness uniformity and intrinsic stresses have a critical impact for 3D MEMS switches. The mirror spring constant measures the endurance of the mirror's spring due to the impact of constant twisting and bending. The damping coefficient, on the other hand, is a measure of the switch's speed in achieving equilibrium in a new mirror position.

- Optical packaging issue: MEMS requires thousand of micro-mirrors, lenses and fibers, which align to each other with tolerances in the order of microns and hundreds of micro-radians. This multi-element body must endure thermal cycles, shock, and vibration during shipping and operation.

An alternative approach, potentially capable of realizing large dimension all optical switches, uses holographic optical beam reflectors, which are based on multiple-phase liquid crystal spatial light modulators (LC-SLMs) [22-26]. SLMs have been utilized in realizing $N \times M$ optical switched since the late 1980's. The technologies of LC-SLMs have the advantage of avoiding the difficulties of fabricating and packaging the large array of microelements like MEMS. Moreover, recent advances in liquid crystal (LC) materials and VLSI technology have enabled the development of multi-phase SLMs that can perform high-resolution, and dynamic optical beam positioning in the 1550 nm optical communication window [27]. These attractive features can effectively be used to achieve high-port-count data-rate-independent optical switches.

1.2 Liquid Crystal Spatial Light Modulators (LC-SLM)

Light modulation with liquid crystals is accomplished by applying an electric field across a liquid crystal layer. A light propagating through an anisotropic liquid crystal material experiences a refractive index that is a function of the applied voltage [28]. Driving an LC material placed between two polarizers can lead to intensity and/or phase modulation for an incident light beam. A LC-SLM is an array of LC cells whose crystallographic orientations are independently addressed to create a pixilated holographic diffraction grating plate [29]. There are two types of LC-SLMs: transmissive and reflective. In transmissive LC-SLMs, the liquid crystal layer is sandwiched between two transparent electrodes. The application of a voltage between the electrodes induces a phase shift in that layer [30]. This is repeated periodically across a pixel block with the intent of forming the periodic phase profile characteristic of a grating. The operation of a reflective SLM is similar to that of a transmissive SLM, however, one of the electrodes of the reflective SLM is a high-reflectivity mirror. The advantage of a reflective SLM is that it can be easily integrated with silicon VLSI circuitry, for addressing and driving the LC cells [31-32]. Usually, Indium-Tin Oxide (ITO) is used as the transparent electrode, and evaporated aluminum is used as reflective electrode. The ITO layer is generally grounded and a voltage is applied at the reflective electrode by the VLSI circuit below the LC layer. A typical cell of a reflective SLM is shown in Figure 1.2 [33].

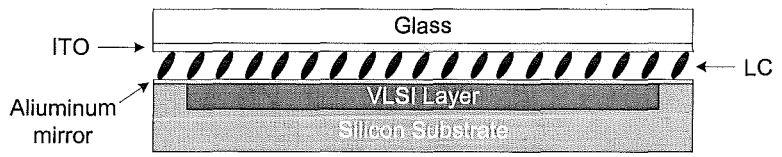

Figure 1.2: A typical LC cell of a reflective SLM [33].

Note that, future optical networks will require optical components, which are polarization insensitive. Therefore, the LC-SLM, being a key element in dynamic optical component architectures, is required to be polarization insensitive. The advances in LC materials and layer thickness control have recently solved this stringent requirement [34]. Incorporation of a thin quarter-wave-plate layer between the LC and the aluminum mirror accomplishes a polarization-insensitive multi-phase-level LC-SLMs [35].

An LC-SLM can steer a collimated beam with very high efficiency by applying an appropriate virtual blazed phase grating on the top of the VLSI chip. Figure 1.3 shows the principle of beam steering for a reflective pixilated SLM, where only a stepped blazed phase grating can be realized [33].

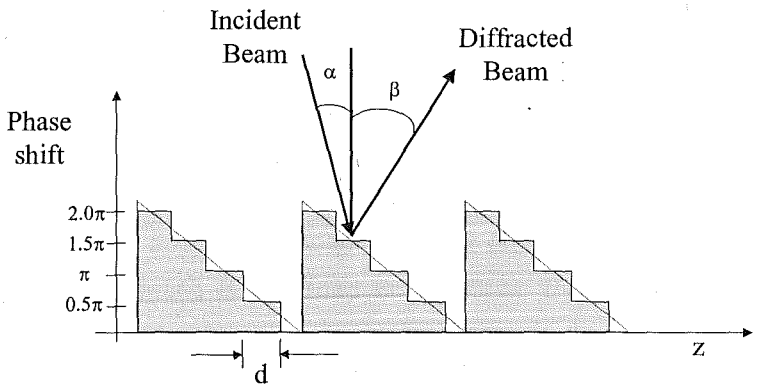

Figure 1.3: 4-phase stepped blazed grating structure [33].

This slightly reduces the first-order diffraction efficiency and induces additional higher diffraction orders. The relationship between the incidence and diffraction angles of a blazed grating on a M -phase SLM in is given by [36]

$$\lambda = M \cdot d\ (\sin\alpha + \sin\beta)$$

where, λ is the wavelength of the light and *d* is the pixel size. For example, a 4 - phase SLM having a pixel size of 10.8 *mm* can steer a 1550 nm laser beam by a maximum angle of 2°. The maximum diffraction efficiency of a SLM depends on the number of discrete phase levels that VLSI circuitry can implement in the given area. The theoretical maximum diffraction efficiency is given by [37]:

$$\eta = \mathrm{sinc}^2\left(\frac{\pi n}{m}\right)$$

where m is the number of phase levels, $n = gm + 1$ is the diffraction order ($n = 1$ is the desired order), and g is an integer. Thus, an SLM with binary phase levels can have a maximum diffraction efficiency of 40.5%, while four phase levels allow for efficiency up to 81%. In an LC-based optical switch, the higher diffraction orders are usually unwanted crosstalk, which must be attenuated or properly routed outside the output ports to maintain a high signal-to-crosstalk performance. The fundamental figure of merit for such devices depends on how well the grating can be realized by the application of an electric field. Ideally, in its fully active state, the switchable SLM grating must display low loss (< 0.3 dB insertion loss), low polarization dependence (< 0.2 dB polarization dependent loss) and other characteristics that approach those of high performance grating plates [33]. In its totally inactive state, the grating will ideally act as a low loss mirror. Fast switching speed (< 10 ms) and low driving voltage (< 5 V) are also important, which depend on

future advances in LC materials to create configurations that are compact, polarization insensitive, and low loss.

A typical structure for a $1 \times N$ LC-SLM optical switch is shown in Figure 1.4. In this structure, a lens is used to convert light emerging from an input optical fiber into a collimated beam with an appropriate beam diameter on the SLM. Then, an appropriate holographic diffraction grating is uploaded on the SLM. By changing the pitch of the blazed grating, the collimated beam is steered to a desired direction. After reflection and passing through the lens again, the steered collimated beam is focused and couples into an output fiber port.

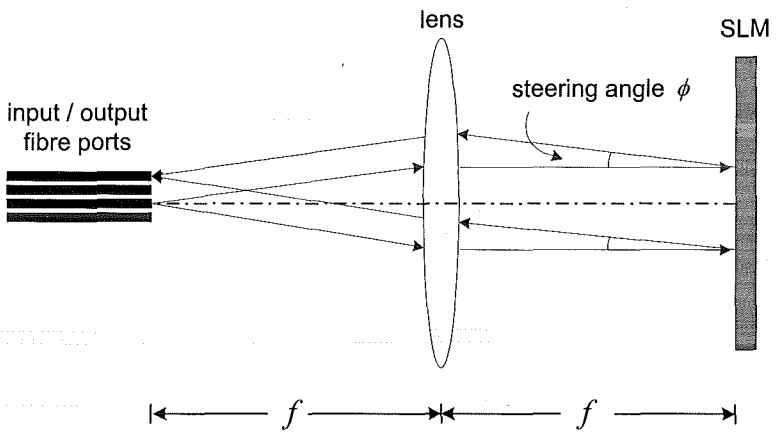

Figure 1.4: A typical 1 x N LC-SLM optical switch.

One important consideration in this switching structure is that the lens converts light with an adequate collimated beam size on modulators. There are some issues related to the divergent nature of Gaussian beam and optical noise (we refer to it as an aberration effect on the image plane) resulting from the lens.

Another important consideration in this switching structure is the output fiber coupling efficiency, which can be described by an overlap integral between the propagating modes in the fiber and the optical field pattern arriving at the fiber end. The coupling efficiency is therefore very sensitive to the incident angle (phase profile) as well as the position of the incident beam [38]. This places a limit on the maximum number of output ports of the switch. A 1×16 LC-based optical switch with 8 dB insertion loss and less than –20 dB crosstalk has been reported, and 1×32 switches are practically achievable [39].

The considerations mentioned above are related to the lens design. Actually, these two issues can be resolved to some extent by using proper optical components instead of

only one single lens. Typically, the variety of lenses or mirrors can be chosen and combined to achieve low loss and high port counts, as we desire in optical networks.

1.3 Optical elements applied in Free Space Interconnection

Typically, light can be treated as an *image* shifting in free space interconnection [40,41]. There are two issues that need to be addressed, if we utilize an optical system in free space interconnection. This is because these effects can be accumulated by image aberrations, beam's misaligned or defects of optical component. First, does this optical system need to focus or un-focus light on the image plane? And second, how can one design an optical system to reduce the power loss and aberration on the image plane? The first issue was addressed by F. B. McCormick in his Free-Space Interconnection Techniques (1993) [40,42,43]. He compared a focused system and an unfocused system, and then made the following conclusions:

- Unfocused channels use lenses with the least complex configuration. By simply distributing lights from the input fibers onto the image plane, we can avoid a complex imaging system and alignment concerns. However, the drawback of this technique is that lights exhibit prohibitively low link efficiencies and create more optical noises.

- Focused channels use lenses or mirrors to contain the optical energy and direct it solely to the destination. The design, alignment, and packaging issues associated with these systems are considerably more complex. However, greater link efficiencies make this approach much more competitive with other interconnects.

Thus, most proposed and demonstrated free space optical interconnection systems are based on focused channels. In addition, McCormick suggested that imaging systems must have the following characteristics [40]:

- *High resolution* to collect all lights from a small source and concentrate the signal energy onto a small output.

- *Isoplanaticism*, so that the size, shape, and energy content of the signal spots do not change significantly across the optical system. This results in an optical system with low aberrations.

- *Low loss,* since power loss will affect system speed and tolerances.

In order to achieve these characteristics, three types of lens combinations have been proposed for the possible optical system [44]. They are: macro-lenses approach; microlens array approach, and hybrid lens approach (that is combining micro- and macro-lenses) [40,42]. The features of these three approaches are listed below:

A. macro-lens approach

In the macro-lens approach, all lights from the input array are treated as a single object. This object is imaged by the macro-lens approach to the image plane, much as a scene is imaged onto the film in a camera. The macro-lens imaging technology is well understood, and although macro-lens approach is still a rapidly developing area, it is a well–established technology. To date, several complex macro-lens optical free space system experiments have been demonstrated [40-42,45]. These optical systems generally operate at infinite conjugates. However, the main challenge is that this approach will face the issues of high-aberration, low-resolution and the large size of the entire system.

B. microlens array approach

Another possible optical system is microlens array approach. The microlens array is placed before each input/output array at a distance equal to the focal length. Microlenses provide high resolution at the optical input/output by dedicating a separate optical system for individual or small groups of optical signals [42]. Currently, microlens arrays can integrate with fiber arrays to form a collimated beams array. However, there are still some technical challenges in using microlens array approach [46-49]:

- The regular spacing of the microlenses demands that the location of the windows on the input/output planes be similarly constrained.
- The packaging constraint on an all-microlens system is severe. Thus it needs to ensure all the lenses have very close focal lengths,
- It is not easy to ensure the optical quality of microlens. Poor quality microlenses would give large spot sizes and loss.
- Misalignment of the beams on the microlenses will cause stray light and crosstalk problems.
- Current technology is limited to an array size of approximately 16X16 data channels.

C. hybrid lenses combination

A hybrid lenses combination uses a microlens array to provide the focusing power in the system and one or more macrolens to control the diffraction of beams. The microlens operates at low f - number[1] (i.e., $f/1$ to $f/5$) and provide most of the lens *NA*[2]. The macrolens operates a high f - number (i.e., $f/10$ to $f/30$) and provides the geometric image magnification. Microlenses arrays have the advantage that they can break a large field into several smaller fields [40,42,50]. The advantages for using this combination are:

- The tolerance of the microlens is not critical.
- Larger arrays and higher input/output may be supported. This is because a hybrid lens controls the diffraction, which limits the array size of microlens system.
- It reduces magnification error on the image plane. Because macrolens operates at high f –number, thus this combination will increase the tolerance for mechanical misalignment and aberrations.
- Microlens can provide independent beam control in comparison to macrolens.

Tooley et al suggested that if the microlens is used at finite conjugates and the macrolens is used at infinite conjugates, then this approach has the desirable attribute of ensuring that large-diameter collimated beams sharing a common aperture stop propagate between compound lens with minimal angular spread.

For certain system assumptions, hybrid lenses have been shown to be the most efficient method (in terms of volume and channel cost) of implementing the optical channel [50].

---

[1] f -number or ($f/\#$) is the ratio of the focal length f to the clear aperture ϕ of a lens system ($f/\# = f/\phi$). Related to numerical aperture by $f/\# = 1/(2NA)$.

[2] NA, *Numerical aperture*, which is the index of refraction (of the medium in which the image lies) times the sine of the half angle of the cone of illumination.

1.4 The Aims and Organization of Present Thesis

Intelligent Reconfigurable Optical Switch (IROS) is an $N \times N$ all-optical free space LC-SLM switch. The application for IROS is to protection switching N input fiber ports into N output ports simultaneously, where $N > 1000$. The primary development of first model 36×36 OXC was taken in 2000. The optical switch has the reconfiguration time, which is the required time to change all interconnections through the switch, of less than 10 milliseconds; a bandwidth of 60 nm in 1550 nm window, and the noise isolation of greater than 20dB [9]. The whole system has physical dimensions of $500mm \times 250mm \times 100mm$. The block diagram of the switch is shown in Figure 1.5. We assume that the system will perform well in WDM systems, because the variation in the optical system due to small changes in wavelength is negligible. However, the wavelength sensitivity of the system in general will need future study.

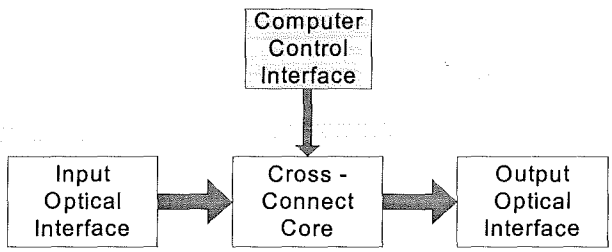

Figure 1.5: Block diagram of the optical switch

The basic concept of operation for this switch is that the input fibers are arranged in a 2D array (input optical interface). Then light beams are launched onto the cross-connect core, and subsequently illuminated onto the 1st SLM. SLM is a modulator device to dynamically modulate optical beams. SLM acts as phase-only diffraction grating with a reconfigurable pattern to set the deflection angle of the reflected beam. Each modulator on the SLM works independently. The reconfigurable pattern is generated by a computer connected through the computer control interface. By controlling the deflection angle, the beam is made to reflect back onto the 2nd SLM, where it is diffracted again and then coupled into the selected output port (output optical interface).

IROS utilizes two SLMs, which have the advantage of achieving compact system size, and it can easily extend the size of the switch ports without additional loss penalty. The two SLMs are placed in parallel, with the input and output fiber array pointing at each respective SLM.

In order to achieve the large-capacity OXC, which is compact, inexpensive, and reliable, low power loss, small loss variation, and low crosstalk are necessary. This is because if the insertion loss of the optical switch is large, optical amplifiers (OAs) will be required to compensate for the loss inside the node. If the loss variation at each switch port is large, the optical receiver (OR) at the termination or regenerating nodes cannot receive the optical signals, as the dynamic range of the OR may be exceeded. If the crosstalk of the optical switch is large, optical signals will be disturbed by other optical signals.

The main focus of this thesis is design and characterization of beams emitted from the input optical interface and their illumination profile on the 1st SLM. Typically, optical signal propagation in this free space can be treated as *image shifting*. Therefore, lenses can be used as an imaging tool to control the optical signals. However, some challenges in designing such optical system in a limited space are listed below:

Firstly, the beams by nature are divergent, but they need to be collimated, so that the crosstalk or signal overlap would be reduced. For example, the output of a 10 μm diameter light source at 1550 nm will diverge at a full angle of 11.3°. After propagating 1 cm, the beam will expand to almost 2 *mm* in diameter! Thus, significant crosstalk may result.

Secondly, each beam emitted from input optical interface should be magnified to an adequate size on the 1st SLM; so that the desired steering angle can be achieved by phase holographic pattern. The scaling amount is determined by "clipping ratio", which will be discussed in Section 3.1.2.

Finally, all beams should be simultaneously aligned to their corresponding positions on the 1st SLM with low aberrations (or to reduce aberration to its 'diffraction limit'[3]).

Taking the above considerations, the designed optical system should satisfy the characteristics of the beam illuminated on the 1st SLM. The design of the optical system is based on the hybrid combination approach, which is composed of microlenses and macrolenses. Thus, a microlens array will be designed and two macro-lenses are selected from the market catalogs. The results show that the proposed optical system achieves the required beam performance criteria of alignment, collimation, and magnification. Also, Modulation Transfer Function (MTF) is introduced to verify that the

[3] Due to the wave nature of light, any optical system with a finite size aperture can never form a perfect image. There is a characteristic minimum blur diameter, even when other image aberrations are absent. Therefore, the best performance that an optical system is capable of is called its "diffraction limited" performance.

optical system creates low aberration of image on the 1st SLM. The rest of this thesis is organized as follows:

In **Chapter 2**, we review the literature which is relevant to this research. At the beginning, the properties of Gaussian beam propagating in free space and passing through a single lens are discussed. Next, we study aberration. Typically, aberrations can be divided into two groups: wavefront error (or optical path difference, OPD), which appears on the system exit pupil, and transverse aberration (TA), which appears on the image plane. We present these two groups in polynomial forms so that we could find the defect type and its amount of aberration from the item and its coefficient of polynomial. Finally, we introduce some techniques to reduce system aberrations.

In **Chapter 3**, we present the process of optical system design. The "clipping ratio" of the beam size shining on SLM is determined. Thus, the optical parameters for each component in the optical system are calculated. Four possible layouts of lens combinations are designed and simulated by a software program. Finally, the beam qualities for these four layouts are analyzed and compared.

In **Chapter 4**, we analyze the aberrations, which are generated by these four layouts. Aberrations are described as three perspectives: System OPD (optical path difference), wavefront error at the exit pupil, and transverse aberration on the image plane. System OPD is expressed as a single-number and the unit is wavelength. Wavefront error and transverse aberration are illustrated by figure and polynomial. Therefore, the types and amount of aberrations occurred in each layout could be measured. Finally, we will select one layout to present our optical system.

In **Chapter 5**, we modify the selected layout, so that the beam quality is improved and the aberration effect is reduced. The result shows that the optimized lens system achieves the required beam performance criteria of alignment, collimation, magnification, and low aberration. In addition, the optimized lens system is found to be diffraction limited on the SLM, and this is analyzed by using the modulation transform function (MTF).

In **Chapter 6,** we conclude this thesis with a summary of the most important results and suggest future prospects and possible improvements.

Chapter 2

Literature Review

An efficient lens design should take into account the beam characteristics and attempt to reduce the aberrations, which exhibit in the image plane. This is because light emitted from a laser has the form of a Gaussian beam. Since a lens is utilized in this light source, the behavior of the beam can be significantly different from that which would be anticipated on the basis of geometrical optics. In this chapter, two main topics are reviewed. First, we present the characteristics of a Gaussian beam as it propagates in free space and traces through a lens system. Then, we explore the wave and ray aberrations expressed as polynomial forms, and discuss some techniques to reduce system aberrations.

2.1 Light Propagation and Collimation

2.1.1 Gaussian beam propagation in free space

Free space is a field that is homogenous, isotropic and source free. A Gaussian beam that propagates in free space is a paraxial wave, meaning that its wavefront normals are nearly unidirectional along the propagation axis (we define z axis). A paraxial wave is a plane wave e^{-jkz} modulated by a complex envelope $A(\vec{r})$, which makes it a slowly varying function of position. Thus, the complex amplitude can be expressed

$$U(\vec{r}) = A(\vec{r})\, e^{-jkz} \tag{2.1}$$

where k is wavenumber, and z is the wave propagation direction. In order to maintain its underlying plane wave nature, variation of $A(\vec{r})$ with position must be slow within the distance of a wavelength $\lambda = 2\pi/k$. In addition, the complex envelope $A(\vec{r})$ must satisfy the *paraxial Helmholtz equation*, so that the complex amplitude $U(\vec{r})$ can satisfy the *Helmholtz equation* $\nabla^2 U + k^2 U = 0$, which is derived from Maxwell's equations [52].

U represents the component electric E and magnetic B of the radiation field. The complex envelope $A(\vec{r})$ in paraxial Helmholtz equation is

$$\nabla_T^2 A - j2k\frac{\partial A}{\partial z} = 0 \tag{2.2}$$

where $\nabla_T^2 = \partial^2/\partial x^2 + \partial^2/\partial y^2$ is the transverse part of the Laplacian operator. The simplest solution for paraxial Helmholtz equation is the paraboloidal wave and it has the spherical wave as a paraxial approximation [53]. One solution for the complex envelope of Gaussian beam provides paraboloidal wave to Eq. (2.2) is

$$A(\vec{r}) = \frac{A_1}{q(z)}\exp(-jk\frac{\rho^2}{2q(z)}),\ q(z) = z + jz_R$$

where $\rho^2 = x^2 + y^2$, A_1 is a constant, and z_R is the Rayleigh range. Therefore, the complex amplitude $U(\vec{r})$ can be expressed as

$$U(\vec{r}) = \underbrace{A_0\frac{\omega_0}{\omega(z)}\exp[-\frac{\rho^2}{\omega^2(z)}]}_{amplitude\ factor}\ \underbrace{\exp[-jkz - jk\frac{\rho^2}{2R(z)} + j\zeta(z)]}_{phase\ factor} \tag{2.3}$$

where $\vec{r}$ is a three dimensions vector expressed as $\vec{r} = x\,\hat{i} + y\,\hat{j} + z\,\hat{k}$, A_0 is a constant, ω_0 is the waist radius, $\omega(z)$ is beam radius on *x* - *y* plane, $R(z)$ is the curvature radius of Gaussian beam, and $\zeta(z)$ is phase retardation which ranges from $-\pi/2$ at $z = -\infty$ to $+\pi/2$ at $z = \infty$. These parameters of Gaussian beam are related to the Rayleigh range and can be expressed as

$$\omega(z) = \omega_0\left[1 + (\frac{z}{z_R})^2\right]^{\frac{1}{2}} \tag{2.4}$$

$$R(z) = z\left[1 + (\frac{z_R}{z})^2\right] \tag{2.5}$$

$$\zeta(z) = \tan^{-1}\frac{z}{z_R} \tag{2.6}$$

At beam waist position, the wavefront is flat and the beam radius has a minimum value ω_0. Rayleigh range z_R can be derived from Eq. (2.5):

$$\frac{d\,R(z)}{d\,z}=0,\ \text{then}\ \frac{dR(z)}{dz}=1-\left(\frac{\pi\,\omega_0{}^2}{\lambda}\right)^2\frac{1}{z_R^2}=0$$

$$z_R=\frac{\pi\omega_0^2}{\lambda} \tag{2.7}$$

Beam radius $\omega(z)$ is defined as the radial distance $\rho=\omega(z)$ where the beam intensity drops by the factor of $1/e^2\approx 0.135$ from its peak value. 86.5% of the power is carried within a circle of radius $\omega(z)$. Beam radius is also equal to the distance (in transverse direction) at which the field amplitude decays to $1/e$ of its maximum value. The waist diameter $2\omega_0$ is called the **spot size**. Far from the beam center, the beam radius increases approximately linearly with z, defining a cone with half-angle θ_0. The angular divergence of the beam is defined by the angle

$$\theta_0=\frac{\lambda}{\pi\omega_0} \tag{2.8}$$

Eq. (2.8) shows that the smaller beam waist ω_0, the larger the divergent angle θ_0. In addition, in order to produce a highly 'collimated' Gaussian beam, the waist diameter must be much larger than the wavelength. Figure 2.1 shows a Gaussian beam which emits from a fiber core into a free-space (z-axis direction). This figure shows that the beam waist is at the end of the fiber core. The Rayleigh range z_R, beam radius $\omega(z)$, and divergence θ_0 are presented in this figure. Using Eq. (2.8) we can say that a beam will rapidly diverge (20^0) from a single-mode fiber if the radius of the fiber core is 5 μm and light source wavelength λ is 1550 nm. For this small aperture of beam emission, D. Marcuse proposed the beam waist coincides with the end of core fiber radius a and fiber V - number in a step-index single-mode fiber [54]:

$$\frac{\omega}{a}=0.65+\frac{1.619}{V^{1.5}}+\frac{2.879}{V^6} \tag{2.9}$$

where $V = \frac{2\pi a}{\lambda} NA$, and NA is the fiber numerical aperture. His research shows that for a step-index single-mode fiber whose V - number is 2.4, its field distribution of the fiber mode almost perfectly matches the Gaussian field and the error of Gaussian spot size is 1%. Eq. (2.9) is commonly used for the Gaussian spot size in step-index single-mode fibers [55].

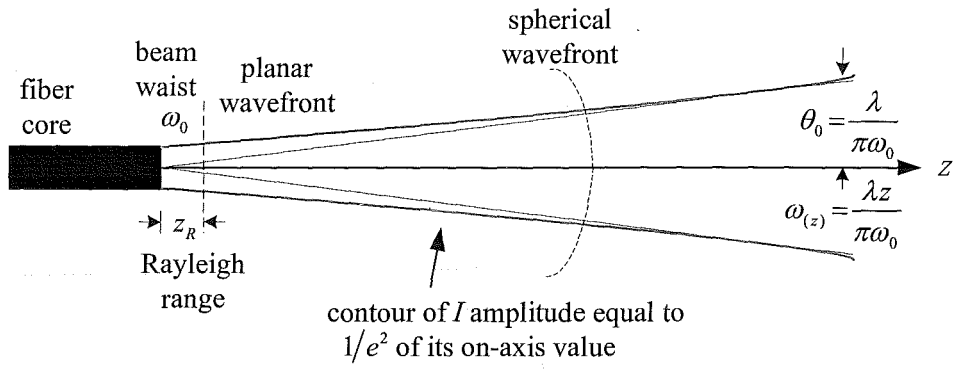

Figure 2.1: A Gaussian beam propagates from a fiber core to a free space (z-axis direction).

The phase of a Gaussian beam in the Eq. (2.3) can be expressed as

$$\varphi(\rho, z) = kz + \frac{k\rho^2}{2R(z)} - \zeta(z) \tag{2.10}$$

The first term is the same as the phase of a *propagating plane wave*. The second term is responsible for *wavefront bending*, or *phase front curvature*. It represents the deviation of the phase at off-axis point in a given transverse plane from that at the axial point. The radius of curvature subsequently increases with further increase of z until $R(z) \approx z$ for $z \gg z_R$. The wavefront is then approximately the same as that of a spherical wave. The last term is *phase retardation*, which corresponds to an excess delay of the wavefront in comparison with a plane wave or a spherical wave. The total accumulated excess retardation as the wave travels from $z = -\infty$ to $z = \infty$ is π. Typically, except for an excess phase $\zeta(z) \approx \pi/2$, the complex amplitude of the Gaussian beam approaches that of the paraboloidal wave, which in turn approaches that of the spherical wave in the paraxial approximation [52].

2.1.2 Light collimation with a lens

If a Gaussian beam emits through a set of circularly symmetric thin lenses along the beam axis, then the amplitude distribution remains Gaussian, as long as the overall system maintains a paraxial wave [56,57]. In addition, only the beam waist and curvature are altered, so that the beam is reshaped [58]. The general characteristic of a Gaussian beam propagation through lenses used in geometrical optics is reported by S. A. Self [59]. He models the transformations of a Gaussian beam through a simple positive optical lens as shown in Figure 2.2.

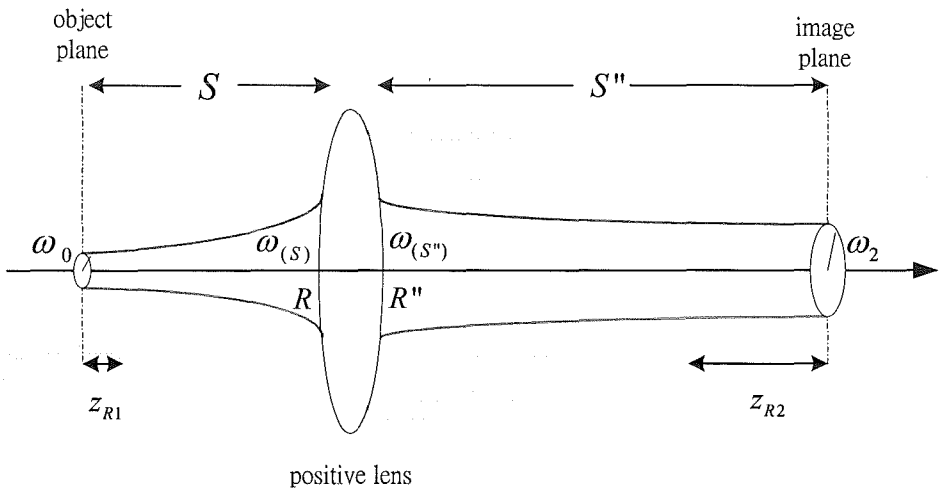

Figure 2.2: A Gaussian beam refract through a thin lens

Under paraxial condition, if the input beam waist radius ω_0 and the object distance S are specified, then the Rayleigh range z_{R1}, the beam's radius $\omega_{(S)}$, and radius of curvature R at the lens can be calculated from Eqs. (2.4), (2.5),and (2.7) respectively.

For a thin lens, the beam radius is unchanged through the lens $\omega_{(S)} = \omega_{(S")}$, while the radius of the curvature is changed by an amount of $(1/f)$ as in the geometrical optics case:

$$\frac{1}{R}+\frac{1}{R"}=\frac{1}{f} \tag{2.11}$$

where R is positive since the wavefront of the incident beam is diverging and $R"$ is negative since the wavefront of the transmitted beam is converging. From Eqs. (2.11), (2.4) and (2.5), we find

$$\frac{1}{S\left[1+\left(\frac{\pi\omega_0^2}{\lambda S}\right)^2\right]}+\frac{1}{S''\left[1+\left(\frac{\pi\omega_2^2}{\lambda S''}\right)^2\right]}=\frac{1}{f} \tag{2.12}$$

From Eq. (2.12), we also can conclude that the *beam waist location* S'' and *beam waist magnification* M are:

$$\frac{S''}{f}=1+\frac{\frac{S}{f}-1}{\left(\frac{S}{f}-1\right)^2+\left(\frac{\pi\omega_0^2}{\lambda f}\right)^2} \tag{2.13}$$

$$M=\left(\frac{\omega_2}{\omega_0}\right)=\sqrt{\frac{1}{\left(\frac{S}{f}-1\right)^2+\left(\frac{\pi\omega_0^2}{\lambda f}\right)^2}} \tag{2.14}$$

If the Rayleigh range z_R replaces $\frac{\pi\omega_0^2}{\lambda}$, then Eqs. (2.13) and (2.14) can be given as

$$\frac{1}{(S/f)+\frac{(z_R/f)^2}{(S/f-1)}}+\frac{1}{(S''/f)}=1 \tag{2.15}$$

$$M=\left(\frac{\omega_2}{\omega_0}\right)=\sqrt{\frac{1}{\left(\frac{S}{f}-1\right)^2+\left(\frac{z_R}{f}\right)^2}} \tag{2.16}$$

From Eq. (2.15), a plot of (S/f) versus (S''/f) for various values of (z_R/f) is shown in Figure 2.3 [53,59]. This figure shows that for nonzero values of (z_R/f), all the curves have a single continuous branch passing through the same point (S/f) = (S''/f) = 1. This means that when an object is placed at a focal length, the image will show at the other side of focal length, not at infinity as in geometric optics description. In addition, this is independent of the ratio (z_R/f). Alternatively, for a Gaussian beam waist, since the incident light is at the front focal length (f_{FFL})[4] of a positive thin lens, then the emerging beam has a waist at the back focal length (f_{BFL})[5].

---

[4] f_{FFL} is front focal length, which is the distance from the object plane of a lens to its first surface.

[5] f_{BFL} is back focal length, which is the distance between the last surface of a lens to its image focal plane.

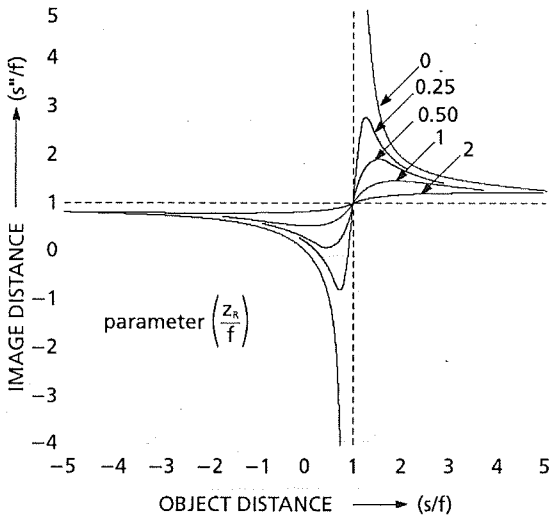

Figure 2.3: Plot of the lens formula for Gaussian beams [53,59].

Eq. (2.15) and Figure 2.3 indicate that (S''/f) has a maximum value of $1+1/2(z_R/f)$ when (S/f) = $1+(z_R/f)$. Therefore, the image distance has a maximum value of $S'' = f + f^2/2z_R$, and this occurs when $S = f + z_R$; while (S''/f) has a minimum value $1-1/2(z_R/f)$ when (S/f) = $1-(z_R/f)$. In this case, the image distance will have a minimum distance $S'' = f + f^2/2z_R$ and this occurs when $S = f - z_R$. This relationship is different from the geometric optics description. The minimum distance from a real object to a real image is $4f$, when $S = S'' = 2f$.

Eq. (2.16) shows that the magnification of a beam by using a positive thin lens. The maximum magnification is (f/z_R), when object beam waist is at focal length $S = f$. And the Rayleigh range of the output beam is given by

$$z_{R2} = M^2 \, z_{R1} \tag{2.17}$$

2.2 Aberration Analysis

Aberration is an image error, which is generated by an optical system. Light can be described by two characteristics: ray and wave [60,61]. In an ideal optical system or an aberration free system, all rays from a point source at the object plane converge to the same point in the image plane to form a clear image. In the wave of light aspect, a perfect real image formed by the wavefront associated with each of the rays leaving the optical system must be spherical and centered on the image point. This is because Fermat's principle states that the optical path length of each ray will be identical. The ideal image forming is only available at the paraxial region of the optical axis and the optical system has an infinite aperture. However in practice, since lenses have finite apertures and fields of view, aberrations are generated due to various types of image faults. In other words, aberrations are the light deviations from the ideal [62]. There are two basic ways to characterize aberrations:

1. By the distance that a ray misses the paraxial focus point.

2. In terms of the departure of the wavefront from a spherical surface, called the reference sphere.

These two descriptions are equivalent as shown in Figure 2.4. The first description is of *transverse aberration* (TA), which is the distance by which the rays miss the paraxial focus; or the *angular aberration* (α), which is the angle by which the rays deviate from the perfect ray, which will hit paraxial focus. The second description is of wavefront aberration (W) or wavefront error, which is the deviation of the wavefront from a reference sphere, as a function of location in the exit pupil [60-62].

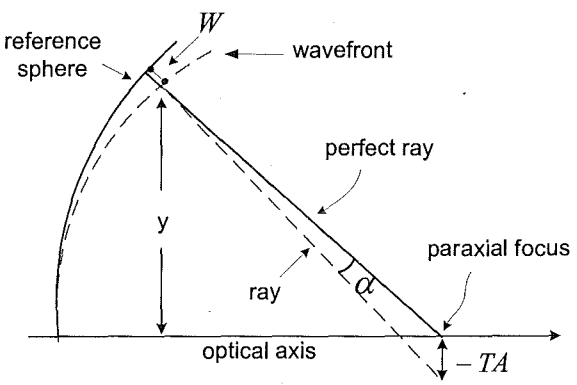

Figure 2.4: Ray and wave aberrations

In this thesis, we only focus on monochromatic aberrations, because our light source is monochromatic. Typically, monochromatic aberrations fall into two sub-groups. The first group includes *spherical aberration*, *coma*, and *astigmatism* that degenerate the image, or make the image unclear. The second group includes *field curvature* and *distortion* that deform the image. These five primary image defects are referred to as the *Seidel aberrations*, attributed to L. von Seidel who investigated and codified the primary aberrations and derived analytical expressions for their determination during the 1850's [62]. These five primary aberrations are described in Appendix A.

In practice, a combination of the above aberrations is found in a single optical element. The above five aberrations give a good description of optical system image quality. Figure 2.5 shows images of a point object under spherical aberration, coma, and astigmatism. Those images are formed at the positions of inside, outside, and on the focal plane [60].

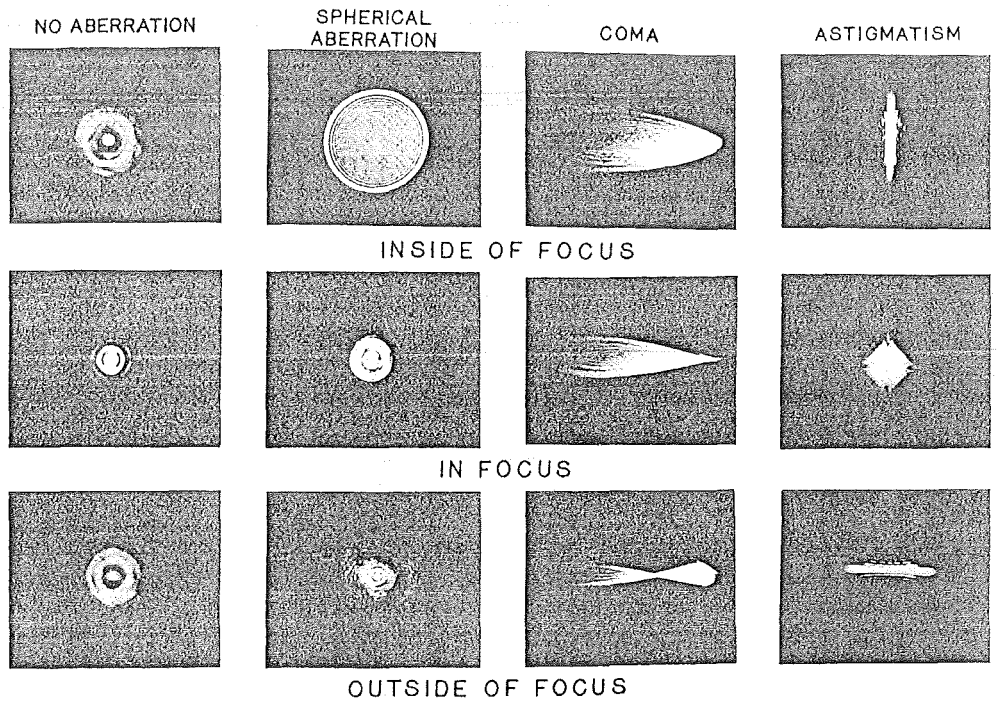

Figure 2.5: images of a point object under no aberration, spherical aberration, coma, and astigmatism at the positions of inside, outside, and on the focal plane [60].

2.2.1 Wavefront aberration

One technique for characterizing aberrations was introduced by W. R. Hamilton (1805-1865). This technique expresses aberration of an optical system in terms of the departure of actual wavefront from an ideal spherical shape (called reference sphere). From paraxial theory, we know that an optical system will image an object point source into the point image. Therefore, in free space, all rays from the point source will arrive to the image point. The geometrical wavefront is formed by generating the normal to each of rays and is a sphere for a point image. This spherical surface is called reference sphere. The difference in the optical paths of rays traveling through an optical system, i.e. the *Optical Path Difference* (*OPD*), is equivalent to the deviation of the wavefront from the reference sphere as shown in Figure 2.6. The OPDs are usually quoted in wavelengths. The OPD is often calculated as a single number that characterizes the aberration. Figure 2.7 shows the isometric plots for some of wavefront aberrations [63].

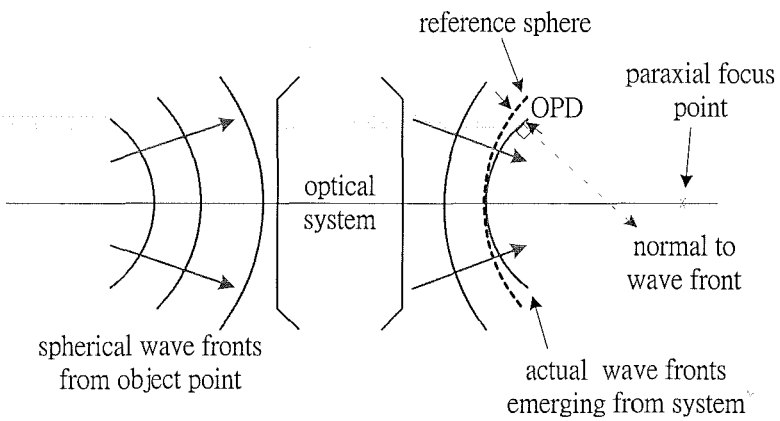

Figure 2.6: Wavefront aberration and optical path difference

The deviation of the actual wavefront $A(x,y,z)$ from the reference sphere $R(x,y,z)$ and in the exit pupil[6], gives us the wavefront aberration $W(x,y,z)$, measured along the radius of the reference sphere [60]:

$$W(x,y,z) = A(x,y,z) - R(x,y,z)$$

[6] Exit pupil is the image of the aperture stop as seen from an axial point on the image plane through the interposed lenses.

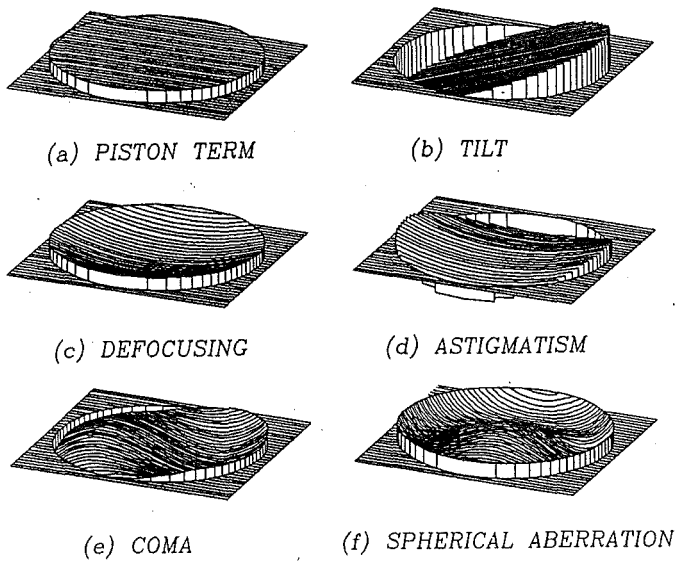

Figure 2.7: Some types of wavefront aberrations [60].

We express the wavefront shape in terms of a polynomial including high order aberration terms:

$$W(x,y)=\sum_{i=0}^{k}\sum_{j=0}^{i}c_{ij}\,x^{j}\,y^{i-j} \tag{2.18}$$

where k is the degree of the polynomial, and c_{ij} is the coefficient for each term. If we consider the polar coordinates, x and y can be expressed as $S\sin\theta$ and $S\cos\theta$ respectively, then Eq. (2.18) can express as

$$W(S,\theta)=\sum_{n=0}^{k}\sum_{l=0}^{n}S^{n}(a_{nl}\cos^{l}\theta+b_{nl}\sin^{l}\theta) \tag{2.19}$$

where θ is measured with respect to y-axis, a_{nl} and b_{nl} are the coefficients for the $\cos\theta$ and $\sin\theta$ terms respectively, and S is the aperture of an optical system. The term $\cos\theta$ and $\sin\theta$ describe the symmetrical and anti-symmetrical components of the wavefront respectively. Due to the symmetry of the optical system, not all possible values of n and l are permitted. To have a single valued function, Eq. (2.19) must satisfy the condition:

$$W(S,\theta)=W(-S,\theta+\pi)$$

Then, n and l must be both odd or both even. We only consider a wavefront produced by an axially symmetric optical system, with a point object displaced along the y axis. The wavefront is symmetric about the tangential plane, and we obtain

$$W(S,\theta)=\sum_{n=0}^{k}\sum_{l=0}^{n} a_{nl}\, S^{n}\cos^{l}\theta \tag{2.20}$$

If we include the image height h within the Eq, (2.20) and consider the following two conditions [60]

1. The symmetry about the tangential plane: $W(S,\theta,h)=W(S,-\theta,h)$

2. The rotational symmetry of the lens system about the optical axis: $W(S,\theta,h)=W(S,\theta+\pi,-h)$

then the wavefront expression may be shown to be a linear combination of the terms of S^2, $h\,S\cos\theta$ and h^2 as shown below:

$$\begin{aligned}
&W(S,h,\theta)=w(S^2,h^2,Sh\cos\theta)=\sum_{k=0}^{m}\sum_{n=0}^{k}\sum_{l=0}^{n} w_{knl}S^{n}h^{k}\cos^{l}\theta \\
&=w_{000} \\
&+w_{200}h^2+w_{020}S^2+w_{111}Sh\cos\theta \\
&+w_{311}Sh^3\cos\theta+w_{220}S^2h^2+w_{222}S^2h^2\cos^2\theta+w_{131}S^3h\cos\theta+w_{040}S^4 \\
&+w_{240}S^4h^2+w_{151}S^5h\cos\theta+w_{060}S^6 \\
&+\text{.....}
\end{aligned} \tag{2.21}$$

where the coefficient w_{knl} is the power of each variables S^2, $h\,S\cos\theta$ and h^2; n is the power of the aperture S, k is the power of the image height h, and l is the power of $\cos\theta$, with $l\le n$. The sum of the powers of S and h is always an even number ($n+k=$ even number). The constant term w_{000} is zero, because the reference sphere and wavefront meet at the optical axis. The 2nd to 4th terms are associated with a shift in the location and a small change in the magnification of the image. These terms do not affect image quality and thus are not really aberrations. The 5th to 9th terms correspond to the lowest-order aberrations. Higher order terms correspond to the higher-order aberrations. The descriptions of the terms in Eq. (2.21) are listed in the Table 3.1.

Table 2.1: The descriptions of the wavefront aberration coefficients [60].

Constant term ($n+k=0$)	w_{000}	Piston term (constant OPD)
First order terms ($n+k=2$)	$w_{200}h^2$	Parabolic field phase term
	$w_{111}Sh\cos\theta$	Tilt about x axis (image displacement along the y axis) with magnification change
	$w_{020}S^2$	Defocusing
Third order or primary aberrations ($n+k=4$)	$w_{311}Sh^3\cos\theta$	Distortion
	$w_{220}S^2h^2$	Petzval curvature
	$w_{222}S^2h^2\cos^2\theta$	Primary astigmastism
	$w_{131}S^3h\cos\theta$	Primary (circular) coma
	$w_{040}S^4$	Primary spherical aberration
Fifth order aberrations ($n+k=6$)	$w_{240}S^4h^2$	Secondary field phase term
	$w_{151}S^5h\cos\theta$	Linear fifth order coma
	$w_{060}S^6$	Fifth order spherical aberration

We are particularly interested in the case of a centered optical system having only primary aberrations. The image height dependence is not considered, and the field phase terms can be neglected. Under these conditions, the wavefront aberration polynomial given by Eq. (2.20) may be written in a compact form:

$$W(S,\theta)=AS^4+BS^3\cos\theta+CS^2(1+2\cos^2\theta)+DS^2+ES\cos\theta+F$$

In Cartesian coordinat, we re-write above polynomial as

$$W(x,y)=A(x^2+y^2)^2+By(x^2+y^2)+C(x^2+3y^2)+D(x^2+y^2)+Ey+F \tag{2.22}$$

where A, B, C, D, E and F are related to the Eq. (2.21) and they are listed in the Table 2.2

Table 2.2: Aberration coefficients [60].

A = w_{040}	Spherical aberration coefficient
B = $w_{131}h$	Coma coefficient
C = $0.5\,w_{222}h^2$	Astigmatism coefficient
D = $w_{020}-0.5\,w_{222}h^2$	Defocusing coefficient
E = $w_{111}+w_{311}$	Tilt about the x axis (image displacement along the y axis)
F = w_{100}	Constant or piston term

2.2.2 Relationship between wave & ray aberrations

At the beginning of Section 2.2 we described that aberration can be expressed by two equivalent forms, ray aberration and wavefront error. In this section, we demonstrate the relationship between these two aberrations and deduce the transverse aberrations on the image plane by Eq. (2.22). Figure 2.8 illustrates the relationship between ray aberration and wavefront error. The deformed wavefront is shown as a solid line and the ray (normal to the wavefront) from zone Y intersects the axis at the point M. The reference sphere, centered at P, is shown dashed, $W(x,y)$ is the radial distance between the two surfaces, and r_W is the radius of curvature of the reference sphere. The ray is normal to the wavefront and the radius is normal to the reference sphere. TA is the transverse aberration, which is the value of the aberration in a perpendicular direction to the optical axis.

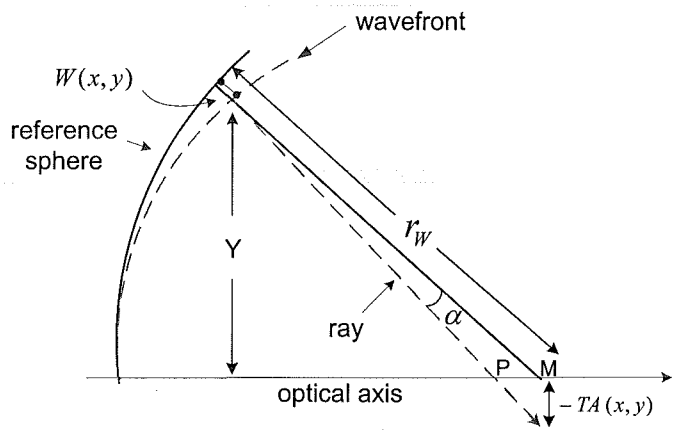

Figure 2.8: Relation between ray and wave aberrations

The angle α is the angular aberration, which is related to the spherical aberration by [61]

$$\alpha \simeq \frac{TA(x,y)}{r_W - W(x,y)} \tag{2.23}$$

The angle α between the two surface normal lines is also the angle between the surfaces, and, as shown in Figure 2.9, the change in wavefront corresponding to a small change in height dY, which is given by the relation

$$\alpha \simeq -\frac{d\,W(x,y)}{dY} \tag{2.24}$$

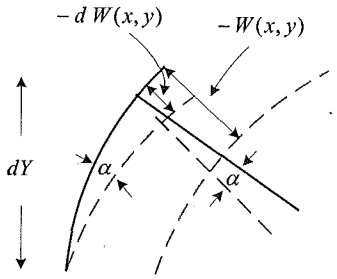

Figure 2.9: The relation between the angle α with the small change in wavefront corresponding to a small change in height $d\,Y$ [63].

An aberrated waverfront $W(x,y)$ has deformations with respect to the reference sphere, which are related to the transverse aberrations $TA_x(x,y)$ and $TA_y(x,y)$ by Eq. (2.23) and (2.24),

$$\frac{\partial W(x,y)}{\partial x} = -\frac{TA_x(x,y)}{r_W - W(x,y)} \tag{2.25}$$

$$\frac{\partial W(x,y)}{\partial y} = -\frac{TA_y(x,y)}{r_W - W(x,y)} \tag{2.26}$$

Typically, the radius of curvature of the reference sphere r_W is much larger than the wave aberration $W(x,y)$. If the wavefront deformations are known, the transverse aberrations may be calculated by

$$TA_x(x,y) = -\frac{\partial W(x,y)}{\partial x} r_W \tag{2.27}$$

$$TA_y(x,y) = -\frac{\partial W(x,y)}{\partial y} r_W \tag{2.28}$$

Eqs. (2.27) and (2.28) indicate that a positive transverse ray aberration is equivalent to a negative wavefront aberration and vice versa. It is easier to obtain and analyze the transverse aberrations for lens design if we know the wavefront aberrations. Eq. (2.27) and (2.28) express the relation between wavefront aberrations and transverse aberrations. Normally, to analyze an optical system design, a fan of 'tangential rays' and a fan of 'sagittal rays' are traced through the system, as shown in Figure 2.10. We assume that the tangential rays are on the y-axis and sagittal rays are on the x-axis. Thus,

we may calculate the transverse aberrations along x and y axes by using Eqs. (2.27), (2.28) and (2.22).

$$TA_x(x,y) = -[2(D+C)x + 2Bxy + 4A(x^2+y^2)x]\, r_W \tag{2.29}$$

$$TA_y(x,y) = -[E + 2(D+3C)y + B(3y^2+x^2) + 4A(x^2+y^2)y]\, r_W \tag{2.30}$$

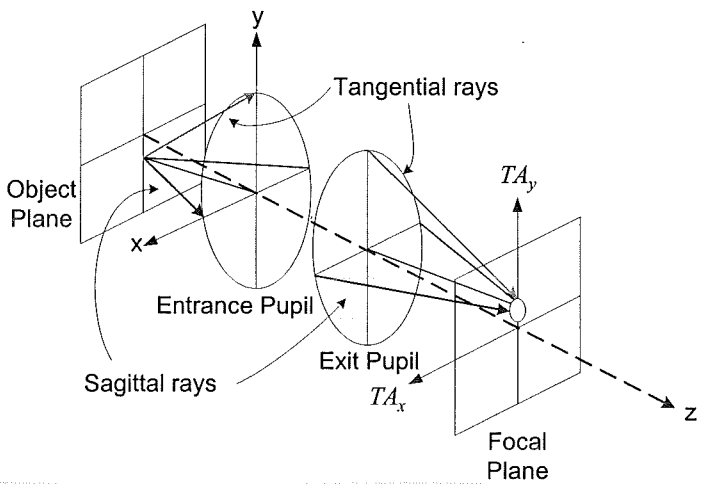

Figure 2.10: Tangential and sagittal fans of rays traced through an optical system

From Table 2.2 and Eqs. (2.27) and (2.28), the coefficients of the Eqs. (2.29) and (2.30) can be found as follows:

$$A = -\frac{SphT}{4r_W y^3} \tag{2.31}$$

$$B = -\frac{Coma_S}{r_W x^2} = -\frac{Coma_T}{3r_W y^2} \tag{2.32}$$

$$C = -\frac{\Delta f_S}{2r_W^2} = -\frac{\Delta f_T}{6r_W^2} \tag{2.33}$$

$$D = -\frac{\Delta f_A}{2r_W^2} \tag{2.34}$$

$$E = -\frac{\Delta h}{r_W} \tag{2.35}$$

where r_W is the radius of curvature of the reference sphere, $SphT$ is the transverse spherical aberration, $Coma_S$ is the sagittal coma, $Coma_T$ is the tangential coma, Δf_S is sagittal focus displacement, Δf_T is tangential focus displacement, Δf_A is axial focus displacement, and Δh is the transverse image displacement along the y-axis.

For Tangential plots:

We can obtain a tangential plot when the object is off-axis and the rays are on the tangential plane. Because the coordinate x on the entrance pupil is zero, $TA_x(x,y)=0$. $TA_y(0,y)$ is given by

$$\begin{aligned} TA_y(0,y) &= a_0 + a_1 y + a_2 y^2 + a_3 y^3 \\ &= -[E + 2(D+3C)y + 3By^2 + 4Ay^3]r_W \\ &= \Delta h + (\Delta f_A + \Delta f_T)\frac{y}{r_W} + Coma_T + SphT \end{aligned} \tag{2.36}$$

On the tangential plot, the tangential coma $Coma_T$ produces a parabolic term; the primary transverse spherical aberration $SphT$ produces a cubic term. The height of graph at the point crosses the y-axis is equal to the image displacement Δh. This image height is the distortion. Figure 2.11 shows tangential plots for some aberrations.

For Sagittal plots:

These plots are obtained when the y coordinate on the entrance pupil is equal to zero. Thus, the expressions will be:

$$\begin{aligned} TA_x(x,0) &= -[2(D+C)x + 4Ax^3]r_W \\ &= (\Delta f_A + \Delta f_S)\frac{x}{r_W} + SphT \end{aligned} \tag{2.37}$$

$$\begin{aligned} TA_y(x,0) &= -[E + Bx^2]r_W \\ &= \Delta h + Coma_S \end{aligned} \tag{2.38}$$

Eq.(2.37) measures antisymmetric transverse aberrations, such as spherical aberration and defocusing. Eq. (2.38) shows symmetric transverse aberrations such as $Coma_S$.

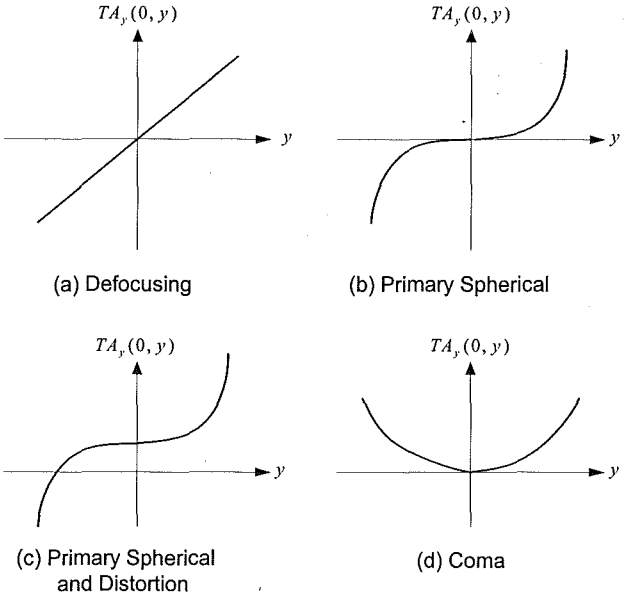

Figure 2. 11: Tangential plots with some aberrations

2.2.3 Aberration variation and reduction

From the previous sections, aberrations can be controlled by many factors, i.e., lens shape, aperture size and image height etc. Therefore, aberrations can be minimized by adjusting the above factors. In this section, those factors are studied in more detail.

A. Aberration and the effect of lens shape

A basic tool to change the aberration of a lens is to change its shape. For a thick lens, the focal length can be calculated by:

$$\frac{1}{f} = (n-1)\left(\frac{1}{R_1} - \frac{1}{R_2} + \frac{n-1}{n}\frac{t}{R_1 R_2}\right) \tag{2.39}$$

where n is the material index of the lens, t is the thickness of the lens, and R_1 and R_2 are the radii of the lens's front (first) and back (second) surfaces respectively. Alternatively, for a thin lens, the focal length is (when $t \ll R_1 \times R_2$):

$$\frac{1}{f} = (n-1)\left(\frac{1}{R_1} - \frac{1}{R_2}\right) \tag{2.40}$$

These two equations reveal that for a given index n and/or thickness t, there is an infinite number of combinations of R_1 and R_2, which will produce a given focal length. Thus a lens of some desired power (or, focal length) might take on any number of different shapes or "bendings". The degree of bending can be characterized by the Coddington shape factor q [53,63]:

$$q = \frac{R_2 + R_1}{R_2 - R_1} \tag{2.41}$$

Figure 2.12 shows the transverse and longitudinal spherical aberration of a singlet lens as a function of the shape factor q. This figure presents that a symmetric biconvex lens has the best shape, for not only spherical aberration is minimized, but also coma and distortion cancel each other out. Plano-convex lens shape ($q = 1$) with convex side toward the infinite conjugate performs nearly as well as a best-form lens. A best-form lens is described as a singlet shape with minimized spherical aberration at a given conjugate ratio. The criterion for *best form* at any conjugate ratio is that the marginal rays are equally refracted at each of the lens/air interfaces, thus minimizing the effect of the error ($\sin\theta \neq \theta$). It also meets the criterion for minimum surface-reflectance loss. Because a plano-convex lens costs much less to manufacture than an asymmetric biconvex singlet, these lenses are quite popular. Furthermore, this lens shape exhibits near minimum total transverse aberration and near zero coma when used off axis, thus enhancing its utilization. It is important to note that the *best form* shape is dependent on the refractive index. The higher the index n, the smaller the aberration for the optimum shape. We list the characteristics of primary aberrations and the corresponding corrections in Table 2.3.

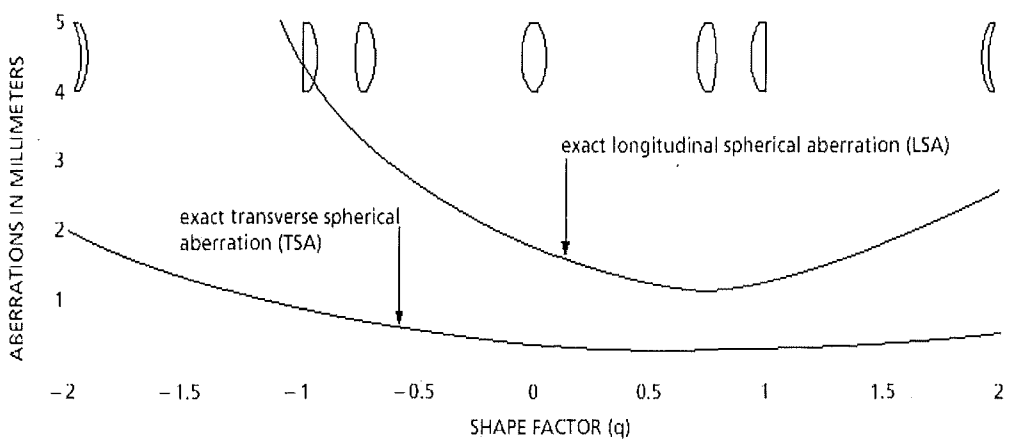

Figure 2.12: Spherical aberration of positive lens at infinite conjugate ratio as a function of lens shape [53].

Table 2.3: Summary of Aberrations and corrections [53,63].

Aberration	Characteristics	Correction
Spherical aberration	On- and off- axis, image blur	Bending, high index, doublet
Coma	Off- axis only, blur	Bending, spaced doublet with central stop
Astigmatism	Off- axis, blur	Spaced doublet with stop
Field curvature	Off- axis	Spaced doublet
Distortion	Off- axis	Spaced doublet with stop

B. Aberration and the effect of aperture and image height

From Table 2.1 (Section 2.2.1), we find that the variation of five primary aberrations can be described by the orders of aperture (S) and image height (h). Their relations are expressed in Table 2.4. This table can be utilized to minimize specific type of aberration, assuming that we have an optical system whose aberration parameters are known. For example, we wish to determine the change in aberrations, if the aperture diameter (S) is increased by 50 %, image height (h) is reduced by 50 %, and Coma varies as a function of S^2 and h. Based on these parameters, we can determine that the coma will be $(1.5)^2 \times 0.5$ or 1.125 times larger than its original size.

Table 2.4: The variations of Aberration with aperture and image height [53,63].

Aberration	Aperture (S)	Image height (h)
Transverse Aberration	S^3	–
Coma	S^2	h
Astigmatism	S	h^2
Field curvature	S	h^2
Distortion	–	h^3

2.3 Summary

In this chapter, we examined the Gaussian beam propagating in free space and considered its collimation, as well as exploring the optical aberrations.

First, we presented the paraxial wave equation and a solution with a Gaussian function, and then explored the characteristics of Gaussian beam propagation in free space. Eq. (2.9) allows us to precisely calculate for a beam spot size from a single-mode fiber into free space. After that, the beam size, wavefront curvature, Rayleigh range, and beam divergence in free space can be calculated by Eqs. (2.4), (2.5), (2.7) and (2.8) respectively. We can assume that Gaussian beam has an approximate spherical wavefront in the paraxial propagation axis. In order to collimate divergent beam, utilizing a lens is an ideal method. Eqs. (2.15) and (2.16) show that the image distance and beam magnification are functions of the object distance, focal length of the lens and Rayleigh range. Moreover, the determination of a focal length f of a lens is related to the Rayleigh range z_R. This is because the parameter (z_R/f) affects the value of deviation range of image distance as shown in Figure 2.3.

Next, we reviewed the aberrations, which are expressed by polynomial form for wavefront error at the exit pupil (i.e., Eq. (2.21)) or by transverse aberration at the image plane (i.e., Eqs. (2.36) and (2.37)). The coefficients for these polynomials represent the specific types of aberrations. Eqs. (2.27) and (2.28) show the relationship between wavefront and transverse aberrations.

Finally, we described some techniques to reduce aberrations for the design of our optical system. Figure 2.12, Table 2.3 and Table 2.4 describe each aberration reduction technique by selecting the lens shape, and adjusting the lens aperture or image height.

Chapter 3

Design of the Optical System

3.1 System Layout and Analysis

3.1.1 System specifications and requirements

Intelligent Reconfigurable Optical Switch (IROS) is an all-optical free space switch. It is designed to switch 36 input fiber ports into 36 output ports simultaneously. The basic concept of operation is that the input fibers are arranged in a 6×6 array from which the light beams are emitted and subsequently collimated, through an optical system onto the spatial light modulators (SLM). SLM is a modulator device, which is able to dynamically modulate optical beams. SLM acts as phase-only diffraction grating with a reconfigurable pattern, setting the deflection angle of the reflected beam. By controlling the deflection angle, the beam is made to reflect back into a second SLM, where it is diffracted again onto the selected output port, where the beam is coupled into the output fiber. The advantage of using two SLMs is to increase the coupling efficiency into the output fibers and the ability to extend the size of the switch without an additional loss penalty. This operation concept of IROS is shown in Figure 3.1. It shows that one beam is emitted from an input fiber, through three optical systems and two SLMs, and finally is coupled into a specific output port [51].

The processes involved in the operation of IROS are considered in three physical subsections of the system. Firstly, light emits from the input fiber array to the 1st SLM; then, is modulated by the 1st SLM and steered to the 2nd SLM where it is modulated for a second time; and finally, light propagates from the 2nd SLM and coupled to the output fiber array. The design of the first optical system has the same architecture as the third stage. This is because of the symmetrical nature of the system with respect to the inputs and outputs.

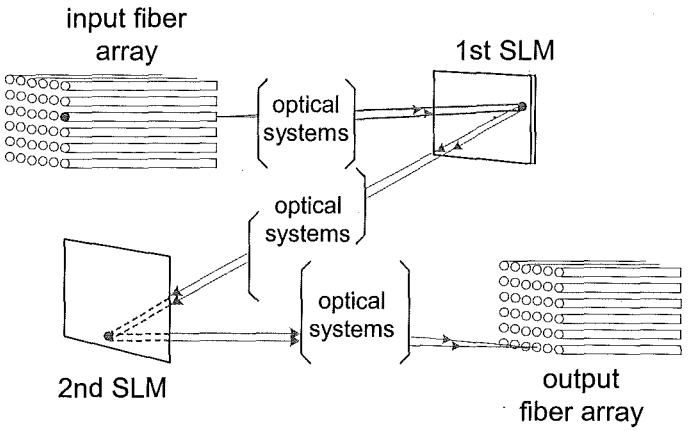

Figure 3.1: The configuration of IROS

In this thesis, we focus on the first subsection of the system, i.e. the processes involved in the transmission of light from the input to the first SLM. Typically, a lens or a group of lenses can be utilized to implement the optical design of this segment. However, practical lens design in an optical system cannot avoid aberration on the image plane. Aberration will cause signal deformation thereby increasing power loss and noise in the transmission process. Therefore, there are a number of strict requirements for the optical design of this switching system. These requirements are necessary to ensure that beams from the input fiber array are properly imaged upon the array of modulators [64]. Thus, a compact, inexpensive, reliable and low loss switch is realized.

- The first requirement is that the optical system must provide precise alignment mechanisms and low aberrations (or to achieve diffraction limited case) performances on the first SLM. This requirement of beam quality illuminating the SLM is essential, because each beam needs to be aligned and collimated to its corresponding modulator. So, the cross talk or signal overlap can be minimized in the transmission.

- The second requirement is that the images on the SLM must be diffraction limited. This is because phase - only hologram provides the steering function by spatially varying the phase of the incident beam. The pixilated nature of hologram leads to diffraction. This diffraction at the edges of the hologram aperture will produce noise.

- The third requirement is that the optical system must be compact and reliable. This is because the dimensions of the SLM are dictated by the available fabrication technology.

- Finally, all of these requirements must be achieved such that the resulting system is inexpensive and has a low power loss, as dictated by competing products.

Figure 3.2 shows the physical layout of the first stage of the whole system. The fiber spacing is the distance between the adjacent fiber cores. $d_{\min}$ is the minimum required distance between the last component of the optical system and the 1st SLM. The pixel block is a unit modulator to steer a Gaussian beam from the input fiber.

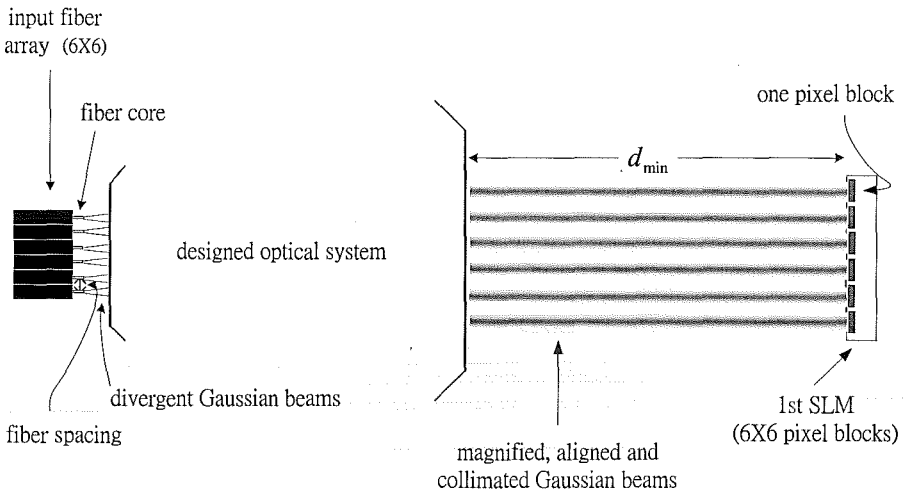

Figure 3.2: Propagation of light from input fiber array to the 1st SLM

The minimum required distance $d_{\min}$ could be computed with some assumptions. For the "Z" configuration, the 1st SLM is given a $7^0 \sim 10^0$ tilt angle with respect to the input fiber array. If the last optical element has an aperture of 25.4 *mm*, then the minimum distance is 147.4 *mm*. Figure 3.3 illustrates the minimum required distance $d_{\min}$ in the IROS system.

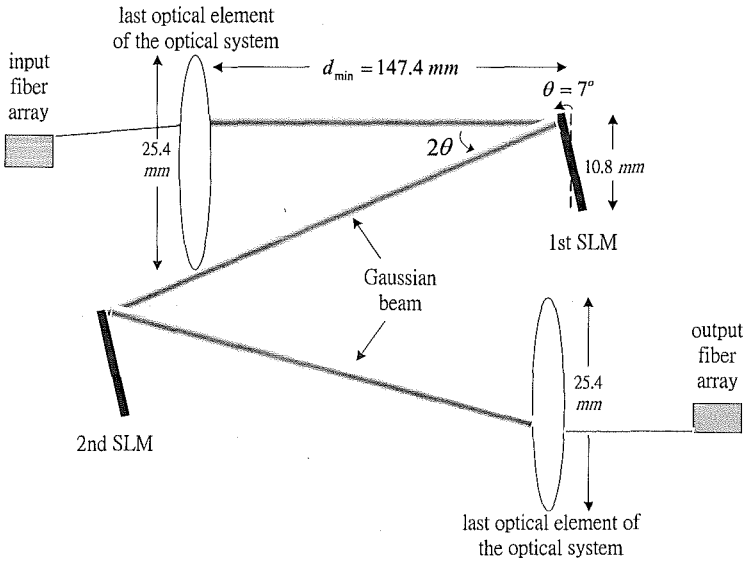

Figure 3.3: Illustration of the minimum distance $d_{\min}$.

The main reason for requiring the minimum distance is that we need to reserve a minimum space, so that beams traveling between the two SLMs will not hit the last optical component. However, for the sake of a compact design, we need to make certain this distance is available and as short as possible.

A 25.4 *mm* aperture size of the last optical element is selected; because we designed all beams to pass through an optical lens with a high f-number (in a paraxial condition). Therefore, the selection of a bulk lens can be achieved and thus aberrations can be reduced.

3.1.2 SLM and light clipping ratio

A phase-only hologram provides the steering function by spatially varying the phase of the incident beam. The hologram is recorded onto a liquid crystal over silicon SLM. The pixels of the SLM are divided into a number of pixel blocks, where each pixel block acts as an independent phase hologram and modulates one beam. The number of pixels on a pixel block and the space between the adjacent blocks will need particular attention to ensure accurate steering of the Gaussian beam, as well as reducing cross talk between channels [65].

The SLM consists of 6 X 6 pixel blocks with each pixel block containing 128 X 128 pixels. The pixel pitch is 10.8 μm. Therefore, one pixel block has an effective area of 1.382 *mm* x 1.382 *mm.* The space between the pixel blocks is 0.5 *mm.* The total dimension of SLM is 10.8 *mm* x 10.8 *mm.* The switching time requires 1 ~ 10 *ms.* In order to proceed with the detailed analysis of the system, we set the optical axis at the center of the SLM as (0, 0) illustrated in Figure 3.4. Due to the symmetrical nature of this structure, we only need to investigate the 6 pixel blocks out of the 36 (namely, port 1, 2, 3, 5, 6 and 9). The SLM and one pixel block dimensions are also shown in the figure.

Having presented the structure of the SLM; the next issue to be addressed is that an adequate area of the pixel block is illuminated by the incoming light. The light emitted by an optical fiber is approximately Gaussian. It is impossible to route the entire Gaussian beams through the hologram system, since a Gaussian beam extends to infinity we only have a finite pixel block. Therefore, we need to determine how much of the Gaussian beam can be clipped.

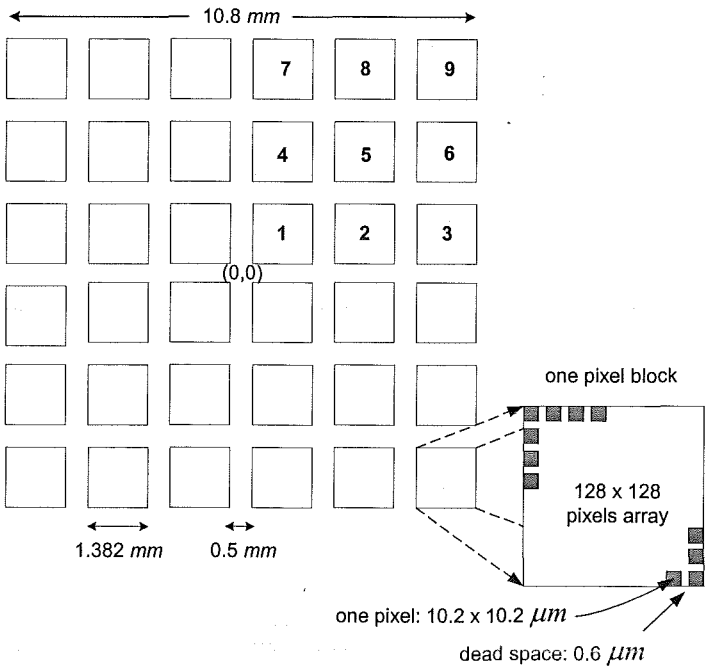

Figure 3.4: Physical dimension of a SLM scheme and pixel block scheme.

The parameter that describes the clipping of the Gaussian beam is known as the "clipping ratio γ", which is the ratio for the aperture of a modulator to the beam spot radius ω ($1/e^2$ intensity) [66,67]. This clipping will create higher order diffraction patterns (noise). This noise in turn can cause cross talk to other output channels, as well as increasing insertion loss and affecting the profile of the beam. An optical switch with low cross talk can be obtained if each output port avoids the entire high-order replay peaks of any hologram for all the input/output port configurations. Tan *et al*'s analyze beam profile versus cross talk for a $4f$ optical system [66]. When γ is between 2 and 4, the sidelobe rippling diminishes with increasing γ. Decreasing γ not only decreases the useable output power by blocking part of the collimated beam but also causes more power loss owing to diffraction effects, which steer the optical power to the sidelobe. They report that $\gamma > 2.5$ is necessary if the higher orders of diffraction are to be kept below –20dB of the Gaussian peak. It could be deduced that a γ value of greater than 2.6 is necessary to prevent a larger than 0.2 dB coupling power penalty. Therefore, the demand of illumination $\omega = 0.53\,mm$ can be achieved with the given clipping ratio ($\gamma = 2.6$) and pixel block dimension (1.382 *mm*).

3.2 Optical System Design

3.2.1 The procedures and modification techniques

In this section, four procedures for the lens design are given and some modification techniques to optimize the designed optical system are explored.

A. The procedures of the optical system design

- **Requirements**

  To start optical lens design, the first step is to collect and tabulate the requirements that need to be met. These could be [68]:

  - Image size (magnifications, and illumination uniformity).
  - Aperture, NA, and f-number.
  - Resolution or performance (aberration, alignment etc.).
  - Wavelength.
  - Space limitations.

- **Layout**

  The next step is to make an initial layout of the system, which will satisfy the above requirements [63]. This layout will simply arrange each component power (or, focal length) and spacing, which will produce the image at the required location, orientation, and of the required size. In addition, the material for lenses and lens surface quality and accuracy will be considered in this procedure.

- **Ray tracing**

  This process can be done by simulated optical design program. An important facet of this stage is to find a layout with minimized component focal lengths, less aberration residuals, and alignment errors [69].

- **Optimization**

  The final step is to optimize the optical system. Optical system can be optimized by lens itself, which was introduced in Section 2.2.3. Also, some useful modification techniques to optimize the entire optical system are listed below [63,68].

B. Modification techniques for lens system

- *Split an element into two or more components*

  In order to reduce the aberrations contribution, a significant factor is to split an element into two or more approximately equal parts whose total power is equal to the power of the original element. This allows the angles of the incidence to be reduced, and smaller angles introduce less aberration than larger ones

- *Raise the index of the positive singlets / lower the index of the negative singlets*

  The refractive characteristics of the materials used in a lens are obviously significant and important in optical design. Typically, for a positive element, the higher index is better, because it reduces the inward Petzval curvature which plagues most lenses. It also tends to reduce most of the other aberrations. In a negative element, the situation is less clear. A low index would increase the over-correcting contribution of a negative element. This can help to offset the inward or under-correction, which is a major problem in most lenses [53].

- *Compound a singlet into a doublet or triplet*

  In order to control the ray paths, a cemented interface into the element is introduced. Thus an Achromatic Doublet with a high-index positive element and a low-index negative element has the characteristic to flatten the Petzval field and to achieve achromatism [68].

- *Use of high f -number in compound lens*

  Clear aperture is the light effective diameter of a lens. For minimal aberrations, only the central portion of the lens should be illuminated. Therefore, a bulk lens is often considered [60].

Due to above discussion, a flowchart of the design procedure for our optical system is organized as shown in Figure 3.5

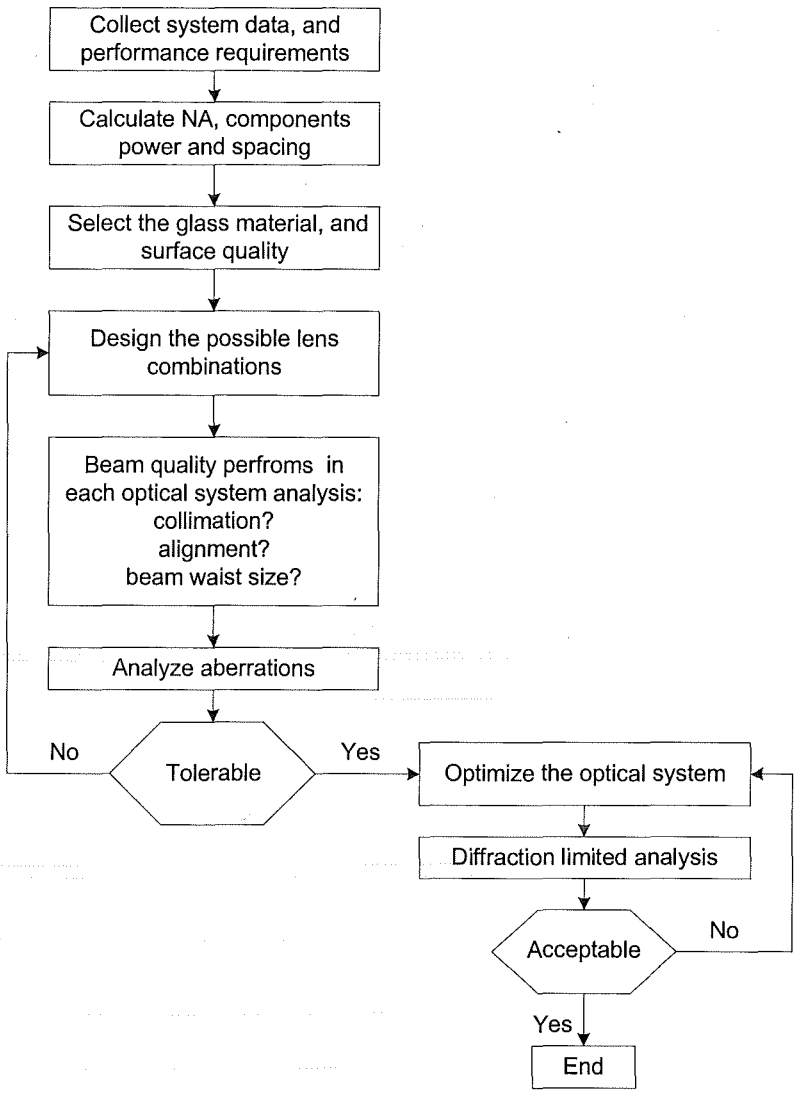

Figure 3.5: The flowchart for design the optical system

3.2.2 Computation of the elements power and spacing

The single-mode fibers Corning SMF-28 are utilized for the input/output fibers. SMF-28 has the numerical aperture 0.13, the core radius 5 μm, and the cladding radius 125 μm. By Eq. (2.9), Gaussian beam has the radius of 5.18 μm emitting from the end of the SMF-28 input port. The beam radius required for illuminating the pixel block is 0.53 *mm*. Therefore, the designed optical system needs to magnify is 102.3.

In order to collimate the divergent Gaussian beams in free space, each optical component has the space (the object distance) equal to the lenses' focal length ($S = f$). So the image distance will be equal to the lens' focal length ($S" = f$) by Eq. (2.13). In

addition, the magnification of the lens is $M = f/z_R$. The Rayleigh range z_R is 54.4 μm, using Eq. (2.5).

From Eqs. (2.15) and (2.16), the image distance S'' and the beam magnification M have the functions of the object distance S, lens' focal length f, and the Rayleigh range z_R. Thus, in order to compute the component power and the space of the optical system, two factors need to be considered:

- The effect of f on the lens magnification M is $M = f/z_R$. In order to achieve the beam scaling on the first SLM of M = 102.3, the element power f should be as large as possible.

- Meanwhile, increase in f makes the image size to be sensitive to the beam's collimation and deviation from the object distance. These two points indicate that the component power f should be as small as possible.

  Sensitivity to the beam's collimation: a Gaussian beam emits from the input fiber port has the divergence 0.35 radian (or, 20 deg) in free space; and the Rayleigh range is 54.4 μm. In order to collimate the divergent beam, lens power f must be close the value of the Rayleigh range. Therefore, the focal length f should design as small as possible. Thus, the concept of a microlens array and one or more macro-lenses combination is considered. The microlens array is to collimate divergent beams emitting from the input array; and then utilize one or more macro-lenses to magnify and align beams to the 1st SLM.

  Sensitivity to deviation from the object distance: this is due to the optical component cannot be placed at the exactly position in practice. As reported by S. A. Self [59]: if a Gaussian beam is collimated by a lens, and the object distance S and the lens' focal length f has the range of $f - z_R \le S \le f + z_R$ (the deviation is $\Delta S = 2z_R$), then the image distance S'' will have the range of $f - f^2/(2z_R) \le S'' \le f + f^2/(2z_R)$, and the deviation of image distance is $\Delta S'' = f^2/z_R$. In order to reduce the deviation of image distance range $\Delta S''$, choosing a small f component is necessary.

From the above analysis, we propose some possible focal lengths f for the microlens; they are 125, 200, 250, 300, 450 and 500 μm. By Eq. (2.15), and setting the focal length f as 125, 200, 250, 300, 450 and 500 μm, we can get the graphs for (S/f) versus $(S"/f)$ at various values of parameter (z_R/f) as shown in Figure 3.6. This figure shows that when (S/f) is in the range of -1 to 3, the variation of the parameter (z_R/f) for $f = 500\mu m$ has the steepest change, and the parameter (z_R/f) for $f = 125\mu m$ varies gradually.

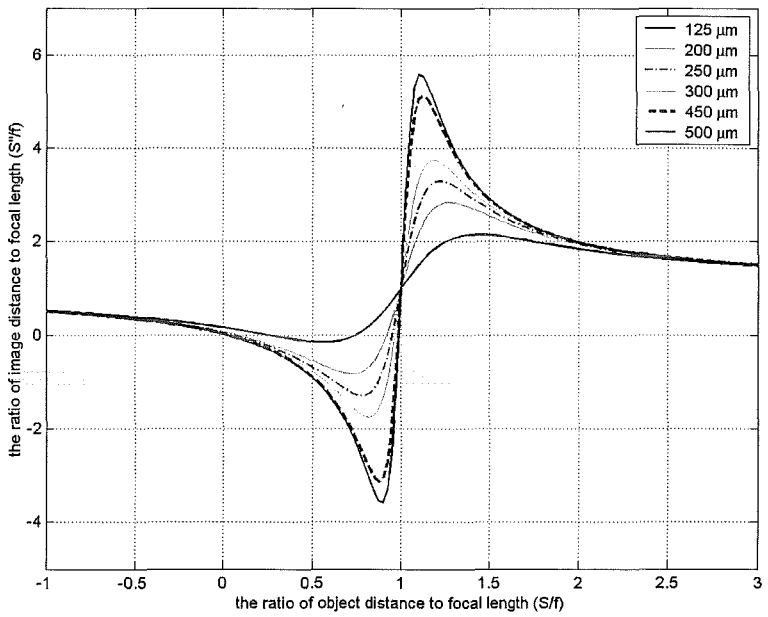

Figure 3.6: Plot of (S/f) versus $(S"/f)$ for the various values of (z_R/f)

The deviation of object distance due to the manufacturing process: if we consider the object distance has a typical deviation of $\pm 2\% f$ due to the manufacturing process, then the variance of (S/f) versus $(S"/f)$ for various parameters (z_R/f) is shown in Figure 3.7. It shows that if the parameter (z_R/f) is large, i.e., $f = 125\mu m$ or $f = 200\mu m$, then the ratio of $(S"/f)$ on the image plane changing is smooth. This means that the deviation of the image distance is small, so that we can easily adjust the correct position for each component. However, when (z_R/f) is small, i.e., $f = 450\mu m$ or $f = 500\mu m$, then the range of defocusing is wider and harder to adjust. Table 3.1 presents the deviation of the image distance for every proposed microlens.

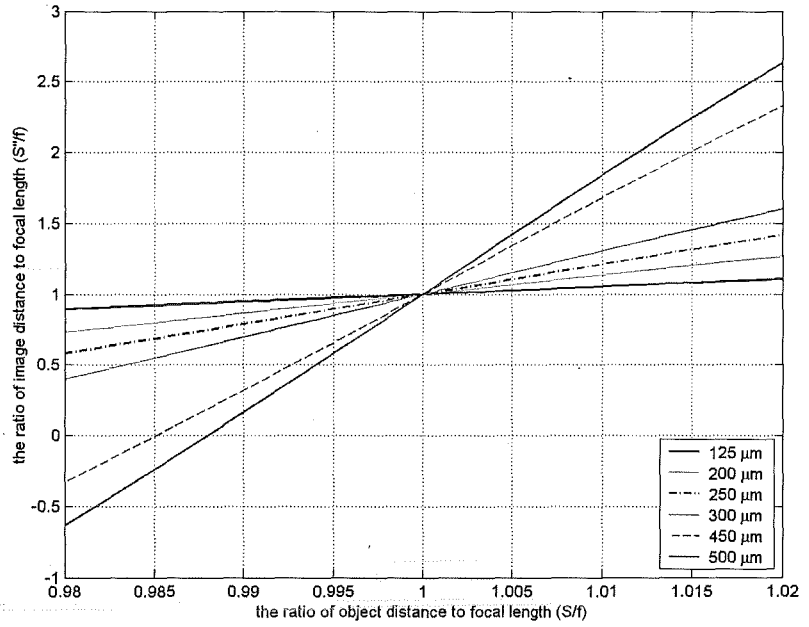

Figure 3.7: The deviation ranges of image distance for six different focal lengths of microlens at its ± 2% object distance if $S = f$.

Table 3.1: Possible deviation ranges of the image distance (unit: μm).

Microlens power f_1	The deviation of ± 2% f_1 of the object distance	Possible deviation of the image distance
125	2.5	15.175
200	4	61.93
250	5	120.5
300	6	207.4
450	9	688.14
500	10	937.25

From above analyses and considering the minimum required distance $d_{\min}$, we design another two macro-lenses in our optical system. The process to compute these two macro-lenses and the microlens power is as follows. We assume that the input fiber is on the optical axis, and each of the lenses in the optical path are separated by a distance equal to the sum of their focal lengths as shown in Figure 3.8.

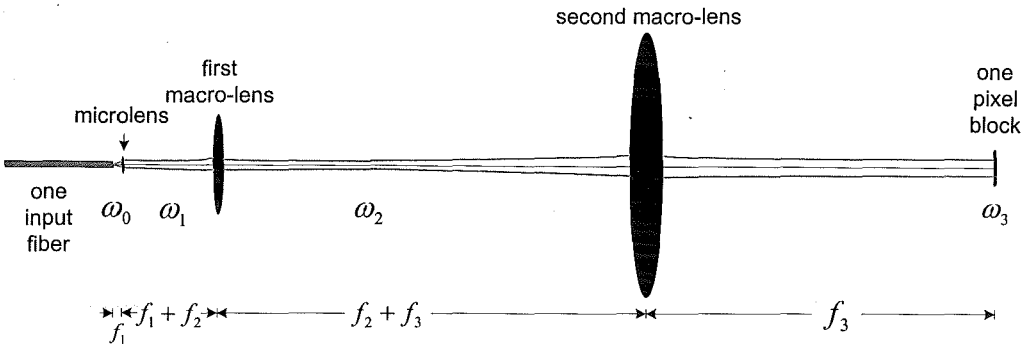

Figure 3.8: One microlens and two macro-lenses used as our optical system

In Figure 3.8, ω_0 is the radius of input beam, ω_1 and ω_2 are the beam waist radii at their Rayleigh ranges, ω_3 is the beam radius illuminated on the pixel block, f_1 is the focal length of microlens, and f_2, f_3 are the focal lengths of two macro-lenses respectively. By Eqs. (2.4), (2.16), and the magnification for each lens, the system power has the relationships as follows

$$\omega_3 = \frac{f_3 f_1 \lambda}{\pi f_2 \omega_0} \tag{3.1}$$

where $\omega_0 = 5.18\,\mu m$ and $\omega_3 = 0.53\,mm$. Then, the three component powers have the relationship of

$$\frac{f_1 f_3}{f_2} = \frac{\omega_0 \omega_3 \pi}{\lambda} = 5.56\,mm$$

The second component power f_2 can be 12.5 *mm*, because it is a commonly available size thereby removing the need for customization and reducing cost. Then, the possible values for the focal length of the third component, f_3, and the resulting distance between the input fiber and the 1st SLM are listed in Table 3.2.

Table 3.2: Components power and their total dimensions (the second lens $f_2 = 12.5$ mm)

f_1 of the microlens	The magnification of the microlens	The ratio of f_3/f_2	f_3 of the third lens	Total dimension
125 μm	2.5	44.5	556.3 *mm*	1138 *mm*
250 μm	5	22.2	277.5 *mm*	580.5 *mm*
300 μm	6	18.5	231.25 *mm*	488 *mm*
450 μm	9	12.4	155 *mm*	336 *mm*
500 μm	10	11.1	138.8 *mm*	303.6 *mm*

Comparing from Table 3.2, we choose f_1 = 450 μm for the power of the microlens. The reasons are:

- The total dimension 336 *mm* satisfies the compact size requirement.
- The space 155 *mm* from the third lens to the first SLM is close to the minimum required distance $d_{\min}$ 147.4 *mm*.
- Two macro-lenses can be easily found in the market catalogs.

3.2.3 Optical material and lens surface condition

Having computed the components power and the spacing of the optical system, the next step is to consider the lens material and its surface condition. The lens surface condition can be described by two items; surface quality and surface accuracy (or, surface irregularity). These factors will affect the performance of the optical system. In summary, the optical material we select is BK7, lens surface quality of 40-20 scratch-dig is the best choice, and surface accuracy from $\lambda/4$ to $\lambda/8$ irregularity is adequate. The details of these are listed below:

Glass material

For telecommunication application at near infrared ($\lambda \sim 1550$ nm), the following factors are significant consideration for the lens material selection: excellent homogeneity, low thermal expansion, laser damage resistance, and high transmission [53]. BK7 has the features that satisfy the above requirements, and the price is reasonable as well. BK7 has the index of 1.50065 at 1550 nm and its transmission rate is 91.5%. Coating technology can be used to improve the transmission rate to 99% or higher. Typically, the standard material index tolerance of BK7 is ± 0.001 [70].

Lens surface quality

Surface quality refers to the finish of the defects surface, and includes such defects as pits, scratches, incomplete polish, stains, and so on. The surface quality is specified by a number such as 80-50, in which the first two digits relate to the apparent width of a tolerable scratch and the second two digits indicate the diameter of a permissible dig, pit, or bubble in hundredths of a millimeter. Thus, a surface specification of 80-50 would permit a scratch of an apparent width, which matched (by visual comparison) a #80 standard scratch and a pit of 0.5-mm diameter. The total length of all scratches and the number of pits are also limited by the specification [53]. Surface qualities of 80-50 or larger are easily fabricated. Qualities of 60-40 and 40-30 command a small premium in

cost. Surfaces with quality specifications of 40-20, 20-10, 10-5, or similar combinations require extremely careful processing, and are considerably more expensive to fabricate [63]. For demanding laser imaging systems with focused beams, and moderate cost, the 40-20 scratch-dig is chosen [70].

Lens surface accuracy

Surface accuracy refers to the dimensional characteristics of a surface, i.e., the value and uniformity of the radius. Surface accuracy is specified in terms of the wavelength of light from a sodium lamp (589.3 nm) or a He-Ne laser (632.8 nm). The surface accuracy is determined by an interferometer comparison of the surface with a test plate gauge by counting the number of fringes and examining the regularity of the rings. The space between the surface of the work and the test plate changes one-half wavelength for each fringe. The accuracy of the fit between work and gauge is described in terms of the number of fringes seen when the gauge is placed in contact with the work. The radius of a test plate is frequently known only to an accuracy of about one part in a thousand or one part in ten thousand. A fit of from five to ten rings, with a sphericity (or "regularity") of from one-half to one ring is not a difficult tolerance. The usual ratio is to have a fit of no worse than 4 or 5 times the maximum allowable irregularity. For surface accuracy, $\lambda/4$ to $\lambda/8$ irregularity should be selected. It should avoid specifying accurate surfaces on pieces whose thickness-to-diameter ratio is low. This is because such elements tend to spring and warp in processing, and extreme precautions are necessary to hold an accurate surface figure [53,68].

3.2.4 Design the possible lens combinations

In Section 3.2.2, the power and the spacing of the three lenses were computed; the focal lengths are 450 μm, 12.5 *mm* and 155 *mm*. whilst the 450 μm microlens array is custom made, the 12.5 *mm* and 155 *mm* macro-lenses can be found in the market catalogs. In order to have high f-numbers in the first and second lenses, bulk lenses for the first and second macro-lenses are considered. Thus, only the central portion of the lenses should be illuminated to reduce the system aberrations. The configuration of lens combination is illustrated in Figure 3.9. This figure summarizes the paraxial properties of the system. A Gaussian beam emits from a single-mode fiber, with a numerical aperture of 0.13 and perpendicular to the object plane, into the designed optical system. Then, the microlens array converts the numerical aperture of the beam to 0.096. The beam is collimated and magnified by the microlens and the first macro-lens, and then aligned by passing through the second macro-lens to shine on the first SLM.

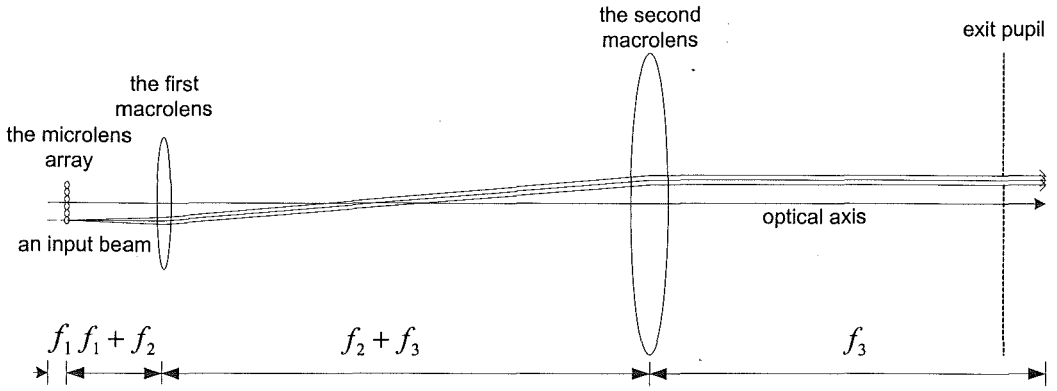

Figure 3.9: The configuration of lens combination

In Figure 3.9, the exit pupil is the image of the aperture stop as seen from an axial point on the image planet through the interposed lenses. Aperture stop is defined as the maximum angle of a ray from the object to the image.

The two macro-lenses, with focal lengths of 12.5 *mm* and 155 *mm,* are selected with optical layouts having combinations of plano-convex, plano-concave, and achromatic doublet (as reviewed in Section 2.2.3). Thus, the possible combinations of the optical layout are listed in Table 3.3.

Table 3.3: The specifications of the four optical combination layouts

Optical layout	microlens	1st macrolens	2nd macrolens
Concave-convex	450 μm convex-plano lens	-12.5 *mm* concave - plano lens (KPC013)	150 *mm* plano -convex lens (KPX100)
Concave-Achromatic doublet		-12.5 *mm* concave - plano lens (KPC013)	150 *mm* Achromatic doublet (PAC058)
Convex-convex		12.5 *mm* convex - plano lens (KPX013)	150 *mm* plano -convex lens (KPX100)
Convex-Achromatic doublet		12.5 *mm* convex - plano lens (KPX013)	150 *mm* Achromatic doublet (PAC058)

These four lenses are selected from the Newport Inc. lens catalog. The -12.5 *mm* plano-concave lens (KPC013) and/or 12.5 *mm* plano-convex (KPX013) may be the first macro-lens; while the 150 *mm* plano -convex lens (KPX100) and/or the 150 *mm* Achromatic doublet (PAC058) may be the second macro-lens[7]. Those lenses satisfy the requirements of optical quality: optical material is BK7, the surface accuracy is $\lambda/4$ or $\lambda/8$, and surface quality is 40-20 scratch-dig. For technical reason, two plano-faces can be used as a back-to-back configuration. This is because these combination of lenses can balance the spherical aberration in situations where the object and image are at unequal

[7] Note that the last two lenses are not accordant with the focal length we required. However, we will modify the lens position to optimize our system in chapter 5.

distances from the lens. Achromatic doublet (PAC058) is composed of two elements, a positive crown glass element (BK7) cemented to a negative flint glass element (SF5). The lens drawings are shown in Appendix B.

3.2.5 Design the microlens array

Having determined the optical power and the spacing of the microlens in the previous section, the configurations of the microlens array can be designed [71,72]. The configuration of the 450 μm microlens array is listed below and illustrated in Figure 3.10.

- Aperture diameter: 160 μm
- Lens shape: convex-plano ($R_1 = 225.3\ \mu m,\ R_2 = \infty$)
- Lens material: BK7 (n =1.50065; λ at 1550 nm)
- Center thickness: 24 μm
- Edge thickness: 6.8 μm

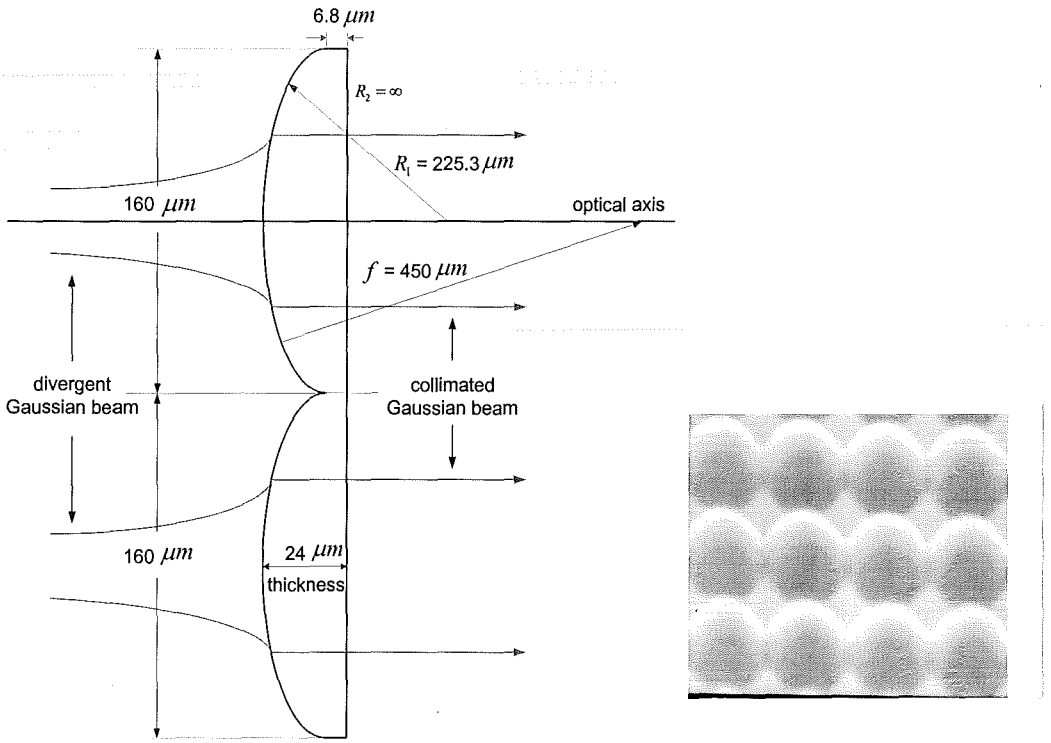

Figure 3.10: The configurations of the 450 μm microlens array

In Figure 3.10, R is the surface curvature of the microlens, and f is its focal length. This design also determines that each single-mode fiber has a 160 μm space on input and output arrays.

3.3 Beam Performances of the Four Layouts

Having designed the four layouts of the optical system, the next step is the ray tracing. By ray tracing, the beam performances and the aberration effects in the optical system can be investigated. These four layouts will be simulated by using the optical program Zemax [69]. Each layout will simulate for the assigned ports; they are port 1, 2, 3, 5, 6, and 9, which has illustrated in Figure 3.3, Section 3.1.2. In the following sections, we will present four layouts of beam qualities illuminating on the first SLM. The analysis of aberration effects will be explored in the next chapter. All figures showing the simulation results are based on the performance of port 1 for each layout; while other ports' data will be listed in tables.

3.3.1 The Concave - convex lenses layout

The Concave-convex layout consists of the 450 μm microlens array, the -12.5 *mm* plano-concave lens (KPC013) and the 150 *mm* plano-convex lens (KPX100). The lens drawings of KPC013 and KPX100 are presented in Appendix B.

The KPC013 has 6.35 *mm* aperture diameter and the center thickness is 2.5 *mm*. The material is BK7 and it has $\lambda/4$ surface accuracy and 40-20 scratch-dig surface quality. The tolerance of focal length is ± 1 %. The KPX100 has 25.4 *mm* aperture diameter and the center thickness is 25.943 *mm*. It has $\lambda/4$ surface accuracy and 40-20 scratch-dig surface quality. The two plane surfaces of the two lenses are designed as a back-to-back configuration. The lens prescription of the Concave-convex layout is listed below:

Lens prescription:

Radius	thickness	glass	index	semi-aperture
Infinity	0.45	air		0.000011
0.2253	0.024	BK7	1.50065204	0.08
infinity	12.95	air		0.050947
-6.46	2.5	BK7	1.50065204	3.175
infinity	133.19	air		3.175
infinity	4.047	BK7	1.50065204	12.7
-77.52	150	air		12.7

Effective Focal Length = 3.24 *mm*
Back Focal Length = -2037.8 *mm*
Total Track = 303.15 *mm*
Working F/# = 615.4

The simulation results show that the beam illuminating the port 1 pixel block has the beam radius $1.432\ mm$, curvature radius $2.2\times10^{3}\ mm$, and the divergent angle 0.0155

radians. The divergent angle is small enough that we can treat it as a collimated beam. Figure 3.11 shows the port 1 beam shining on its pixel block. The beam diameter is much larger than the size of the pixel block (1.382 *mm* × 1.382 *mm*). Thus, the result implies that beams contribute cross talk to other ports. In addition, the illuminating light on the pixel block is de-centered, and is not a perfect circle. That is, of course, distortion has occurred in each pixel block. From ZEMAX analysis data, the beam transmission efficiency is 89.66%, (or 0.474dB). The results for other ports are listed in Table 3.4. This table shows that every port has the same results; they are de-centered, over spread out on their pixel blocks and beam shapes have distortion. The average power efficiency for this layout is 89.65%.

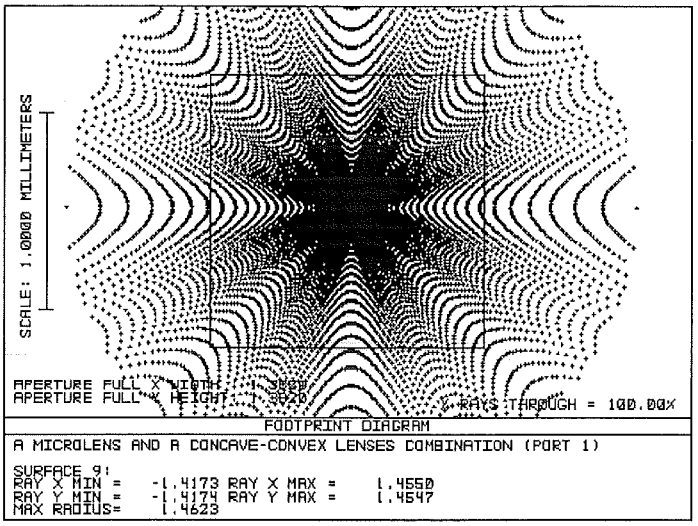

Figure 3.11: Beam shines on pixel block of the Concave - convex lenses layout

Table 3.4 Beams illuminate on their pixel blocks of the Concave - convex lenses layout[8]

Port #	1	2	3	5	6	9
On x axis*	-1.4173 1.4550	-1.3808 1.4883	-1.3412 1.5216	-1.3799 1.4875	-1.3403 1.5207	-1.3386 1.5195
On y axis*	-1.4174 1.4547	-1.4168 1.4542	-1.4155 1.4531	-1.3800 1.4871	-1.3784 1.4863	-1.3386 1.5191
Efficiency	89.66%	90.18%	89.19%	89.74%	89.63%	89.48%
Efficiency	-0.4740dB	-0.4489dB	-0.4983dB	-0.4701dB	-0.4755dB	-0.4827dB
Average radius	1.432	1.435	1.433	1.434	1.431	1.429

[8] All data are measured from the centered of pixel block and the unit is mm.

3.3.2 The Concave - Achromatic doublet layout

The Concave-Achromatic doublet layout consists of the 450 μm microlens array, the -12.5 *mm* plano-concave lens (KPC013) and the 150 *mm* achromatic doublet (PAC058). The lens drawing of PAC058 is presented in Appendix B.

The PAC058 150 *mm* Achromatic doublet has the same aperture size as KPX100. PAC058 consists of a positive low-index crown glass lens element (f_{FFL} = 147.1 *mm*, BK7, and center thickness 2.167 *mm*) cemented to a negative high-index flint glass lens element (f_{BFL} = -148.9 *mm*, SF5, and center thickness 4.0 *mm*). PAC058 has the focal length tolerance of ± 2 %. The surface quality is 40-20 scratch-dig and surface accuracy is $\lambda/8$. The lens prescription of the Concave-Achromatic doublet layout is as follows:

Lens prescription:

Radius	thickness	glass	index	semi-aperture
Infinity	0.45	air		0.000011
0.2253	0.024	BK7	1.50065204	0.08
infinity	12.95	air		0.050947
-6.46	2.5	BK7	1.50065204	3.175
infinity	132.96	air		3.175
200.644	2.167	BK7	1.50065204	12.7
-67.225	4	SF5	1.64332172	12.7
-91.273	148.9	air		12.7

Effective Focal Length = 3.9 *mm*
Back Focal Length = -2437.95 *mm*
Total Track = 303.9 *mm*
Working F/# = 705

The simulation results show that the beam illuminating the port 1 pixel block has the beam radius $1.421\,mm$, curvature radius $2.6\times10^{3}\,mm$, and the divergent angle 0.0129 radians. The divergent angle is small; so that we can treat the beam is collimated. Figure 3.12 shows the port 1 beam shining on its pixel block. The beam diameter is much large than the size of pixel block, and this result is same as the previous layout. From ZEMAX analysis data, the beam transmission efficiency is 89.78%, (or 0.4683dB). The measurements of other ports are listed in Table 3.5. This table shows that every port has the same results; they are de-centered, over spread out on their pixel blocks and beam shapes have distortion. The average power efficiency for this combination is about 89.78%. The performance of this layout is similar to the first one.

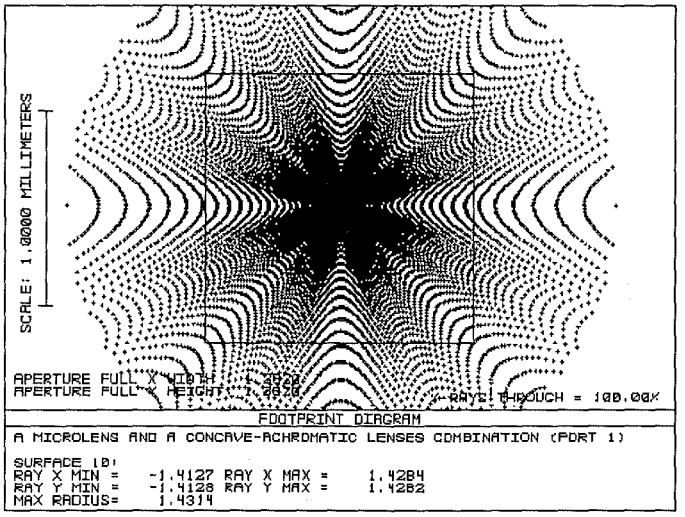

Figure 3.12: Beam shines on pixel block of the Concave - achromatic doublet layout

Table 3.5: Beams illuminate on their pixel block of the Concave - achromatic doublet layout[9]

Port #	1	2	3	5	6	9
On x axis*	-1.4127 1.4284	-1.3985 1.4420	-1.3798 1.4594	-1.3971 1.4425	-1.3778 1.4607	-1.3738 1.4636
On y axis*	-1.4128 1.4282	-1.4123 1.4284	-1.4112 1.4288	-1.3972 1.4423	-1.3948 1.4441	-1.3739 1.4633
Efficiency	89.64%	89.97%	90.11%	89.46%	89.63%	89.86%
Efficiency	-0.4750dB	-0.4590dB	-0.4523dB	-0.4837dB	-0.4755dB	-0.4643dB
Average radius	1.421	1.420	1.420	1.42	1.42	1.418

[9] All data are measured from the centered of pixel block and the unit is mm.

3.3.3 The Convex - convex lenses layout

The Convex-convex layout consists of the 450 μm microlens array, the 12.5 *mm* plano-convex lens (KPX013) and the 150 *mm* plano-concave lens (KPX100). The lens drawing of KPX013 is presented in Appendix B.

The 12.5 *mm* KPX013 plano-convex lens has a 6.35 *mm* aperture diameter and its center thickness is 3.819 *mm*. KPX013 has the surface accuracy of $\lambda/4$ and the scratch-dig surface quality is 40-20. The tolerance of focal length of the KPX013 is ± 1 %. The two plane surfaces of the two lenses are designed as a back-to-back configuration. The lens prescription of the Convex-convex layout is as follows:

Lens prescription:

Radius	thickness	glass	index	semi-aperture
Infinity	0.45	air		0.000011
0.2253	0.024	BK7	1.50065204	0.08
Infinity	12.95	air		0.050947
6.563	3.819	BK7	1.50065204	3.175
Infinity	159.83	air		3.175
Infinity	4.047	BK7	1.50065204	12.7
-77.52	150	air		12.7

Effective Focal Length = -5.4 *mm*
Back Focal Length = 239.6 *mm*
Total Track = 331.11 *mm*
Working F/# = 1026.45

The simulation results show that the beam illuminating on the pixel block has much better performance than the previous two layouts. The illumination on the port 1 pixel block has the beam radius $0.6162\,mm$, curvature radius $-89.9\,mm$, and the divergence 0.0093 radians. Due to the small divergent angle, the beam can be treated as collimated. In addition, the beam collimation is better than the previous two layouts.

Figure 3.13 shows the port 1 beam superimposed on its pixel block. The figure presents that beam is well collimated and aligned on its pixel block. The results of other ports are listed in Table 3.6. The table indicates that all ports of beams are well collimated and aligned on the pixel blocks. However, each port has a tiny amount of de-centering and distortion, except ports 5 and 9. Table 3.7 presents the averaged beam radius $0.6127\,mm$ and the average standard deviation 0.0026 *mm*, (or 0.424%).

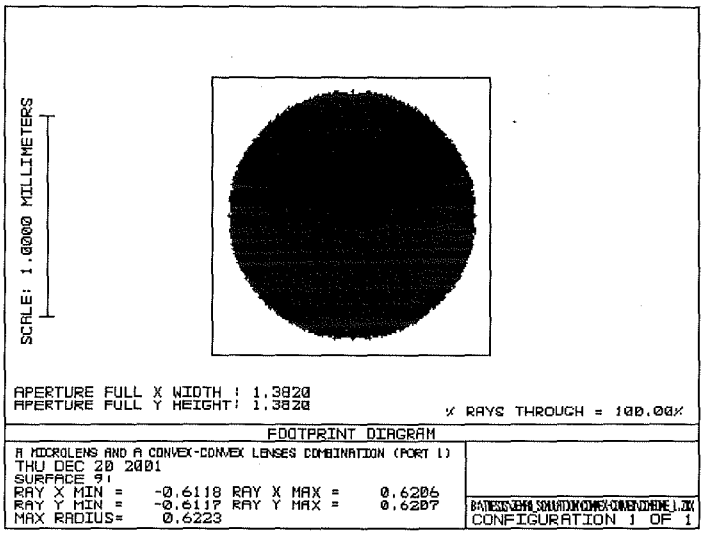

Figure 3.13: Beam shines on pixel block of the Convex - convex lenses layout

Table 3.6: Beams illuminate on their pixel block of the Convex - convex lenses layout[10]

Port #	1	2	3	5	6	9
On x axis*	-0.6118 0.6206	-0.6038 0.6246	-0.5925 0.6279	-0.6032 0.6240	-0.5919 0.6273	-0.5904 0.6262
On y axis*	-0.6117 0.6207	-0.6109 0.6200	-0.6094 0.6186		-0.6014 0.6228	
Average radius	0.6162	0.6148	0.6121	0.6136	0.6109	0.6083
Max radius[11]	0.6223	0.6253	0.6283	0.6268	0.6288	0.6296

Table 3.7: Average beam size and its S.D. of the Convex - convex lenses layout

Average radius	Standard deviation	
0.6127 *mm*	0.0026 *mm*	0.424%

[10] All data are measured from the centered of pixel block and the unit is mm.

[11] Max radius is the max distance, which measures from the center of pixel block to the edge of the beam. However, due to beam is little de-centering in pixel block, so the max radius become meaningless.

3.3.4 The Convex - Achromatic doublet layout

The Convex-Achromatic doublet layout consists of the 450 μm microlens array, the 12.5 *mm* plano-convex lens (KPX013) and the 150 *mm* Achromatic doublet (PAC058). The lens prescription of the Convex-Achromatic doublet layout is as follows:

Lens prescription:

Radius	thickness	glass	index	semi-aperture
Infinity	0.45	air		0.000011
0.2253	0.024	BK7	1.50065204	0.08
infinity	12.95	air		0.050947
6.563	3.819	BK7	1.50065204	3.175
infinity	161.4	air		3.175
91.273	4	BK7	1.50065204	12.7
-67.225	2.167	SF5	1.64332172	12.7
-200	147.1	air		12.7

Effective Focal Length = -5.27 *mm*
Back Focal Length = 232.2 *mm*
Total Track = 331.9 *mm*
Working F/# = 921

The simulation results show that this layout has the similar performance to the previous one. The illumination on the port 1 pixel block has the beam radius $0.6079\ mm$, curvature radius $-85\ mm$, and the divergence 0.0095 radians. Due to the small divergent angle, the beam can be treated as collimated.

Figure 3.14 shows the port 1 beam superimposed on its pixel block. The figure presents that beam is well collimated and aligned on its pixel block. The results of other ports are listed in Table 3.8. The table indicates that all ports of beams are well collimated and aligned on the pixel blocks. However, each port has a tiny amount of de-centering and distortion, except ports 1, 5 and 9. Table 3.9 presents the averaged beam radius $0.6048\ mm$ and the average standard deviation 0.0027 *mm*, (or 0.44%).

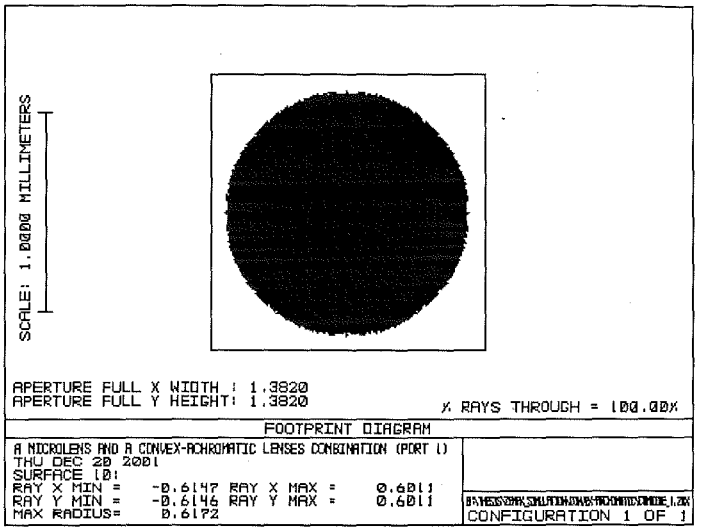

Figure 3.14: Beam shines on pixel block of the Convex - achromatic doublet layout

Table 3.8: Beams illuminate on their pixel block of the Convex - achromatic doublet layout[12]

Port #	1	2	3	5	6	9
On x axis*	-0.6147	-0.6293	-0.6293	-0.6288	-0.6407	-0.6396
On y axis*	0.6011	0.5824	0.5824	0.5818	0.5620	0.5605
		-0.6139	-0.6139		-0.6274	
		0.6004	0.6004		0.5803	
Average radius	0.6079	0.6065	0.6065	0.6053	0.6026	0.6001
Max radius	0.6172	0.6301	0.6301	0.6369	0.6456	0.6516

Table 3.9: Average beam size and its S.D. of the Convex - achromatic doublet layout

Average radius	Standard deviation	
0.6048 *mm*	0.0027 *mm*	0.446%

[12] All data are measured from the centered of pixel block and the unit is mm.

3.4 Discussion

In this chapter, we designed the possible lens layouts to be our optical system. Also, we presented the beam quality performances on the first SLM for these four layouts. At beginning, we considered the system requirements and discussed the design procedures. Next, the design of a microlens array in the optical system was explored. Also the two macro-lenses were designed. Finally, the performances for the four layouts were simulated.

The simulation data showed that these four optical layouts achieved beam collimation on the pixel blocks. The average divergent angle is about 0.01 radians. Also, the third layout (Convex-convex layout) has the best collimation result, the divergence is 0.0093 radians. The next one is the fourth layout (Convex-Achromatic doublet combination), which has the divergent angle of 0.0095 radians.

The third and fourth layouts achieved better alignment and illumination on the pixel block. Although Table 3.6 and Table 3.8 indicated these two layouts have tiny de-center and distortion illuminated on the pixel blocks, they are still acceptable. One issue for these two layouts is that the beam size on the pixel block (0.6127 *mm* and 0.6048 *mm* respectively) is larger than our requirement (0.53 *mm*). Thus, these two layouts need to optimize to address this issue.

Typically, the third layout has better uniform beam size shining on the first SLM than the fourth layout. The former has averaged standard deviation 0.0026 *mm*, and the later is 0.0027 *mm*. We can compare them from Table 3.7 and Table 3.9. Moreover, the third layout has less beam de-centering on the pixel blocks than the fourth layout.

The first and second layouts generated virtual images on the first SLM, because both of them have the negative back focal lengths. Figure 3.11 and Figure 3.12 showed that beams were defective on the first SLM. In addition, it is obvious to see that beams spread outside the pixel blocks and become crosstalk to other ports. The average power losses are 0.474 dB and 0.4683 dB respectively. The reason for the illumination spreads outside the square is that the distance between the convex or (Achromatic doublet) and the concave lenses was large. This will cause the beam to diverge more widely. Moving the third lens close to the plano-concave lens or put one more convex lens to collimate the over-divergent light can solve this problem.

To sum up, the first and second layouts are not ideal for our optical system. On the other hand, the third and fourth layouts have acceptable performance. Although both of them

produce larger beam sizes on the pixel blocks than our requirement, they can be optimized by some modified techniques. We will address this issue in Chapter 5.

Chapter 4

Analysis the Aberration Effects on the 1st SLM

In Chapter 3, we designed four optical system layouts and investigated the beams performance. In this chapter, we will analyze the aberration effects shown on the pixel blocks by utilizing Zemax software program [69]. The aberrations will be presented by three perspectives: system optical path difference (OPD), wavefront error, and transverse aberration. OPD is the difference of the wavefront from the reference sphere. OPD is expressed by a number and the unit is the beam wavelength (λ). Less OPD indicates less aberration. Wavefront error and transverse aberration can be detected by observing the pattern of the aberration itself and may also be computed in a polynomial form. Therefore, we can understand the types of aberrations and their coefficients for each layout. Finally, the comparison of aberrations for these four layouts will be discussed.

The results show that every port in each layout has the same types of aberrations, and a close aberration coefficients as well. Thus, we present the aberration data in port 1 as the layout's aberration effect. Also, the simulation data show that four layouts produce the same types of aberrations on the 1st SLM. They are: spherical aberration, defocusing, and de-centering. However, Coma and Astigmatism are not shown. In addition, the Convex-convex lenses layout performs the least aberration on the 1st SLM.

4.1 Analysis of aberration with Four Layouts

4.1.1 The Concave-convex lenses layout

To simplify aberrations analysis, we consider tangential (PY, y-axis) fan and sagittal (PX, x-axis) fan of the port 1 rays tracing through the optical system. The OPD (W) of the Concave-convex layout on tangential pupil (PY) and sagittal pupil (PX) are plotted in Figure 4.1. Where PY and PX are normalized by the exit pupil (The exit pupil is illustrated in Figure 3.9, Section 3.2.4). The result shows that the port 1 has the maximum P-V (peak-to-valley) OPD of 0.2055 waves. Due to the positive value of OPD, the actual

wavefront is ahead of the reference sphere. Other ports of the maximum P-V OPD are listed in Table 4.1. The table shows that OPD value for each port decreases from center port to outer port on SLM.

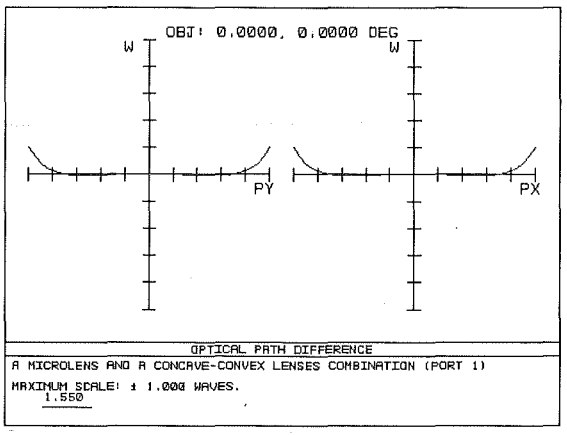

Figure 4.1: OPD of the Concave-convex layout.

Table 4.1:The maximum OPDs of the Concave-convex layout.

Port #	1	2	3	5	6	9
OPD $(unit:\lambda)$	0.2055	0.2042	0.2016	0.2020	0.2001	0.1932

Figure 4.2 shows the wavefront aberrations of the Concave-convex layout at the exit pupil.

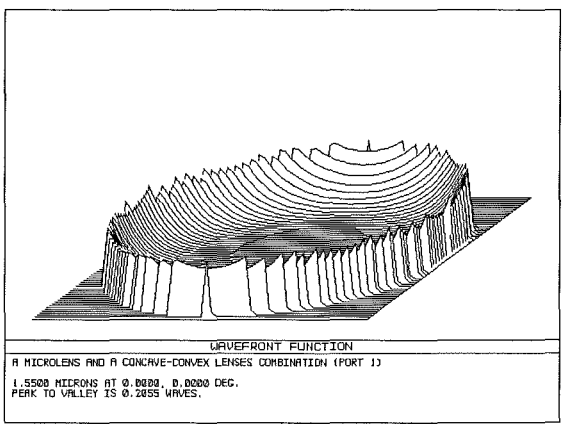

Figure 4.2: The wavefront aberrations for the Concave-convex layout at 1550 nm, for the field angle of 0 deg

In Figure 4.1, $W(0,y)-PY$ and $W(x,0)-PX$ can be expressed as two polynomials:

$$W(0,y)=W(PY)=0.05095\,PY^4+0.61\,PY^2+0.47\,PY \tag{4.1}$$

$$W(x,0)=W(PX)=0.05095\,PX^4+0.61\,PX^2+0.47\,PX \tag{4.2}$$

From Eq. (2.22), $W(0,y)$ and $W(x,0)$ can be expressed as

$$W(0,y) = A y^4 + B y^3 + (3C + D) y^2 + E y + F \tag{4.3}$$

$$W(x,0) = A x^4 + (C + D) x^2 + F \tag{4.4}$$

Therefore, using Eqs. (4.1) to (4.4), we can find each type of aberration and its coefficient presents at the exit pupil. They are shown in Table 4.2.

Table 4.2 The wavefront Aberration coefficients of the Concave-convex layout

A: Spherical aberration coefficient	0.05095
B: Coma coefficient	0
C: Astigmatism coefficient	0
D: Defocusing coefficient	0.61
E: De-centering coefficient	0.47
F: Constant or piston term	0

This table presents that the Concave-convex layout generates spherical aberration (A), defocusing (D), and de-centering (E). Spherical aberration coefficient A is positive because the actual wavefront is ahead of reference sphere. However, Coma and Astigmatism are not present in this layout, because both coefficients B and C are zero. Defocusing is the distance of the pixel block from a Gaussian beam waist. The positive value presents that the beam waist is located in front of the SLM, while the negative value means that beam waist has not formed before it hits the SLM. One reason for defocusing is due to the title angle (7^0) of the SLM itself. De-centering is the deviation of a Gaussian beam from the center of the pixel block.

The transverse aberrations shown on each pixel block can be computed from Eqs. (4.1) and (4.2). Using Eqs. (2.27), (2.28), (4.1) and (4.2), the transverse aberrations for tangential fan $TA_y(0,y)$ and sagittal fan $TA_x(x,0)$ on the pixel block are given as

$$TA_y(0,y) = EY = -3.84PY^3 - 23.15PY - 8.77 \tag{4.5}$$

$$TA_x(x,0) = EX = -3.84PX^3 - 23.15PX - 8.77 \tag{4.6}$$

where EY and EX represent the transverse aberration on y and x axes respectively. The unit of TA is μm. The transverse aberrations on y- and x-axes of the pixel block are shown in Figure 4.3.

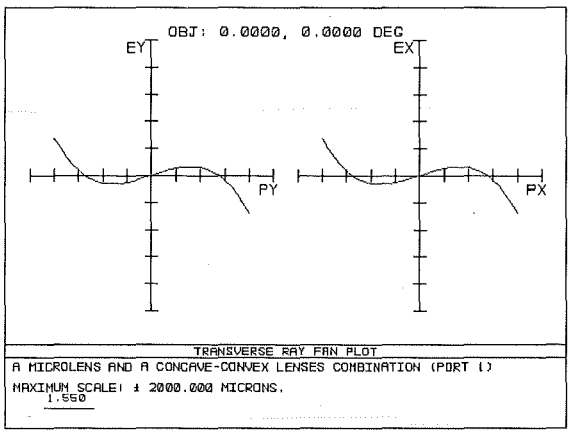

Figure 4.3: The transverse aberrations on image plane of the Concave-convex layout

Eqs. (2.31) to (2.37), (4.5) and (4.6) show that a beam shining on the pixel block has spherical aberration, defocusing and decentering. The types and coefficients of the transverse aberrations are listed in Table 4.3.

Table 4.3: The transverse aberrations coefficients of the Concave-convex layout

Aberration type	Unit: μm
Transverse spherical aberration: $SphT$	$-3.84PY^3$
Coma: $Coma_T$	0
y-axis focus displacement: Δf_T	0
Defocusing displacement: Δf_A	–23.15
Image de-centering displacement: Δh	–8.77

4.1.2 The Concave-Achromatic doublet layout

The OPD (W) of the Concave-Achromatic doublet layout on tangential pupil (PY) and sagittal pupil (PX) are plotted in Figure 4.4, where PY and PX are normalized by the exit pupil (The exit pupil is illustrated in Figure 3.9, Section 3.2.4). The results show that port 1 has the maximum P-V (peak-to-valley) OPD of 0.2059 waves. The actual wavefront is ahead of the reference sphere. Other ports of the maximum P-V OPD are listed in Table 4.4. The table shows that OPD value for each port decreases from center port to outer port on SLM. This layout has results close to the previous layout.

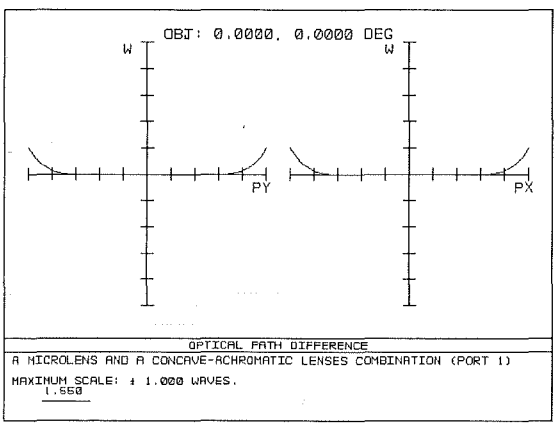

Figure 4.4: OPD of the Concave - Achromatic doublet layout.

Table 4.4: The maximum OPDs of the Concave - Achromatic doublet layout.

Port #	1	2	3	5	6	9
OPD $(unit:\lambda)$	0.2059	0.2057	0.2054	0.2054	0.2051	0.2044

Figure 4.5 shows the wavefront aberrations of the Concave-Achromatic doublet layout at the exit pupil.

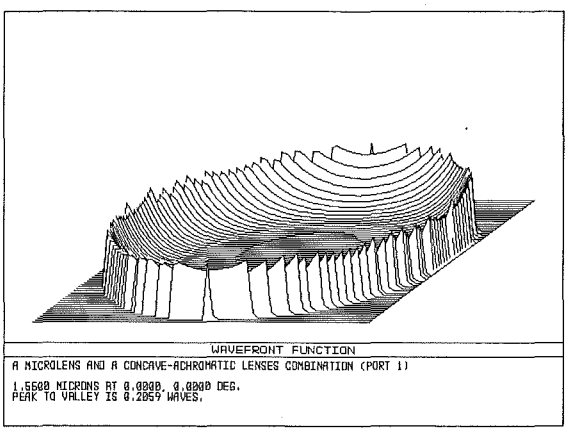

Figure 4.5: The wavefront aberrations of the Concave-Achromatic doublet layout at 1550.nm, for the field angle of 0 deg

In Figure 4.4, $W(0,y)-PY$ and $W(x,0)-PX$ can be expressed as the following polynomials:

$$W(0,y)=W(PY)=0.05095\,PY^4+0.62\,PY^2+0.47\,PY \tag{4.7}$$

$$W(x,0)=W(PX)=0.05095\,PX^4+0.62\,PX^2+0.47\,PX \tag{4.8}$$

Using Eqs. (4.3), (4.4), (4.7) and (4.8), the aberrations of the Concave-Achromatic doublet layout can be obtained as given in Table 4.5.

Table 4.5: Wavefront aberration coefficients for the Concave-Achromatic doublet layout

Spherical aberration coefficient	0.05095
Defocusing coefficient	0.62
De-center and distortion	0.47

The transverse aberrations shown on pixel block can be computed from Eqs. (2.27), (2.28), (4.7) and (4.8). The transverse aberrations for tangential fan $TA_y(0,y)$ and sagittal fan $TA_x(x,0)$ on the pixel block are expressed as

$$TA_y(0,y)=EY=-5.21PY^3-31.74PY-12.04 \tag{4.9}$$

$$TA_x(x,0)=EX=-5.21PX^3-31.74PX-12.04 \tag{4.10}$$

From Eqs. (4.9) and (4.10), the transverse aberrations on y- and x-axes of the pixel block are shown in Figure 4.6.

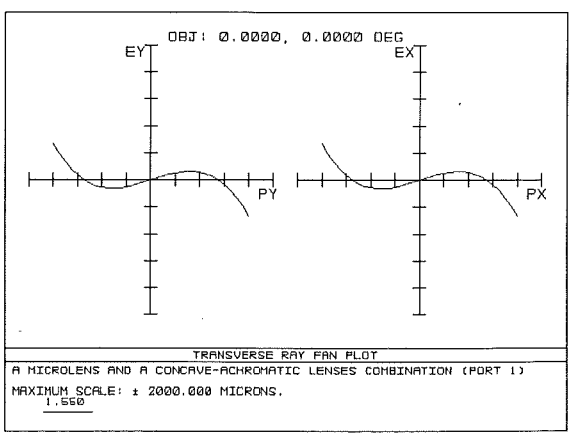

Figure 4.6: The transverse aberrations of the Concave-Achromatic doublet layout

Using Eqs. (2.27), (2.28), (4.9) and (4.10) we find that this layout contains spherical aberration, defocusing and de-centering. We conclude this layout of transverse aberrations and their coefficients in Table 4.6.

Table 4.6: The transverse aberrations coefficients of the Concave - Achromatic doublet layout

Aberration type	Unit: μm
$SphT$	$-5.21PY^3$
$Coma_T$	0
Δf_T	0
Δf_A	−31.74
Δh	−12.04

4.1.3 The Convex-convex lenses layout

The OPD (W) of the Convex-convex layout on tangential pupil (PY) and sagittal pupil (PX) are plotted in Figure 4.7, where PY and PX are normalized by the exit pupil (the exit pupil is illustrated in Figure 3.9, Section 3.2.4). The result shows that the port 1 has the maximum P-V (peak-to-valley) OPD of 0.1661 waves. The figure also shows that the actual wavefront is behind the reference sphere. Other ports of the maximum P-V OPD are listed in Table 4.7. The table shows that OPD value for each port increases from center port to outer ports on the SLM. This result is opposite to what we have seen for the previous two layouts.

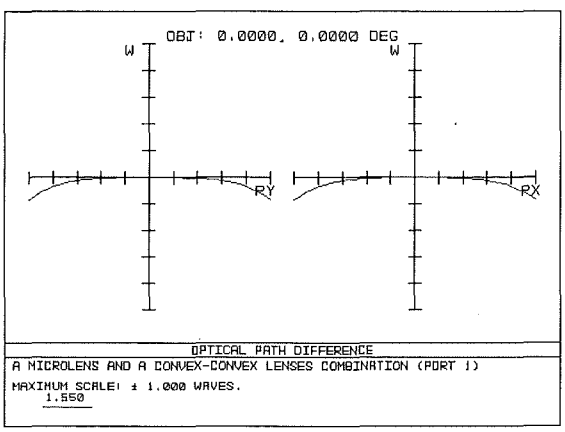

Figure 4.7: OPD of the Convex-convex layout.

Table 4.7: The maximum OPDs of the Convex - convex layout.

Port #	1	2	3	5	6	9
P-V OPD $(unit:\lambda)$	0.1661	0.1668	0.1679	0.167	0.1681	0.1683

Figure 4.8 shows the wavefront aberrations of the Convex-convex layout at the exit pupil.

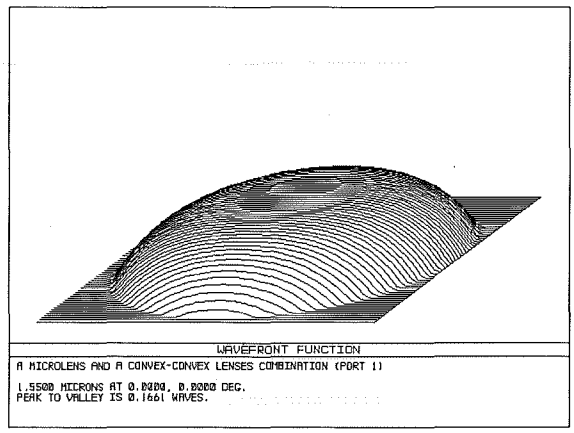

Figure 4.8:The wavefront aberrations of the Convex-convex layout at 1550 nm, for the field angle of 0 deg

As before, $W(0,y)-PY$ and $W(x,0)-PX$ can be expressed as two polynomials:

$$W(0,y)=W(PY)=-0.05097PY^4-0.27PY^2-0.16PY \tag{4.11}$$

$$W(x,o)=W(PX)=-0.05097PX^4-0.27PX^2-0.16PX \tag{4.12}$$

Every type of wavefront aberration and its coefficient can be computed by Eqs. (4.3), (4.4), (4.11) and (4.12). They are listed in Table 4.8. These aberration types are same as the previous two layouts.

Table 4.8 The wavefront aberration coefficients of the Convex-convex layout

Spherical aberration coefficient	- 0.05097
Defocusing coefficient	- 0.27
De-center coefficient	- 0.16

The transverse aberrations polynomial shown on the pixel blocks can be calculated by Eqs. (2.27), (2.28), (4.11) and (4.12). The aberrations for tangential and sagittal fan rays on the pixel block are given as

$$TA_y(0,y)=EY=4.594PY^3+12.35PY+3.59 \tag{4.13}$$

$$TA_x(x,0) = EX = 4.594PX^3 + 12.35PX + 3.59 \quad (4.14)$$

The transverse aberrations shown on the 1st SLM are shown in Figure 4.9. The types and the coefficients of transverse aberrations are listed in Table 4.9.

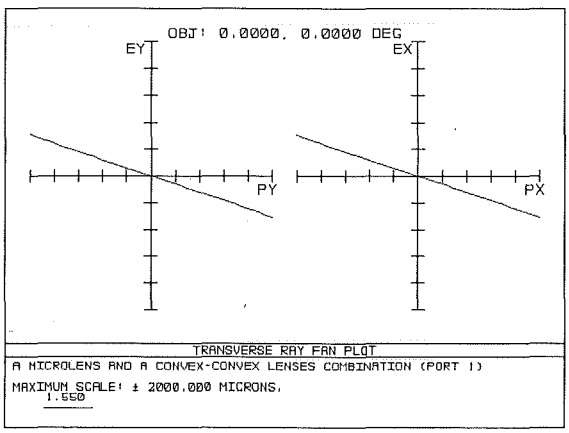

Figure 4.9: The transverse aberrations of the Convex - convex layout

Table 4.9: The transverse aberrations coefficients for the Convex-convex layout

Aberration type	Unit: μm
$SphT$	$4.594PY^3$
$Coma_T$	0
Δf_T	0
Δf_A	12.35
Δh	3.59

4.1.4 The Convex-Achromatic doublet layout

The OPD (W) of the Concave-Achromatic doublet layout on tangential pupil (PY) and sagittal pupil (PX) are plotted in Figure 4.10, where PY and PX are normalized by the exit pupil (the exit pupil is illustrated in Figure 3.9, Section 3.2.4). The results show that port 1 has the maximum P-V (peak-to-valley) OPD of 0.1663 waves. The actual wavefront is behind the reference sphere. Other ports of the maximum P-V OPD are listed in Table 4.10. The table shows that OPD value for each port increases from center port to outer ports on the SLM. This result is same as the third layout.

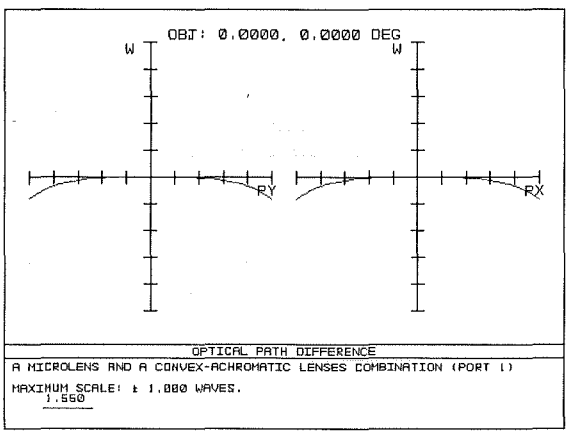

Figure 4.10: OPD for the Convex-Achromatic doublet layout.

Table 4.10: The maximum OPDs for the Convex-Achromatic doublet layout.

Port #	1	2	3	5	6	9
OPD ($unit:\lambda$)	0.1663	0.1684	0.1082	0.1689	0.113	0.1743

Figure 4.11 shows the wavefront aberrations of the Convex-Achromatic doublet layout at the exit pupil.

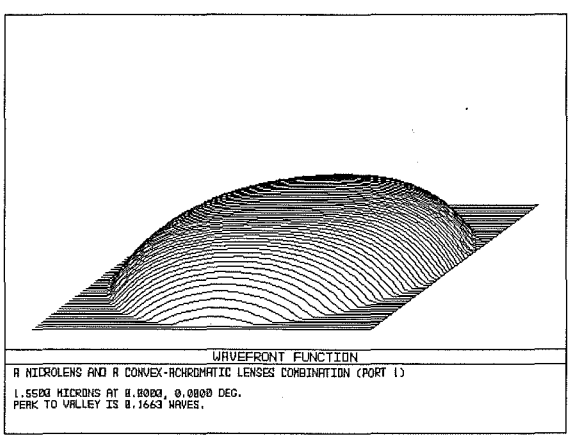

Figure.4.11: Wavefront aberrations for the Convex-Achromatic doublet layout at 1550 nm, for the field angle of 0 deg

The $W(0,y)-PY$ and $W(x,0)-PX$ can be expressed as two polynomials:

$$W(0,y)=W(PY)=-0.05096PY^4-0.45PY^2-0.24PY \tag{4.15}$$

$$W(x,0)=W(PX)=-0.05096PX^4-0.45PX^2-0.24PX \tag{4.16}$$

Table 4.11 presents the types and the coefficients of the wavefront aberrations showing at the exit pupil. Spherical aberration, defocusing, and de-centering are generated by this layout.

Table 4.11: The wavefront aberration coefficients of the Convex - Achromatic doublet layout

Spherical aberration coefficient	- 0.05096
Defocusing coefficient	- 0.45
De-center coefficient	- 0.24

From Eqs. (2.27), (2.28), (4.15) and (4.16), we can calculate the transverse aberration polynomials shown on the image plane as

$$TA_y(0,y)=EY=4.55PY^3+20.17PY+5.41 \tag{4.17}$$

$$TA_x(x,0)=EX=4.55PX^3+20.17PX+5.41 \tag{4.18}$$

By Eqs. (2.27), (2.28), (4.17) and (4.18), we find that this layout generates spherical aberration, defocusing and decentering on the pixel block. These aberrations types are the same as the previous three layouts. Eqs. (4.17) and (4.18) of the transverse aberrations shown on the 1st SLM are plotted in Figure 4.12. The types of transverse aberrations and the coefficients of this layout are listed in Table 4.12.

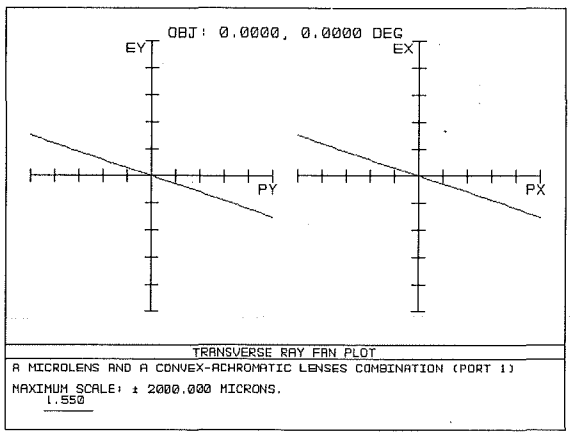

Figure 4.12: The transverse aberrations on the image plane of the Convex - Achromatic doublet layout

Table 4.12: The transverse aberrations coefficients of the Convex - Achromatic doublet layout

Aberration type	Unit: μm
$SphT$	$4.55PY^3$
$Coma_T$	0
Δf_T	0
Δf_A	20.17
Δh	5.41

4.2 Discussion

In this chapter, we have explored the aberration effects for each of the 4 optical system layouts as designed in Chapter 3. In this section, we will compare the aberration effects for these four layouts. System aberrations are compared from three perspectives: OPD, wavefront aberrations and transverse aberrations. In addition, with considering the beam performance analyses which were described in Chapter 3, we will then choose a right layout for the optical system.

The first aberration comparison is from the perspective of OPD. Each layout's OPD is presented in Table 4.13 (data are collected from Tables 4.1, Table 4.4, Table 4.7 and Table 4.10). The table shows that the third layout has the smallest OPD. In fact, all ports of the Convex-convex layout present the least OPD compared to the corresponding ports of the other layouts. The first two layouts have the similar OPD results which are higher than the third and fourth layouts.

Table 4.13: Comparison the OPDs of the four layouts.

Layout	The maximum OPD (unit: λ)
Concave-convex	0.2055
Concave-Achromatic doublet	0.2059
Convex-convex	0.1683
Convex-Achromatic doublet	0.1743

The second aberration comparison is from the perspective of wavefront error at each system's exit pupil. Wavefront error is expressed by a polynomial, so that the specific types of aberrations can be found and its coefficients can be calculated. We summarize the four layouts' wavefront aberrations in Table 4.14 (data are collected from Tables 4.2, Table 4.5, Table 4.8 and Table 4.11). This table shows that spherical aberrations for the four layouts have similar coefficients (in absolute value). However, the negative sign means that the actual wavefront is behind the reference sphere. So, in the first two layouts, the actual wavefront is ahead of the reference sphere. On the other hand, in the last two layouts, the actual wavefront is behind the reference sphere. The table shows that the Convex-convex layout has the best performance at defocusing and de-center/distortion at the system's exit pupil.

Table 4.14: Comparison the wavefront aberrations of the four layouts.

Layout	Spherical aberration	Defocusing	De-center/distortion
Concave-convex	0.05095	0.61	0.47
Concave-Achromatic doublet	0.05095	0.62	0.47
Convex-convex	-0.05097	-0.27	-0.16
Convex-Achromatic doublet	-0.05096	-0.45	-0.24

The final aberration comparison is from the perspective of transverse aberration. All the data of transverse aberrations from the four layouts are listed in Table 4.15 (data are collected from Tables 4.3, Table 4.6, Table 4.9 and Table 4.12). This table gives more accurate data for comparing the aberration effects which are produced on the SLM. Especially, the spherical aberration effect for each layout is clearly distinguished. The concave–convex layout has the best result. Thus, the Convex–convex layout has the least aberration produced on the SLM.

Table 4.15: Comparison the transverse aberrations of the four layouts.

Layout	$SphT$	Δf_A	Δh
Concave-convex	$-3.84PY^3$	−23.15	−8.77
Concave-Achromatic doublet	$-5.21PY^3$	−31.74	−12.04
Convex-convex	$4.594PY^3$	12.35	3.59
Convex-Achromatic doublet	$4.55PY^3$	20.17	5.41

In summary, considering the beam quality performance (as explored in Chapter 3), and the aberration analysis presented in this chapter, the Convex-convex layout has the best image forming on the SLM. Therefore, we select the Convex–convex layout for our optical system. However, this layout still needs to be optimized, so that it can satisfy all requirements of our optical system. This issue will be addressed in the next chapter.

Chapter 4

Analysis the Aberration Effects on the 1st SLM

In Chapter 3, we designed four optical system layouts and investigated the beams performance. In this chapter, we will analyze the aberration effects shown on the pixel blocks by utilizing Zemax software program [69]. The aberrations will be presented by three perspectives: system optical path difference (OPD), wavefront error, and transverse aberration. OPD is the difference of the wavefront from the reference sphere. OPD is expressed by a number and the unit is the beam wavelength (λ). Less OPD indicates less aberration. Wavefront error and transverse aberration can be detected by observing the pattern of the aberration itself and may also be computed in a polynomial form. Therefore, we can understand the types of aberrations and their coefficients for each layout. Finally, the comparison of aberrations for these four layouts will be discussed.

The results show that every port in each layout has the same types of aberrations, and a close aberration coefficients as well. Thus, we present the aberration data in port 1 as the layout's aberration effect. Also, the simulation data show that four layouts produce the same types of aberrations on the 1st SLM. They are: spherical aberration, defocusing, and de-centering. However, Coma and Astigmatism are not shown. In addition, the Convex-convex lenses layout performs the least aberration on the 1st SLM.

4.1 Analysis of aberration with Four Layouts

4.1.1 The Concave-convex lenses layout

To simplify aberrations analysis, we consider tangential (PY, y-axis) fan and sagittal (PX, x-axis) fan of the port 1 rays tracing through the optical system. The OPD (W) of the Concave-convex layout on tangential pupil (PY) and sagittal pupil (PX) are plotted in Figure 4.1. Where PY and PX are normalized by the exit pupil (The exit pupil is illustrated in Figure 3.9, Section 3.2.4). The result shows that the port 1 has the maximum P-V (peak-to-valley) OPD of 0.2055 waves. Due to the positive value of OPD, the actual

wavefront is ahead of the reference sphere. Other ports of the maximum P-V OPD are listed in Table 4.1. The table shows that OPD value for each port decreases from center port to outer port on SLM.

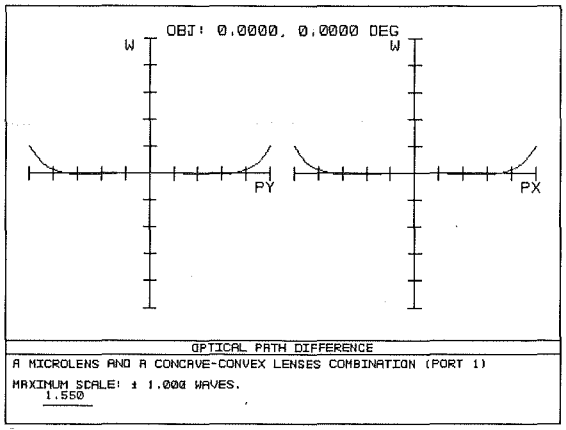

Figure 4.1: OPD of the Concave-convex layout.

Table 4.1:The maximum OPDs of the Concave-convex layout.

Port #	1	2	3	5	6	9
OPD $(unit:\lambda)$	0.2055	0.2042	0.2016	0.2020	0.2001	0.1932

Figure 4.2 shows the wavefront aberrations of the Concave-convex layout at the exit pupil.

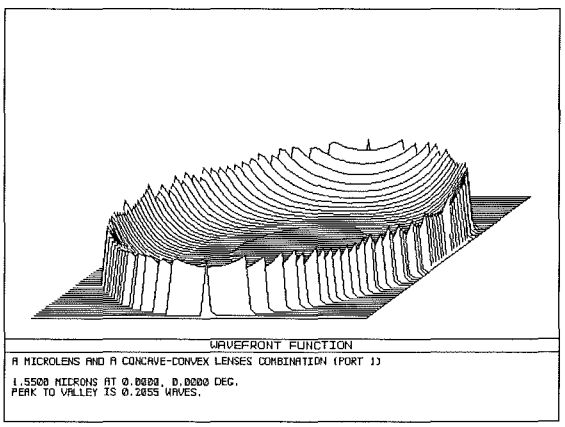

Figure 4.2: The wavefront aberrations for the Concave-convex layout at 1550 nm, for the field angle of 0 deg

In Figure 4.1, $W(0,y)-PY$ and $W(x,0)-PX$ can be expressed as two polynomials:

$$W(0,y)=W(PY)=0.05095\,PY^4+0.61\,PY^2+0.47\,PY \tag{4.1}$$

$$W(x,0)=W(PX)=0.05095\,PX^4+0.61\,PX^2+0.47\,PX \tag{4.2}$$

From Eq. (2.22), $W(0,y)$ and $W(x,0)$ can be expressed as

$$W(0,y) = A y^4 + B y^3 + (3C + D) y^2 + E y + F \tag{4.3}$$

$$W(x,0) = A x^4 + (C + D) x^2 + F \tag{4.4}$$

Therefore, using Eqs. (4.1) to (4.4), we can find each type of aberration and its coefficient presents at the exit pupil. They are shown in Table 4.2.

Table 4.2 The wavefront Aberration coefficients of the Concave-convex layout

A: Spherical aberration coefficient	0.05095
B: Coma coefficient	0
C: Astigmatism coefficient	0
D: Defocusing coefficient	0.61
E: De-centering coefficient	0.47
F: Constant or piston term	0

This table presents that the Concave-convex layout generates spherical aberration (A), defocusing (D), and de-centering (E). Spherical aberration coefficient A is positive because the actual wavefront is ahead of reference sphere. However, Coma and Astigmatism are not present in this layout, because both coefficients B and C are zero. Defocusing is the distance of the pixel block from a Gaussian beam waist. The positive value presents that the beam waist is located in front of the SLM, while the negative value means that beam waist has not formed before it hits the SLM. One reason for defocusing is due to the title angle (7^0) of the SLM itself. De-centering is the deviation of a Gaussian beam from the center of the pixel block.

The transverse aberrations shown on each pixel block can be computed from Eqs. (4.1) and (4.2). Using Eqs. (2.27), (2.28), (4.1) and (4.2), the transverse aberrations for tangential fan $TA_y(0,y)$ and sagittal fan $TA_x(x,0)$ on the pixel block are given as

$$TA_y(0,y) = EY = -3.84PY^3 - 23.15PY - 8.77 \tag{4.5}$$

$$TA_x(x,0) = EX = -3.84PX^3 - 23.15PX - 8.77 \tag{4.6}$$

where EY and EX represent the transverse aberration on y and x axes respectively. The unit of TA is μm. The transverse aberrations on y- and x-axes of the pixel block are shown in Figure 4.3.

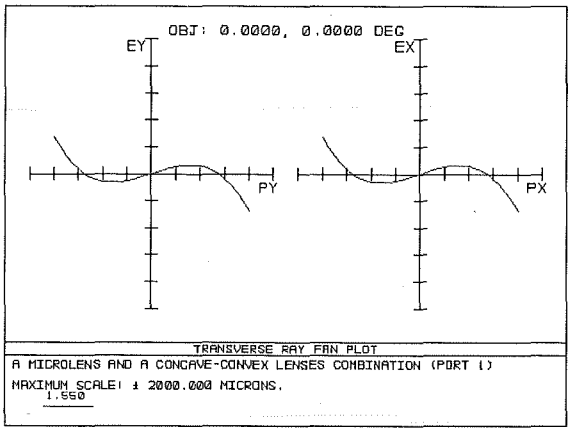

Figure 4.3: The transverse aberrations on image plane of the Concave-convex layout

Eqs. (2.31) to (2.37), (4.5) and (4.6) show that a beam shining on the pixel block has spherical aberration, defocusing and decentering. The types and coefficients of the transverse aberrations are listed in Table 4.3.

Table 4.3: The transverse aberrations coefficients of the Concave-convex layout

Aberration type	Unit: μm
Transverse spherical aberration: $SphT$	$-3.84PY^3$
Coma: $Coma_T$	0
y-axis focus displacement: Δf_T	0
Defocusing displacement: Δf_A	−23.15
Image de-centering displacement: Δh	−8.77

4.1.2 The Concave-Achromatic doublet layout

The OPD (W) of the Concave-Achromatic doublet layout on tangential pupil (PY) and sagittal pupil (PX) are plotted in Figure 4.4, where PY and PX are normalized by the exit pupil (The exit pupil is illustrated in Figure 3.9, Section 3.2.4). The results show that port 1 has the maximum P-V (peak-to-valley) OPD of 0.2059 waves. The actual wavefront is ahead of the reference sphere. Other ports of the maximum P-V OPD are listed in Table 4.4. The table shows that OPD value for each port decreases from center port to outer port on SLM. This layout has results close to the previous layout.

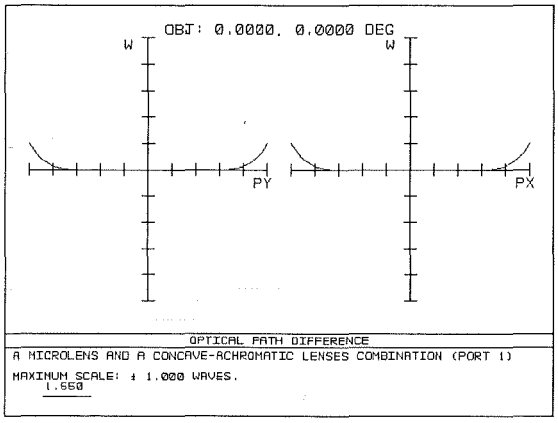

Figure 4.4: OPD of the Concave - Achromatic doublet layout.

Table 4.4: The maximum OPDs of the Concave - Achromatic doublet layout.

Port #	1	2	3	5	6	9
OPD $(unit:\lambda)$	0.2059	0.2057	0.2054	0.2054	0.2051	0.2044

Figure 4.5 shows the wavefront aberrations of the Concave-Achromatic doublet layout at the exit pupil.

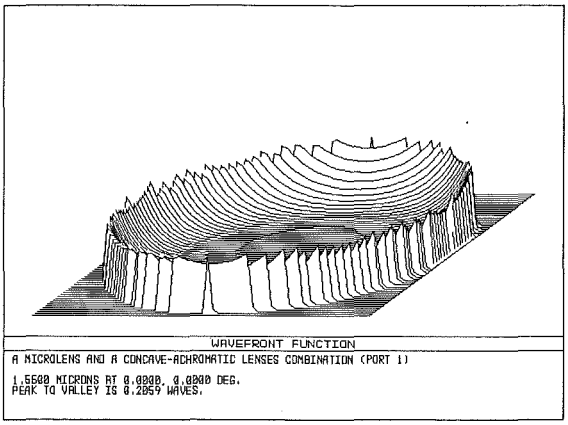

Figure 4.5: The wavefront aberrations of the Concave-Achromatic doublet layout at 1550.nm, for the field angle of 0 deg

In Figure 4.4, $W(0,y)-PY$ and $W(x,0)-PX$ can be expressed as the following polynomials:

$$W(0,y)=W(PY)=0.05095\,PY^4+0.62\,PY^2+0.47\,PY \tag{4.7}$$

$$W(x,0)=W(PX)=0.05095\,PX^4+0.62\,PX^2+0.47\,PX \tag{4.8}$$

Using Eqs. (4.3), (4.4), (4.7) and (4.8), the aberrations of the Concave-Achromatic doublet layout can be obtained as given in Table 4.5.

Table 4.5: Wavefront aberration coefficients for the Concave-Achromatic doublet layout

Spherical aberration coefficient	0.05095
Defocusing coefficient	0.62
De-center and distortion	0.47

The transverse aberrations shown on pixel block can be computed from Eqs. (2.27), (2.28), (4.7) and (4.8). The transverse aberrations for tangential fan $TA_y(0,y)$ and sagittal fan $TA_x(x,0)$ on the pixel block are expressed as

$$TA_y(0,y)=EY=-5.21PY^3-31.74PY-12.04 \tag{4.9}$$

$$TA_x(x,0)=EX=-5.21PX^3-31.74PX-12.04 \tag{4.10}$$

From Eqs. (4.9) and (4.10), the transverse aberrations on y- and x-axes of the pixel block are shown in Figure 4.6.

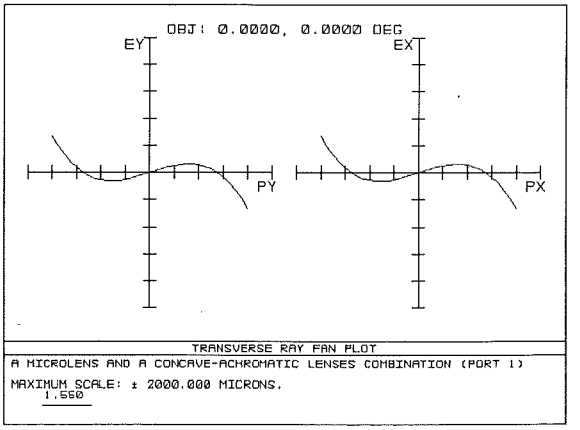

Figure 4.6: The transverse aberrations of the Concave-Achromatic doublet layout

Using Eqs. (2.27), (2.28), (4.9) and (4.10) we find that this layout contains spherical aberration, defocusing and de-centering. We conclude this layout of transverse aberrations and their coefficients in Table 4.6.

Table 4.6: The transverse aberrations coefficients of the Concave - Achromatic doublet layout

Aberration type	Unit: μm
$SphT$	$-5.21PY^3$
$Coma_T$	0
Δf_T	0
Δf_A	−31.74
Δh	−12.04

4.1.3 The Convex-convex lenses layout

The OPD (W) of the Convex-convex layout on tangential pupil (PY) and sagittal pupil (PX) are plotted in Figure 4.7, where PY and PX are normalized by the exit pupil (the exit pupil is illustrated in Figure 3.9, Section 3.2.4). The result shows that the port 1 has the maximum P-V (peak-to-valley) OPD of 0.1661 waves. The figure also shows that the actual wavefront is behind the reference sphere. Other ports of the maximum P-V OPD are listed in Table 4.7. The table shows that OPD value for each port increases from center port to outer ports on the SLM. This result is opposite to what we have seen for the previous two layouts.

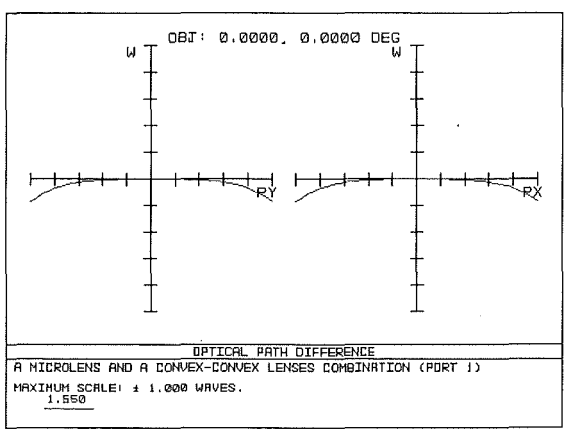

Figure 4.7: OPD of the Convex-convex layout.

Table 4.7: The maximum OPDs of the Convex - convex layout.

Port #	1	2	3	5	6	9
P-V OPD $(unit:\lambda)$	0.1661	0.1668	0.1679	0.167	0.1681	0.1683

Figure 4.8 shows the wavefront aberrations of the Convex-convex layout at the exit pupil.

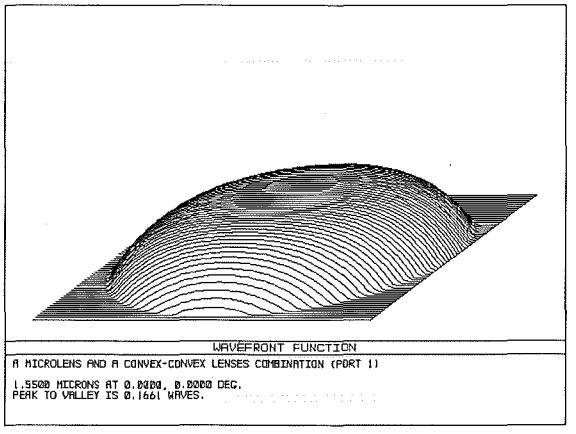

Figure 4.8:The wavefront aberrations of the Convex-convex layout at 1550 nm, for the field angle of 0 deg

As before, $W(0,y)-PY$ and $W(x,0)-PX$ can be expressed as two polynomials:

$$W(0,y)=W(PY)=-0.05097PY^4-0.27PY^2-0.16PY \tag{4.11}$$

$$W(x,o)=W(PX)=-0.05097PX^4-0.27PX^2-0.16PX \tag{4.12}$$

Every type of wavefront aberration and its coefficient can be computed by Eqs. (4.3), (4.4), (4.11) and (4.12). They are listed in Table 4.8. These aberration types are same as the previous two layouts.

Table 4.8 The wavefront aberration coefficients of the Convex-convex layout

Spherical aberration coefficient	- 0.05097
Defocusing coefficient	- 0.27
De-center coefficient	- 0.16

The transverse aberrations polynomial shown on the pixel blocks can be calculated by Eqs. (2.27), (2.28), (4.11) and (4.12). The aberrations for tangential and sagittal fan rays on the pixel block are given as

$$TA_y(0,y)=EY=4.594PY^3+12.35PY+3.59 \tag{4.13}$$

$$TA_x(x,0) = EX = 4.594PX^3 + 12.35PX + 3.59 \quad (4.14)$$

The transverse aberrations shown on the 1st SLM are shown in Figure 4.9. The types and the coefficients of transverse aberrations are listed in Table 4.9.

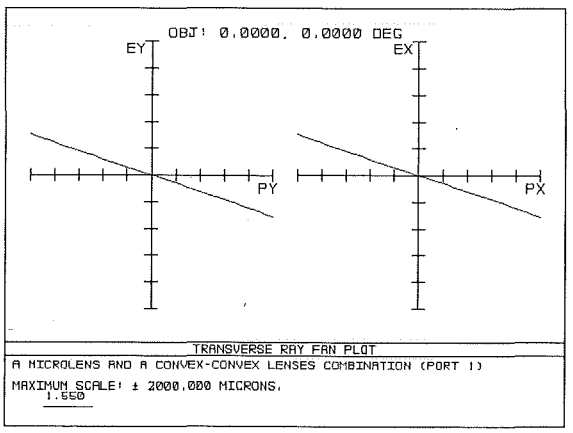

Figure 4.9: The transverse aberrations of the Convex - convex layout

Table 4.9: The transverse aberrations coefficients for the Convex-convex layout

Aberration type	Unit: μm
$SphT$	$4.594PY^3$
$Coma_T$	0
Δf_T	0
Δf_A	12.35
Δh	3.59

4.1.4 The Convex-Achromatic doublet layout

The OPD (W) of the Concave-Achromatic doublet layout on tangential pupil (PY) and sagittal pupil (PX) are plotted in Figure 4.10, where PY and PX are normalized by the exit pupil (the exit pupil is illustrated in Figure 3.9, Section 3.2.4). The results show that port 1 has the maximum P-V (peak-to-valley) OPD of 0.1663 waves. The actual wavefront is behind the reference sphere. Other ports of the maximum P-V OPD are listed in Table 4.10. The table shows that OPD value for each port increases from center port to outer ports on the SLM. This result is same as the third layout.

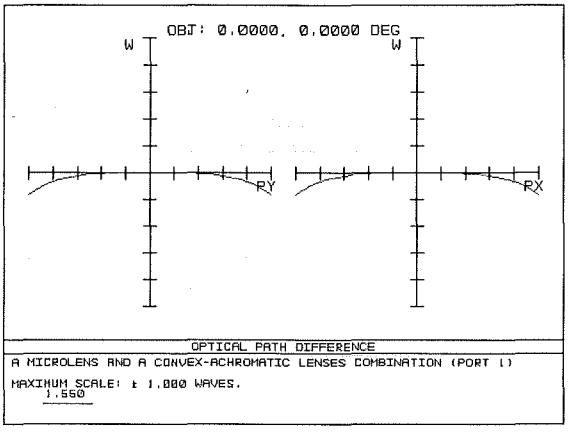

Figure 4.10: OPD for the Convex-Achromatic doublet layout.

Table 4.10: The maximum OPDs for the Convex-Achromatic doublet layout.

Port #	1	2	3	5	6	9
OPD ($unit:\lambda$)	0.1663	0.1684	0.1082	0.1689	0.113	0.1743

Figure 4.11 shows the wavefront aberrations of the Convex-Achromatic doublet layout at the exit pupil.

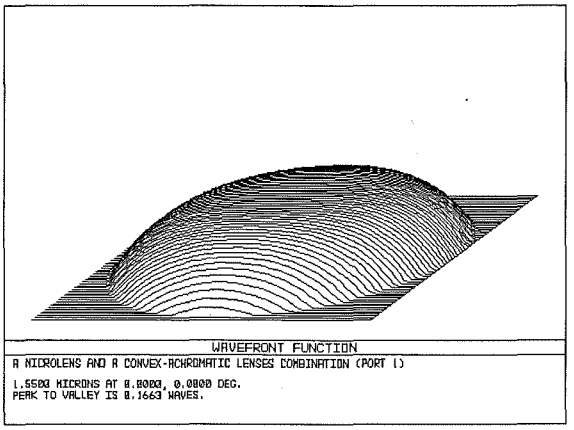

Figure.4.11: Wavefront aberrations for the Convex-Achromatic doublet layout at 1550 nm, for the field angle of 0 deg

The $W(0,y)-PY$ and $W(x,0)-PX$ can be expressed as two polynomials:

$$W(0,y)=W(PY)=-0.05096PY^4-0.45PY^2-0.24PY \quad (4.15)$$

$$W(x,0)=W(PX)=-0.05096PX^4-0.45PX^2-0.24PX \quad (4.16)$$

Table 4.11 presents the types and the coefficients of the wavefront aberrations showing at the exit pupil. Spherical aberration, defocusing, and de-centering are generated by this layout.

Table 4.11: The wavefront aberration coefficients of the Convex - Achromatic doublet layout

Spherical aberration coefficient	- 0.05096
Defocusing coefficient	- 0.45
De-center coefficient	- 0.24

From Eqs. (2.27), (2.28), (4.15) and (4.16), we can calculate the transverse aberration polynomials shown on the image plane as

$$TA_y(0,y)=EY=4.55PY^3+20.17PY+5.41 \quad (4.17)$$

$$TA_x(x,0)=EX=4.55PX^3+20.17PX+5.41 \quad (4.18)$$

By Eqs. (2.27), (2.28), (4.17) and (4.18), we find that this layout generates spherical aberration, defocusing and decentering on the pixel block. These aberrations types are the same as the previous three layouts. Eqs. (4.17) and (4.18) of the transverse aberrations shown on the 1st SLM are plotted in Figure 4.12. The types of transverse aberrations and the coefficients of this layout are listed in Table 4.12.

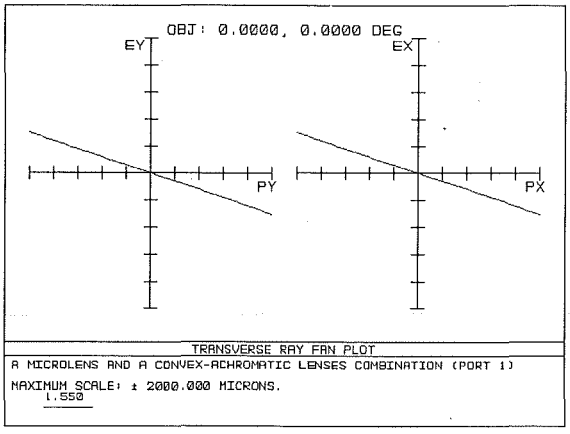

Figure 4.12: The transverse aberrations on the image plane of the Convex - Achromatic doublet layout

Table 4.12: The transverse aberrations coefficients of the Convex - Achromatic doublet layout

Aberration type	Unit: μm
$SphT$	$4.55PY^3$
$Coma_T$	0
Δf_T	0
Δf_A	20.17
Δh	5.41

4.2 Discussion

In this chapter, we have explored the aberration effects for each of the 4 optical system layouts as designed in Chapter 3. In this section, we will compare the aberration effects for these four layouts. System aberrations are compared from three perspectives: OPD, wavefront aberrations and transverse aberrations. In addition, with considering the beam performance analyses which were described in Chapter 3, we will then choose a right layout for the optical system.

The first aberration comparison is from the perspective of OPD. Each layout's OPD is presented in Table 4.13 (data are collected from Tables 4.1, Table 4.4, Table 4.7 and Table 4.10). The table shows that the third layout has the smallest OPD. In fact, all ports of the Convex-convex layout present the least OPD compared to the corresponding ports of the other layouts. The first two layouts have the similar OPD results which are higher than the third and fourth layouts.

Table 4.13: Comparison the OPDs of the four layouts.

Layout	The maximum OPD (unit: λ)
Concave-convex	0.2055
Concave-Achromatic doublet	0.2059
Convex-convex	0.1683
Convex-Achromatic doublet	0.1743

The second aberration comparison is from the perspective of wavefront error at each system's exit pupil. Wavefront error is expressed by a polynomial, so that the specific types of aberrations can be found and its coefficients can be calculated. We summarize the four layouts' wavefront aberrations in Table 4.14 (data are collected from Tables 4.2, Table 4.5, Table 4.8 and Table 4.11). This table shows that spherical aberrations for the four layouts have similar coefficients (in absolute value). However, the negative sign means that the actual wavefront is behind the reference sphere. So, in the first two layouts, the actual wavefront is ahead of the reference sphere. On the other hand, in the last two layouts, the actual wavefront is behind the reference sphere. The table shows that the Convex-convex layout has the best performance at defocusing and de-center/distortion at the system's exit pupil.

Table 4.14: Comparison the wavefront aberrations of the four layouts.

Layout	Spherical aberration	Defocusing	De-center/distortion
Concave-convex	0.05095	0.61	0.47
Concave-Achromatic doublet	0.05095	0.62	0.47
Convex-convex	-0.05097	-0.27	-0.16
Convex-Achromatic doublet	-0.05096	-0.45	-0.24

The final aberration comparison is from the perspective of transverse aberration. All the data of transverse aberrations from the four layouts are listed in Table 4.15 (data are collected from Tables 4.3, Table 4.6, Table 4.9 and Table 4.12). This table gives more accurate data for comparing the aberration effects which are produced on the SLM. Especially, the spherical aberration effect for each layout is clearly distinguished. The concave–convex layout has the best result. Thus, the Convex–convex layout has the least aberration produced on the SLM.

Table 4.15: Comparison the transverse aberrations of the four layouts.

Layout	$SphT$	Δf_A	Δh
Concave-convex	$-3.84PY^3$	−23.15	−8.77
Concave-Achromatic doublet	$-5.21PY^3$	−31.74	−12.04
Convex-convex	$4.594PY^3$	12.35	3.59
Convex-Achromatic doublet	$4.55PY^3$	20.17	5.41

In summary, considering the beam quality performance (as explored in Chapter 3), and the aberration analysis presented in this chapter, the Convex-convex layout has the best image forming on the SLM. Therefore, we select the Convex–convex layout for our optical system. However, this layout still needs to be optimized, so that it can satisfy all requirements of our optical system. This issue will be addressed in the next chapter.

Chapter 5

System Optimization and Diffraction limited Analysis

In previous two chapters, we presented the beam performances and aberration effects for the four design layouts. Following the analysis, the convex-convex layout was chosen for our optical system due to its adequate performance. This layout satisfied the beam collimation, alignment, uniform illumination and low aberrations criteria. However, one issue for this layout is that the beam spot size on the pixel block (0.6127 *mm*, in Section 3.3.3) is larger than we need (0.53 *mm*, in Section 3.1.2). Thus, in this chapter we will optimize the convex-convex layout to address this issue.

However, a related issue is whether the optimized layout satisfies the image with diffraction limited criteria on the 1st SLM. To address this issue, the application of the Modulation Transfer Function (MTF) in the optimized layout is introduced. MTF is extremely useful because the diffraction limited MTF is the upper limit for any system performance. No optical system can perform better than its diffraction limited MTF [63,68,69]. Aberrations will increase image size, thus contribute to a poor MTF. This is because aberrations will pull the MTF curve down. Therefore, MTF can compare the curve for an imperfect system (with aberration) with the curve for a perfect system (diffraction limited). Moreover, comparing MTF curves can decide how much headroom has been left for manufacturing tolerances.

The results show that the optimized layout has the averaged beam size of 0.5276 *mm* on the pixel block. In addition, the optimized layout has satisfied the beam collimation, alignment, and uniform illumination criteria. Moreover, this layout has improved 20% of the aberration effects, if we compare to the Convex-convex layout. The total dimension is 332.2 *mm*. Finally, the MTF confirms that the optimized layout has achieved the diffraction limited on the first SLM.

5.1 Optimizing the Convex-convex Lenses Layout

In order to optimize the Convex-convex layout, the first modification is to move the stop position in the optical system. This is because for the third component we using is a 150 *mm* of market catalog lens, not the 155 *mm* lens that we computed in Section 3.2.4. Therefore, increasing some space between two optical elements can compensate this little component power difference. Also, the advantage of this method is that we still keep lens shape for each component to reduce aberrations whilst using off-the-shelf lenses to reduce the cost.

Table 4.9 shows that the Convex-convex layout has a defocusing distance of $12.35\,\mu m$. Therefore, by Eq. (2.15) and increasing the distance between the 450 μm microlens array and 12.5 *mm* plano-convex lens from 12.95 *mm* to 14.03 *mm*, the beam has the average size of 0.5276 *mm* illuminated on the pixel block. The renewed lens prescription is listed below:

Lens prescription:

Radius	thickness	glass	index	semi-aperture
Infinity	0.45	air		0.000011
0.2253	0.024	BK7	1.50065204	0.08
Infinity	14.03	air		0.050947
6.563	3.819	BK7	1.50065204	3.175
Infinity	159.83	air		3.175
Infinity	4.047	BK7	1.50065204	12.7
-77.52	150	air		12.7

Effective Focal Length = -5.27 *mm*
Back Focal Length = 87.43 *mm*
Total Track = 332.2 *mm*
Working F/# = 1005.7

Figure 5.1 shows Gaussian beam illuminating on port 1 pixel block. The beam radius is 0.5312 *mm.* Other beam illuminations on the 1st SLM are listed in Table 5.1. The table shows that the beam has less de-centering compared to the previous four layouts. In addition, the beam sizes on the SLM are decreasing form the port 1 to 9. The average beam size is 0.5276 *mm* and the standard deviation for these ports is 0.0026 *mm* or 0.49% as listed in Table 5.2. The results show that the optimized layout has better quality beam illumination on the 1st SLM than the previous four layouts. Also, the divergent angle is the smallest.

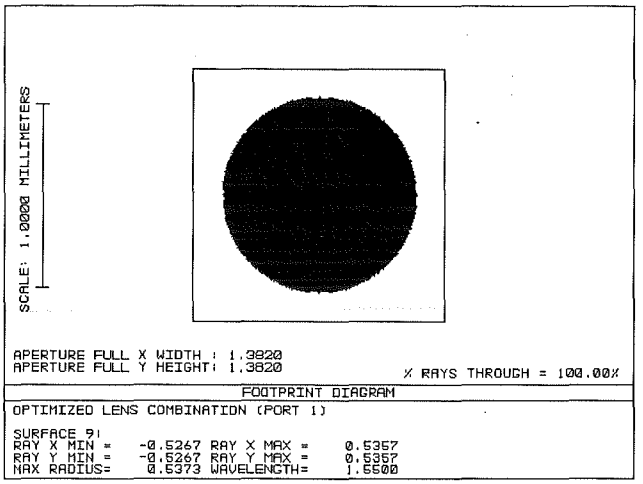

Figure 5.1: Beam illuminating at the pixel block of the optimized layout

Table 5.1: Beams illuminating at the pixel blocks of the optimized layout

Port #	1	2	3	5	6	9
On x axis*	-0.5267	-0.5187	-0.5072	-0.5181	-0.5066	-0.505
On y axis*	0.5357	0.5397 -0.5259	0.5431 -0.5243	0.5391	0.5425 -0.5163	0.5414
		0.535	0.5336		0.5379	
Average radius	0.5312	0.5298	0.527	0.5286	0.5258	0.5232

Table 5.2: Average beam size and its S.D. of the optimized layout

Averaged radius	Standard deviation	
0.5276 *mm*	0.0026 *mm*	0.49%

The modified beam size satisfies the required value. The other results show that this modification neither affects the system collimation, alignment, and beam uniform illumination, nor the low aberrations on the 1st SLM. Moreover, the size of the beam illuminating the pixel block will cause the clipping ratio of $\gamma = 2.62$. This value is greater than 2.6 and thus the system will prevent a larger 0.2 dB coupling power penalty, which is mentioned in Section 3.1.2. The total dimension of the optimized layout is 332.2 *mm*. This dimension is acceptable as a compact size, as we required.

Next, we observe the aberration effect for the optimized layout. The OPD (W) of the optimized layout on tangential pupil (PY) and sagittal pupil (PX) are plotted in Figure 5.2 (The exit pupil is illustrated in Figure 3.9, Section 3.2.4). The port 1 has the maximum P-V (peak-to-valley) OPD of 0.1511 waves. The actual wavefront is behind the reference sphere. Other ports of the maximum P-V OPD are listed in Table 5.3. The averaged OPD for the optimized layout is 0.1515 waves. In addition, the optimized layout has decreased by 10%of OPD, if compared to the Convex-convex layout (as shown in Table 4.13).

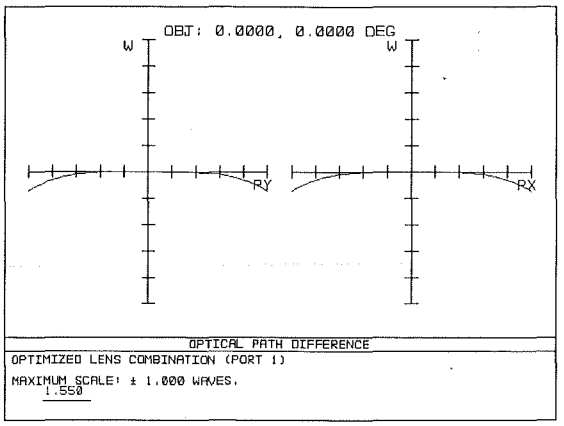

Figure 5.2: OPD at the exit pupil of the optimized layout

Table 5.3: The maximum OPDs for the specific ports of the optimized layout

Port #	1	2	3	5	6	9
OPD $(unit:\lambda)$	0.1511	0.1511	0.1517	0.1512	0.1518	0.1519

Figure 5.3 shows the wavefront aberration presents at the exit pupil.

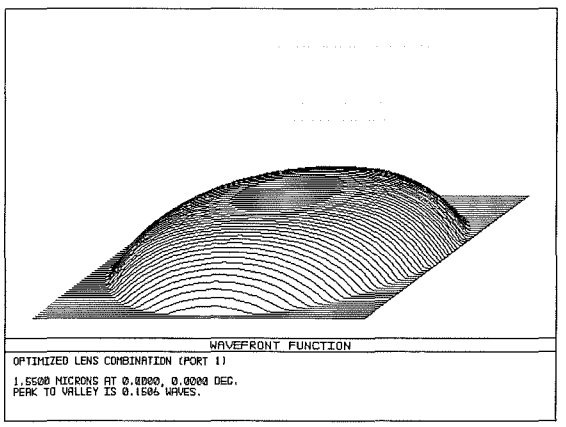

Figure 5.3: The wavefront aberrations of the optimized layout at 1550 nm, for the field angle of 0 deg

$W(0,y)-PY$ and $W(x,0)-PX$ can be expressed as the polynomial

$$W(PY) = -0.05\,PY^4 - 0.23\,PY^2 - 0.128\,PY \tag{5.1}$$

$$W(PX) = -0.05\,PX^4 - 0.23\,PX^2 - 0.128\,PX \tag{5.2}$$

Eqs. (5.1) and (5.2) show that the optimized layout has the same types of aberrations to the previous layouts. The aberration types and their coefficients are listed in Table 5.4. The negative value of the coefficients means that actual wavefront is behind the

reference sphere at the exit pupil. In addition, these values of coefficients are less than any other previous layouts (They were presented in Table 4.14).

Table 5.4: The wavefront aberration coefficients of the optimized layout

Spherical aberration coefficient	-0.05
Defocusing coefficient	-0.23
De-centering coefficient	-0.128

The transverse aberrations appearing on the pixel block can be computed by Eqs. (2.27), (2.28), (5.1), and (5.2). The transverse aberrations for tangential fan $TA_y(0,y)$ and sagittal fan $TA_x(x,0)$ on the pixel block are given as

$$TA_y(0,y) = EY = 3.55PY^3 + 10.16PY + 2.85 \tag{5.3}$$

$$TA_x(x,0) = EX = 3.55PX^3 + 10.16PX + 2.85 \tag{5.4}$$

The types and coefficients of transverse aberrations are listed in Table 5.5. The optimized layout has spherical, defocusing and de-centering aberrations on the 1st SLM. However, the aberration coefficients of the optimized layout are reduced, if we compare them to the previous layouts (they are presented in Table 4.15). In general, they have an average reduction of 20% ($SphT$ is 22.7% off, Δf_A is 17.7% off, and Δh is 20.6% off).

Table 5.5: The transverse aberrations coefficients of the optimized layout

Aberration type	Unit: μm
Transverse spherical aberration: $SphT$	$3.55PY^3$
Coma: $Coma_T$	0
y-axis focus displacement: Δf_T	0
Defocusing displacement: Δf_A	10.16
Image de-centering displacement: Δh	2.85

5.2 Diffraction limited analysis

Due to the wave nature of light, any optical system with a finite size aperture can never form a point image. There is a characteristic minimum blur diameter, even when other image aberrations are absent. Therefore, the best performance that an optical system is capable of is called its "diffraction limited" performance.

To analyze the optimized layout satisfying the diffraction limited criteria on the SLM, we introduce the transfer function. The transfer function can be defined as the ratio of the spatial frequency spectrum of the output optical field to the spatial frequency spectrum of the input optical field. When the system is, for example, the lens of the eye and the input is electromagnetic radiation, then the transfer function characterizes the manner in which the lens modulates the light waves; hence, the eye has a modulation transfer function that describes the lens [73]. An ideal lens could transfer all details of an object to an image without any variation. So, the ideal lens produces an image, which represents the object exactly.

5.2.1 Modulation transform function (MTF)

Modulation Transfer Function (MTF) is an analysis showing the relationship between the contrast transfer coefficients of the system and the number of line pairs (or spatial frequency: cycles/*mm*) in the image. MTF is extremely useful because we can compare the performance of imperfect optical systems with the curve for a perfect system. The curve for an imperfect system generally lies below the ideal MTF curve. This means that for the same *resolution* the image contrast of the imperfect system is lower than that of a perfect system. However, resolution is a quantity without a standardized definition. We can define it as the *separation*, either in object-space angle or in image-plane distance, for which two discrete point targets can be easily discerned. Resolution can be specified in the spatial frequency domain as the inverse of this separation [63,68]. Since the MTF of a real system is the accumulation of both diffraction effects and various aberrations, it gives information about the magnitude of the image aberrations.

A bar target is an object which is used to test the performance of an optical system. A bar target consists of a series of alternating 'light and dark bars', which have equal width with sharp boundaries, as shown in Figure 5.4 (a). Figure 5.4 (b) shows that if the pattern of the bars is repeated every x *mm* (1 period), then the pattern has a frequency of $1/x$ lines per *mm* ($line/mm$). Such pattern is a "square wave".

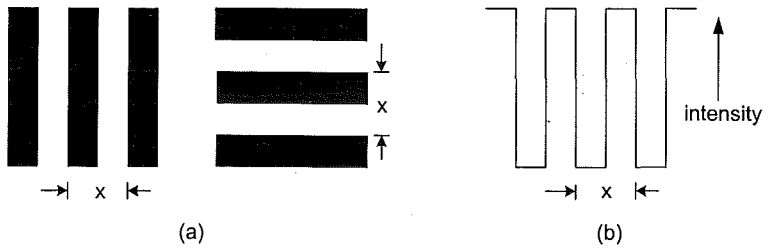

Figure 5.4 Typical bar target with corresponding intensity plot

The modulation of object or image can be expressed as the ratio of the difference between its maximum and minimum intensity to the sum of them as shown in the following equation:

$$Modulation \equiv \frac{I_{\max} - I_{\min}}{I_{\max} + I_{\min}} \tag{5.5}$$

where $I_{\max}$ is the maximum intensity of object or image, $I_{\min}$ is the minimum intensity of object or image, respectively. Figure 5.5 shows two different spatial frequencies, square-waves of object brightness and their corresponding sine-waves image illumination. In addition, this figure shows the maximum intensity $I_{\max}$ and minimum intensity $I_{\min}$ of sine-wave image.

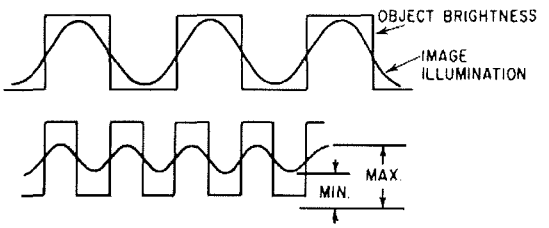

Figure 5.5: Object intensity and its image intensity at two different spatial frequencies [63].

Spread function is what causes a square wave of the object transferring to a sine wave of the image. Figure 5.6 shows how spread function "rounds off" the "corners" of image.

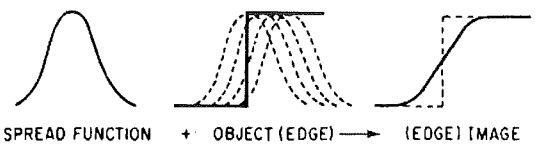

Figure 5.6: A spread function "rounds off" the "corners" of an image [63].

Figure 5.7 shows the intensity pattern for two spatial frequencies and the spatial frequencies varying from low on the top curve to high on the bottom curve. The reason

that it is more difficult to see the lines (or we call it blur) as the pattern becomes smaller is that the apparent change in intensity between the dark and white regions is decreasing as one approaches the limiting resolution of the system. The difference in intensity between the dark and white regions is the same for all frequencies at the object. However, the difference decreases in the image as the spatial frequency increases. The dark regions become lighter and the white regions darker, i.e., the contrast decreases from 90% to 30%. The sharp discontinuities in the object have been rounded off in the image. When the contrast in the image is smaller than the system can detect, the pattern can no longer be resolved.

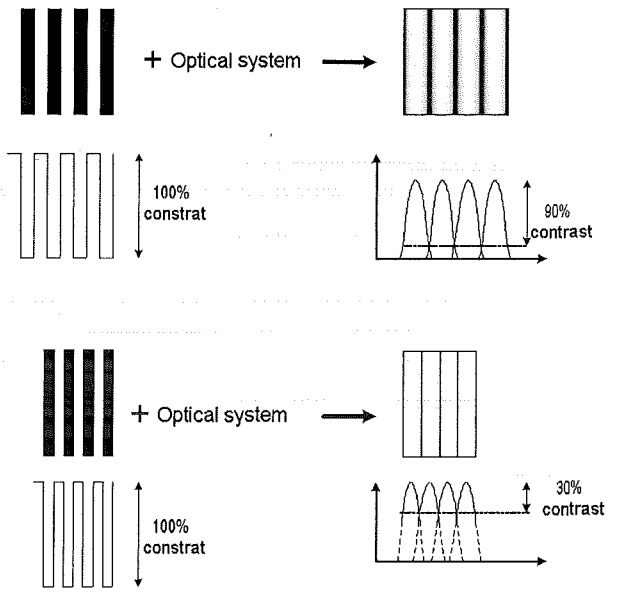

Figure 5.7: Modulation and contrast transfer functions

The modulation transfer function then can be expressed as

$$MTF(\nu) = \frac{M_{image}}{M_{object}} \tag{5.6}$$

where M_{image} and M_{object} are the modulations of image and object at all spatial frequencies (ν) respectively. Resolution is a single-number performance specification, thus, it is more convenient to use than MTF because MTF is a function instead of a single-number. However, MTF provides more complete performance information than is available form simply specifying resolution. This includes information about system performance over a range of spatial frequencies. Figure 5.8 shows two modulation plots of two optical systems (A and B) which have identical limiting resolution but quite different performances at the lower frequencies. System (A) will produce a superior image quality

because greater modulation at the lower frequencies will produce more contrast images. Choosing the system which has better performance would require a specification of the spatial frequency range of interest. A plot of MTF against spatial frequency is an almost universally applicable measure of the performance of an image forming system, and can be applied not only to lenses but to films, image tubes, the eye, and even to complete systems.

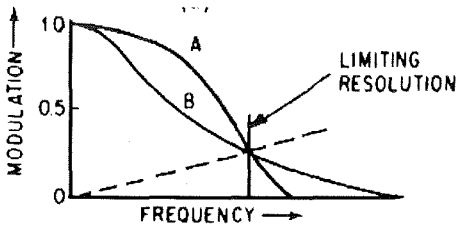

Figure 5.8: The system (A) will produce a superior image than (B), although both have the same limiting resolution [63].

The above discussion is based on square-wave intensity patterns and the square-wave MTFs. If an object pattern has the form of sine-wave, then the intensity distribution in the image will be described by the sine-wave form as well. However, an object with the sine-wave form is difficult to obtain. In general, it is easier to measure an object with square-wave MTF, and then convert the square wave MTF to the sine wave MTF mathematically. The square-wave MTF can be converted to the sine wave MTF using the following equation:

$$\underset{\text{sin}\,wave}{MTF(f_1)} = \frac{\pi}{4}[\underset{sq.wave}{MTF(f_1)} + \frac{1}{3}\underset{sq.wave}{MTF(3f_1)} - \frac{1}{5}\underset{sq.wave}{MTF(5f_1)} + ... + \frac{B_k}{k}\underset{sq.wave}{MTF(kf_1)}] \tag{5.7}$$

where

$$B_k = (-1)^m(-1)^{\frac{k-1}{2}} \quad if\ t = m$$
$$B_k = 0 \quad if\ t < m$$

In the above equation f_1 is frequency (lines/mm), m is the total number of primes into which k can be factored, and t is the number of prime factors in k (1 is not a prime factor). One advantage of using sine-wave MTF is that it can simply multiply the sine-wave MTFs of two or more elements at each frequency to obtain the MTF of the combination.

5.2.2 MTF with a diffraction limited optical system

When aberration for an optical system is small, the interactions between the diffraction effects of the system aperture and the aberrations become very complex. If there are no significant aberrations present in an optical system (aberration free), then this system is termed "diffraction limited".

According to the Rayleigh criterion, an optical system produces a diffraction limited image if the OPD has a maximum absolute value smaller than one fourth of the wavelength [73]. That is because the effects of light diffraction at the pupils limit the spatial frequency response and establish the limits of resolution. Thus, the modulation transfer function is related to the size of the diffraction pattern, which is a function of optical system f-number ($f/\#$) and wavelength (λ) of illumination. The $MTF_{diffraction}$ is the upper limit of the optical system's performance; where the effects of aberrations are assumed to be negligible. Aberrations will increase the spot size and thus contribute to a poor MTF. In quantitative terms, $MTF_{diffraction}$ of a "perfect" circular aperture optical system can be expressed as:

$$MTF(\nu/\nu_0)=\frac{2}{\pi}[\cos^{-1}(\nu/\nu_0)-\nu/\nu_0\sqrt{1-(\nu/\nu_0)^2}] \tag{5.8}$$

where ν_0 is called *cutoff frequency* and it is in cycles per millimeters. The cutoff frequency is a point that the spatial frequency (ν) at which contrast reaches zero. The cutoff frequency is the "limiting resolution" for an aberration free system and it can be expressed by:

$$\nu_0=\frac{1}{\lambda(f/\#)} \tag{5.9}$$

where λ is in millimeters, and $f/\#$ is the relative aperture of the system. In an optical system, spatial frequency (ν) cannot transmit information at a higher spatial frequency than the cutoff frequency (ν_0).

5.2.3 MTF with the optimized layout

According to mathematical theory, the MTF of an optical system is equivalent to the Fourier transform of its spread function. Figure 5.9 illustrates their relationship, where the MTF is the real value of the Optical transfer function (OTF) [74].

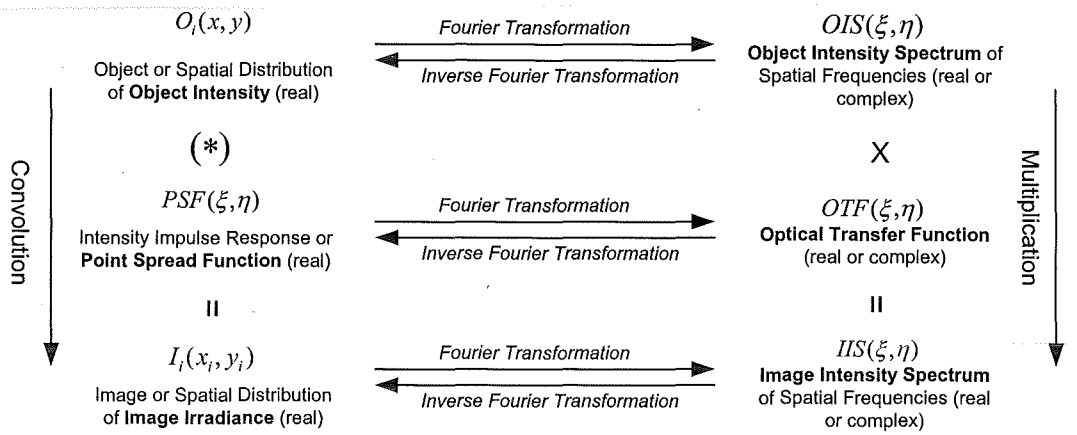

Figure 5.9: The relationship between an object, image and OTF in an optical system [74]

The resulting MTF is the modulation as a function of spatial frequency for a sine-wave object. The Square wave MTF is the modulation response for a square wave target of a specific frequency, as opposed to the response to a sine-wave target for the other plots. The square wave response is computed from the MTF data by using Eq. (5.7). The transmittance of a sine area can be described by the equation [69]:

$$I(x) = t_0 + t_1 \cos 2\pi\nu x + t_2 \cos 4\pi\nu x + t_3 \cos 6\pi\nu x + \ldots\ldots \tag{5.10}$$

where t_0 is a constant, t_1 is the amplitude of fundamental frequency, t_2 , t_3 are the amplitudes of the higher order frequencies, and x is the transmit direction. According to Fourier theory, $I(x)$ repeats itself periodically, so we can express Eq. (5.10) as:

$$I(x) = \frac{1}{2}a_0 + \sum_{n=1}^{\infty}[a_n \cos 2\pi n\nu x + b_n \sin 2\pi n\nu x] \tag{5.11}$$

$$a_n = 2\nu \int_{-1/2f}^{1/2f} I(x) \cos 2\pi n\nu x \, dx \tag{5.12}$$

$$b_n = 2\nu \int_{-1/2f}^{1/2f} I(x) \sin 2\pi n\nu x \, dx \tag{5.13}$$

where $n = 0,1,2,3.....$. For practical purposes, there is no need to go beyond $n = 3$. Using the trigonometric identity $\cos(x-y) = \cos x \cos y + \sin x \sin y$, Eq. (5.11) can be rewritten in the form of

$$I(x) = \frac{1}{2} a_0 + \sum_{n=1}^{\infty} c_n \cos(2\pi n\nu x - \phi_n) \tag{5.14}$$

where $c_n = \pm(a_n^2 + b_n^2)^{1/2}$ and $\phi_n = \tan^{-1}(a_n / b_n)$. MTF data are sampling to a size of the ray grid at the exit pupil. Due to the discontinuous data, rather than performing integration we do a summation. Thus, Eqs. (5.12) and (5.13) will have the forms:

$$a_n = 2\frac{\nu}{m} \sum_{m'-1}^{m} I_{x'} \cos(2\pi nm'\nu) \tag{5.15}$$

$$b_n = 2\frac{\nu}{m} \sum_{m'-1}^{m} I_{x'} \sin(2\pi nm'\nu) \tag{5.16}$$

From Eq. (5.14) we see that if $x = 0$ and $\phi = 0$, then $I_{max} = a_0 + c_1 + c_2 + c_3 + ...$. Likewise, if $x = \pi$ and $\phi = 0$, then $I_{\min} = a_0 - c_1 + c_2 - c_3 + ...$. If we substitute these results into Eq. (5.5), then we arrive at the following result:

$$Modulation = \frac{c_1 + c_3 + ..}{a_0 + c_2 + ..} \tag{5.17}$$

Diffraction MTF computation is based on a fast Fourier transform (FFT) algorithm of the pupil data. The pupil data is sampling a size of the ray grid, i.e., n_x x n_y. Due to the rapid computation of the FFT algorithm, the total of $n_x n_y$ grids requires the order $n_x n_y \log_2 n_x n_y$ complex multiplications and additions. Thus, if the number of samples n_x and n_y are chosen to be powers of 2, then the computation is fastest. Therefore, the sampling may be 32 x 32, 64 x 64, etc. The diffraction calculations are, of course, more accurate as the sampling increases. The sampling of 256 x 256 ray grid is selected to compute in the MTF.

ZEMAX computes $f/\#$ at each wavelength for each field for the tangential and sagittal response separately. By Eq. (5.9) each specific ports of $f/\#$ and the cut frequency v_0 for optimized layout are presented in Table 5.6. The MTF of actual and perfect optical system are plotted as curves in spatial frequency domain, and the entire specific ports are shown in Figures 5.10 ~ 5.15. The upper two curves of these figures represent the tangential and sagittal diffraction-limited MTF value at spatial frequency domain. While the lower two curves represent the diffraction MTF value at spatial frequency domain. These figures show that all ports of the optimized layout have achieved results close to diffraction limited case on the image plane. Because every curve presented in these figures show that the actual optical systems generally lies close to the ideal MTF curve.

Table 5.6: The $f/\#$ and the cut frequency v_0 for the specific ports of the optimized layout

Port	$f/\#$	Cutoff frequency v_0 (cycles/*mm*)
1	1005.7	0.6415
2	998.24	0.6463
3	983.78	0.6558
5	995.77	0.6479
6	981.4	0.6574
9	976.48	0.6607

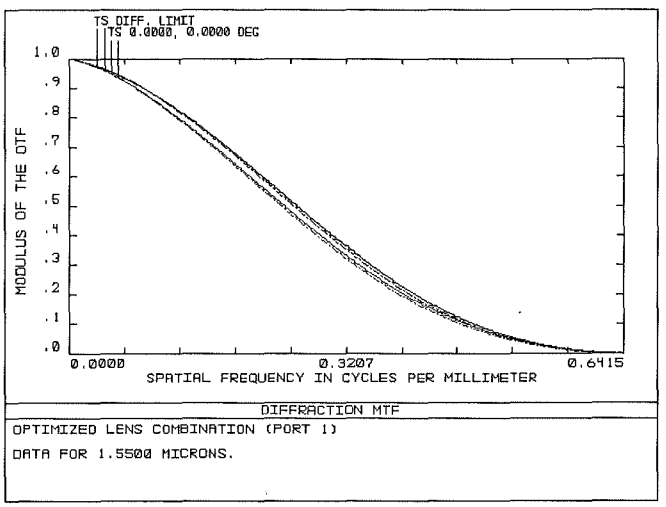

Figure.5.10: MTF of diffraction limited curve with port 1 curve

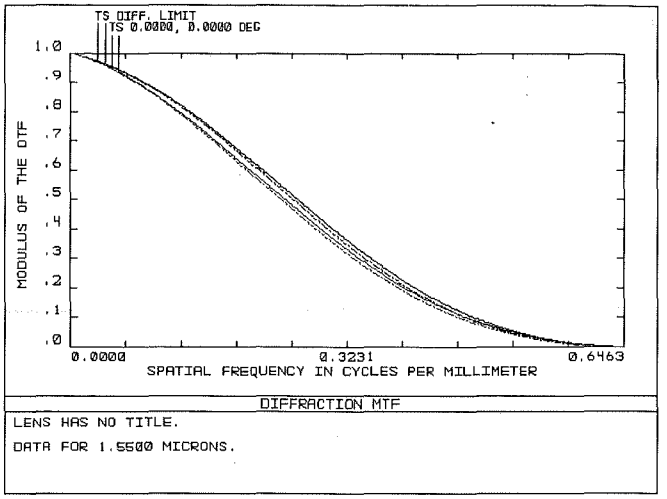

Figure 5.11: MTF of diffraction limited curve with port 2 curve

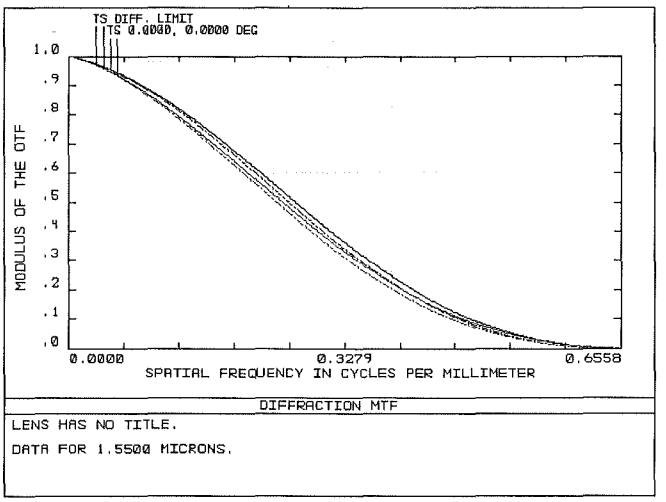

Figure 5.12: MTF of diffraction limited curve with port 3 curve

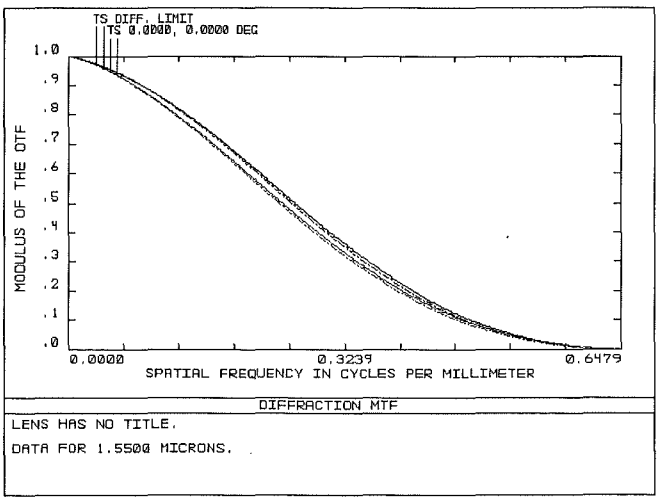

Figure 5.13: MTF of diffraction limited curve with port 5 curve

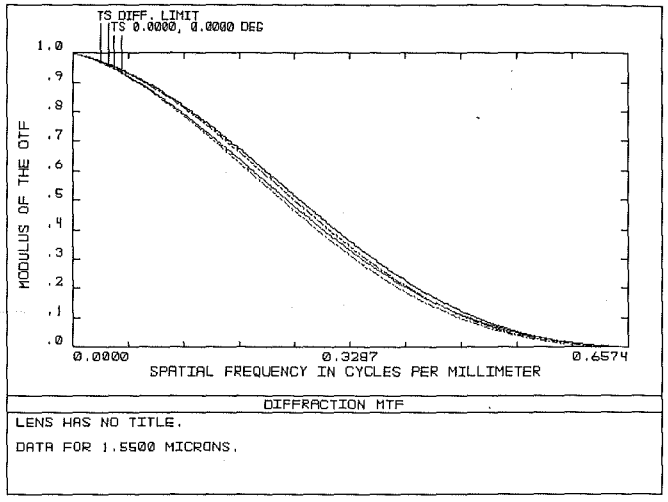

Figure 5.14: MTF of diffraction limited curve with port 6 curve

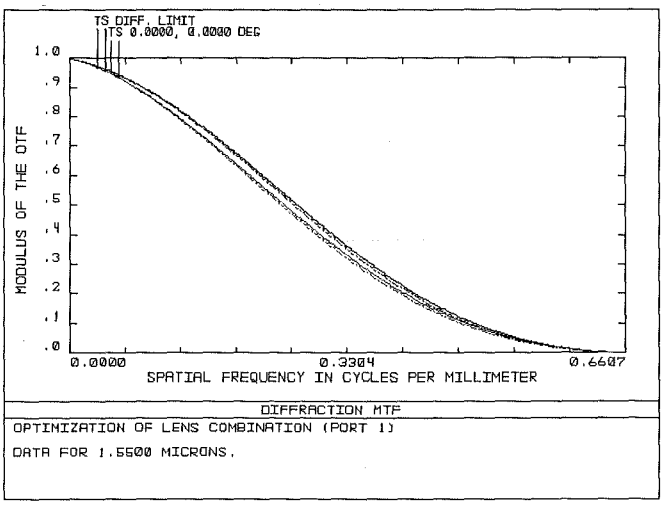

Figure 5.15: MTF of diffraction limited curve with port 9 curve

5.3 Summary

In this chapter, we optimized the Convex–convex layout by modifying the space of first two components, and utilized the MTF to measure the optimized layout. The lens prescription of the optimized optical layout was given. The beam performances and the aberration effects were presented. Also the diffraction limited of the optimized layout was verified.

This layout is successfully converting Gaussian beams from the input fiber array with collimating, aligning, and adequate magnified beam size onto the pixel blocks (these requirements are introduced in Section 3.1.1). The results showed that the averaged beam size is 0.5276 *mm* illuminated on the pixel block. The size of Gaussian beam illuminates on the pixel will cause the clipping ratio of $\gamma = 2.62$. This value is greater than 2.6, which is required to prevent a larger than 0.2 dB coupling power penalty. The dimension of the optimized layout is 332.2 *mm*. This length is acceptable to be a required compact size.

The aberration effects for the optimized layout are improved due to the modification. The results show that the optimized layout has better image forming on the pixel block. Compared to the Convex-convex layout, the optimized layout has decreased up to 10% of the OPD, and 22.7% of the $SphT$, 17.7% of the Δf_A, and 20.6% of the Δh.

The requirement of the beam illuminating the SLM must be diffraction limited is verified by utilizing the MTF. The results show that the system aberrations are close to the diffraction limited case. Therefore, the optimized optical system has achieved the requirement criteria of performance. Finally, the manufacturing tolerances we specified are:

Index of refraction: ± 0.001

Radii of curvature: $\pm 0.02\ mm$

Lens thickness: $\pm 0.025\ mm$

Surface tilt: $\pm 30\ arc\ \sec.$

Light transmission should be greater than 98% at $1550 \pm 30\ nm$ range

Mechanical and optical axes should coincide within 2 arc min.

Chapter 6

Summary

In this thesis, starting from a "Z" configuration free space optical switch using LC SLMs, we investigated an optical system to achieve the performance criteria for the entire input beams illuminating the 1st SLM. The designed optical system was composed of a microlens array and two plano-convex macro-lenses. The performances of the beams' illumination profile on the 1st SLM were analyzed. The results showed that Gaussian beams have the average radius of 0.5276 *mm* on the pixel block. The average OPD for all ports is 0.1515 waves which contains spherical aberration, defocusing and de-centering on the first SLM. The MTF verified that system aberration is close to the diffraction limited case, which means the system has achieved its best performance. The optimized layout has a total length of 332.2 *mm*, this dimension is acceptable for a required compact size switch.

Due to these results, we believe that the optimized optical system meet the requirements of the beam illuminations on the 1st SLM. This chapter summarizes the contributions of this thesis and recommends future research work.

6.1 Contributions of the Thesis

The main contributions of this thesis in brief are:

- The lens design procedures and the modification techniques were efficient in facilitating the design of the optical system to meet the system requirements. In chapter 3 we devised set the procedures for analyzing the system requirements and considering the optical system performance. Therefore, a compact, inexpensive, reliable and low loss switch is realized. We explored the beam clipping ratio on the pixel block, the minimum length required of the system dimension, and considered the optical system performances: beam's collimation, alignment, magnification, and diffraction limited on the first SLM. In order to improve the beam performances and reduce the aberration effects, lens material,

lens surface quality, possible combination of lens shapes, and utilizing a hybrid lens combination (a microlens array and two macro-lenses) were considered.

- Microlens array is a useful optical component that efficiently collimates beams emitting from a single-mode-fiber array into free space. The computation of the microlens' focal length is related to the beam size emitting from the single-mode-fiber into free space and the beam magnification we design. The design of microlens has the plano-convex surfaces. The convex surface facing the input fiber will perform better beam collimation than the plane surface.

- Concave lenses with a large air space utilized with Gaussian beam will cause system to have poor performance. The results showed that beam illumination spread outside the pixel blocks due to the magnification introduced by the concave lenses in the Concave-convex layout and the Concave-achromatic doublet layout. In addition, these two layouts have the average power losses of 0.474 dB and 0.4683 dB respectively. Reducing the distance between the two lenses or putting one more positive lens to collimate the over-divergent light can solve this problem.

- The modification technique for moving the stop position of the optical system successfully optimizes the optical system. Moving the stop position of the optical system was achieved by adjusting the distance between the microlens and the first macro-lens. The results showed that the precise magnification of beam size illuminating the pixel block, and improved aberration effects on the first SLM as well.

- Finally, the Modulation Transfer Function (MTF) was utilized to confirm that the optimized optical system performed a near diffraction limited case. Due to the fact that diffraction limited MTF is the upper limit for any optical system performance, no optical system can perform better than its diffraction limited MTF. Therefore, MTF can compare the curve for an imperfect system (with aberration) with the curve for a perfect system (diffraction limited). The MTF results showed that the optimized optical system performed with close to diffraction limited condition. Thus, the incident illuminating can avoid producing noise from the diffraction at the edge of the hologram aperture on the first SLM.

6.2 *Future Work*

In this section, we propose some research areas where the work presented in this thesis can be extended in terms of theory and applications. Firstly, we consider two possible factors which may influence system performance. They are wavelength sensitivity and non-uniformities in microlens array. Although the optimized optical system has achieved the requirements specified, these two factors may affect the performance in practice. Secondly, a possible future research project is to design a compact lens system in IROS. Although two macrolenses can be found in market catalogs to reduce the cost, the size of the lenses will lead to difficulty of system assembly.

6.2.1 Future work on two sensitivity factors for the optical system

Wavelength sensitivity is an important consideration in the design of optical system. Since the bandwidth in optical telecommunication transmission is 1550 ± 30 nm, light with different wavelength will cause different refraction angle in the optical system. Thus, the actual beam size on the SLM will become uncertain. The varying beam size on SLM will directly affect the clipping ratio on the pixel block, and the coupling efficiency on output fiber. Therefore, an extension of this research maybe to design the optical lens arrangement in such a way that light signals within the bandwidth of the system won't affect the performance of the SLM.

The surface uniformity of each microlens on the microlens array is another sensitive factor. Although we applied the hybrid approach to reduce the critical requirements of microlens quality, non-uniformity of microlenses will affect the system performance to some extent. However, it is very difficult to measure the spherical uniformity of each lens, because of its tiny size. Non-uniformity of the microlenses will introduce different levels and types of aberration and misalignment in IROS. Therefore, possible future research may consider the design of lens systems that are insensitive to such non-uniformities. Typically, the method to test and measure the aberrations of microlens array utilizes Mach-Zehnder interferometer. The scheme of the Mach-Zehnder interferometer is shown in Figure 6.1 [68]. In the test procedure, a micro-objective produces a spherical wavefront, and the microlens being tested collimates into a plane wave deformed by the reference arm and the wavefront of the test arm yields the interferogram of the wave aberrations. Based on these measurements, the coefficients of the aberration polynomials can be calculated.

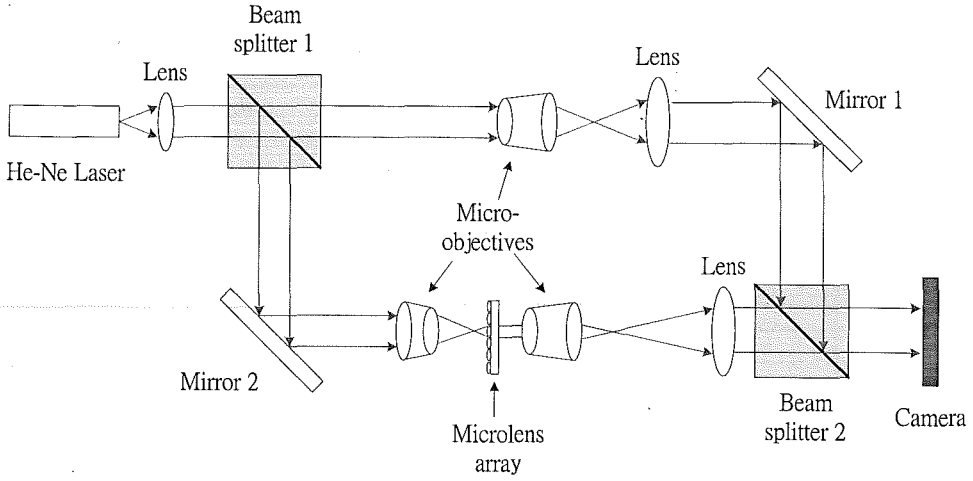

Figure 6.1: The scheme of the Mach-Zehnder interferometer [68].

6.2.2 Future work on compact design of optical systems

Another possible future work is to design a compact optical system instead of using two macro-lenses. The design of our optical system is based on the paraxial theory. That is, beams propagate in the paraxial region. For this reason, the two macro-lenses are designed as bulk. Therefore, beams propagate in an infinite-like aperture of the lens system, so that the diffraction limited can be achieved on the image plane.

However, utilizing the bulk lenses will cause the challenge of assembling two optical systems in the area of close to 1st SLM in the "Z" configuration. Therefore, possible future research may be to design an optical system with smaller lens size. We can design a low f-number lens system, which has the same performance as we require, avoiding the use of bulk lenses. For example, we can combine two objectives lenses; one is an afocal system and the other is a Petzval lens or a Double Gauss lens. The function of afocal system is similar to a beam expander as shown in Figure 6.2 [75].

Since there are essentially two thin lenses separated by a large distance, as a preliminary design we shape each lens for minimum spherical aberration. The purpose of a Petzval lens or double Gaussian lens is to form a long focal length and diffraction limited image quality. A Petzval lens consists of two positive members separated by a large distance of perhaps half the focal length of the lens [76]. This can be constructed economically and can yield low f-number [63]. The double Gaussian lens is usually used in a telescope. It is also similar to anastigmatic photographic lenses and consists of a nearly symmetric arrangement of elements about a central stop. Surrounding this stop are two "achromats" with the flint element facing the stop, such that its surface is concave toward the stop [76].

To reduce the f-number, additional elements are generally added in the front and rear. These two layouts are shown in Figure 6.3 and Figure 6.4 respectively [75].

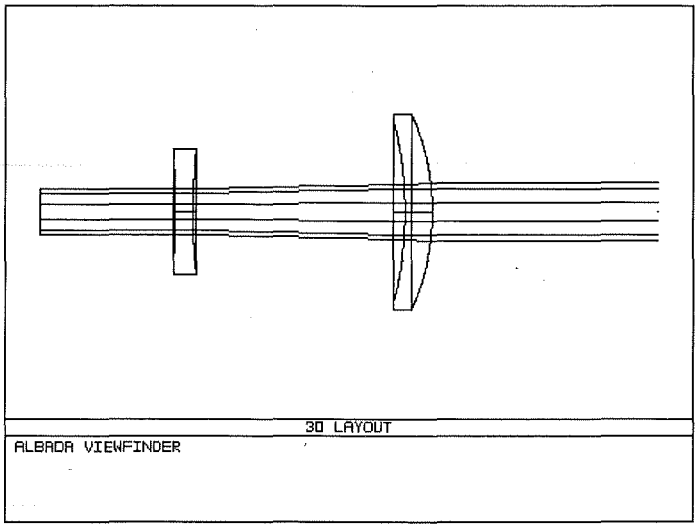

Figure 6.2: The configuration of an Afocal system from [75].

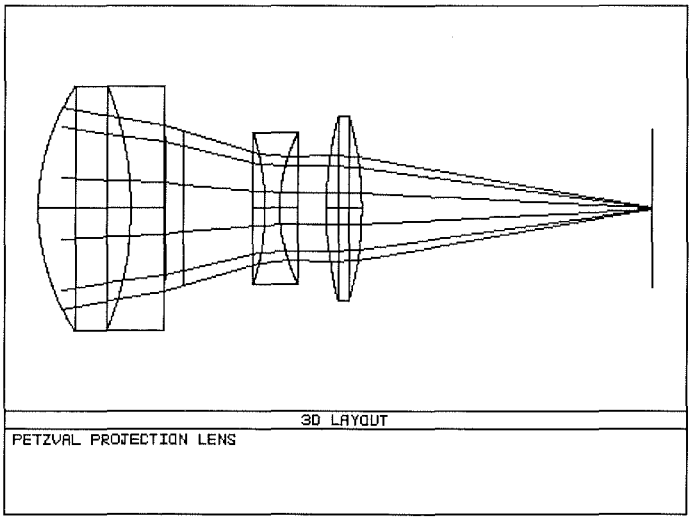

Figure 6.3: The configuration of a Petzval lens from [75].

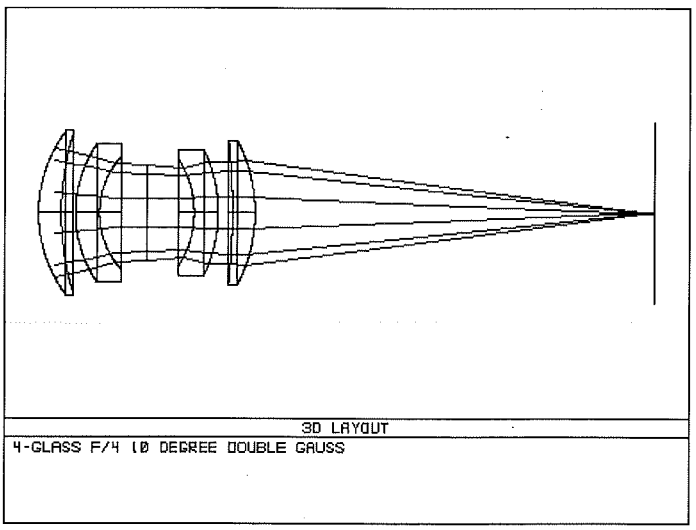

Figure 6.4: The configuration of a Double Gauss lens from [75].

Appendix A

The five primary aberrations are spherical aberration, coma, astigmatism, field curvature and distortion. They are described as fellow:

Spherical Aberration

Spherical aberration is formed by lenses made with spherical surfaces and rays, which are parallel to the optic axis but at different distances from the optic axis, fail to converge to the same point, as illustrated in Figure A.1.

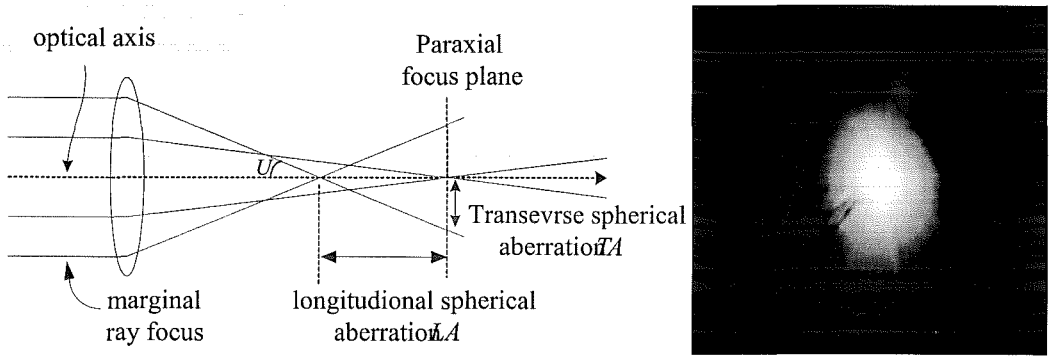

Figure A.1: A lens makes spherical aberration on the paraxial focus plane, right picture is from [53]

Figure A.1 shows rays from farther to near the optical axis pass through the lens and then focus across the optical axis. *Longitudinal spherical aberration* (LA) is the distance along the optical axis between the intercept of the rays that are nearly on the optical axis (*paraxial rays*) and the rays that go through the edge of the lens (*marginal rays*). *Transverse spherical aberration* (TA) is the height at which these rays intercept the paraxial focal plane. These two quantities are related by

$$\tan U = \frac{TA}{LA}$$

Spherical aberration can be minimized by bending the lens surface for a single lens. Alternatively, by combining multiple lenses or overcorrecting some elements can reduce spherical aberrations, i.e. the use of symmetric doublets greatly reduces spherical aberration.

Coma

Coma is caused by rays from an off-axis point of light in the object plane to create a trailing "comet-like" blur directed away from the optic axis. The reason is different parts of lens surface exhibit different degrees of magnification in a spherical lens, as shown in Figure A.2. So that coma may produce a sharp image in the center of the field, but become increasingly blurred toward the edges. Coma can be partially corrected by bending the lens surface for a single lens. More complete correction can be achieved by using a combination of lenses symmetric about a central stop.

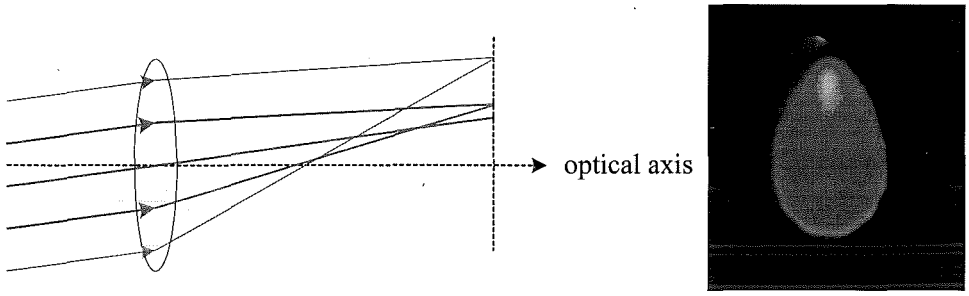

Figure A.2: Positive transverse coma, right picture is from [53]

Astigmatism

The natural asymmetry leads to astigmatism when an off-axis object is focused by a spherical lens. The system appears two different focal planes as is shown in Figure A.3. One is *tangential plane*, which containing both optical axis and object point. The other is *sagittal plane*, which perpendiculars to the tangential plane and contains the chief ray. The chief, or principal, ray goes from the object point through the center of the aperture of the lens system. The figure illustrates that tangential rays from the object come to a focus closer to the lens than do rays in the sagittal plane. When the image is evaluated at the tangential conjugate, we see a line in the sagittal direction. A line in the tangential direction is formed at the sagittal conjugate. Between these conjugates, the image is either an elliptical or a circular blur. The amount of astigmatism in a lens depends on lens shape only when there is an aperture in the system that is not in contact with the lens itself.

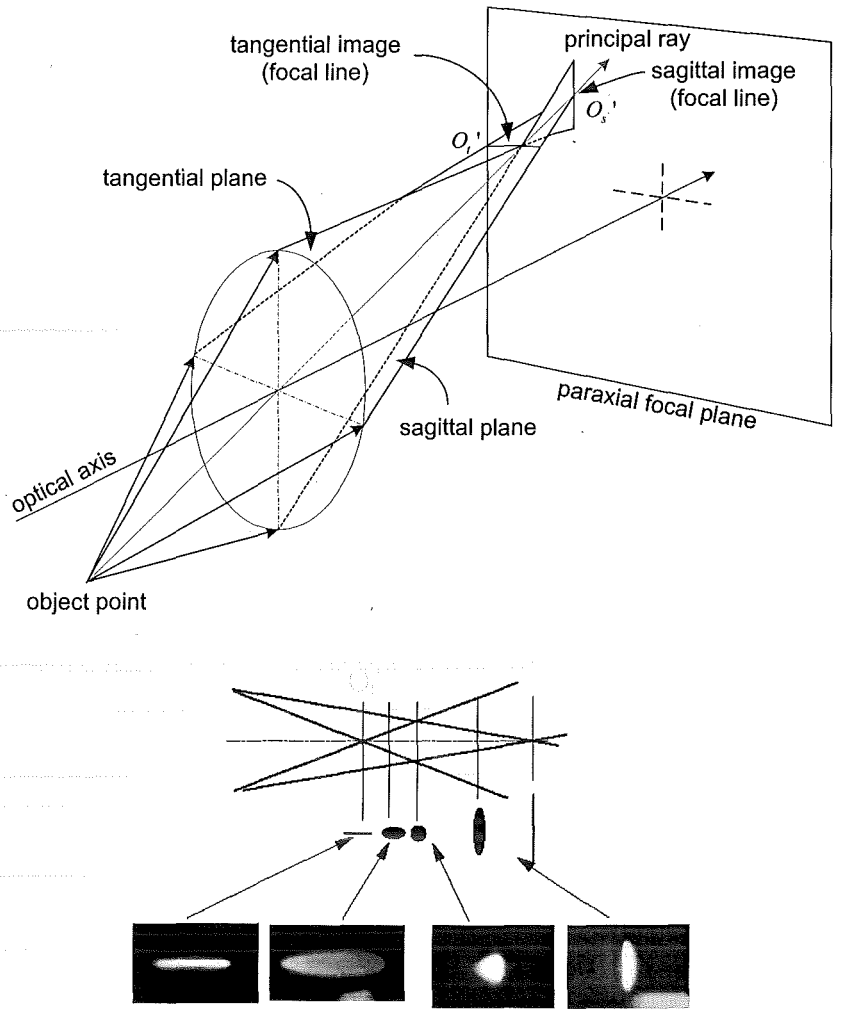

Figure A.3: Astigmatism represented by sectional views [53]

Field Curvature

There is a tendency of optical systems to image better on curved surfaces than on flat planes even in the absence of astigmatism. This effect is called field curvature as shown in Figure A.4. Field curvature causes a planar object to project a curved (nonplanar) image. Positive lens elements usually have inward curving fields, and negative lenses have outward curving fields. Field curvature can thus be corrected to some extent by combining positive and negative lens elements. In the presence of astigmatism, this problem is compounded because there are two separate astigmatic focal surfaces that correspond to the tangential and sagittal conjugates. Field curvature varies with the square of field angle or the square of image height. Therefore, by reducing the field angle by one-half, it is possible to reduce the blur from field curvature to a value of 0.25 of its original size.

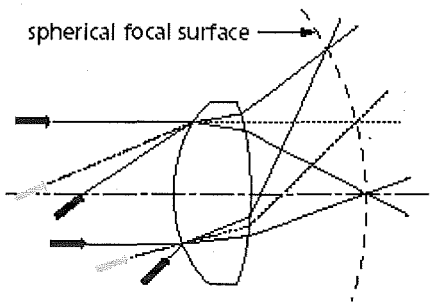

Figure A.4: Field curvature [53]

Distortion

Distortion is a separation of an actual image point from the paraxial predicted location on the image plane. Therefore an image shape does not correspond exactly to the shape of the object. Distortion can be expressed either as an absolute value or as a percentage of the paraxial image height. This may lead to a brief that a lens or lens system has opposite types of distortion depending on whether it is used forward or backward. The amount of distortion usually increases with increasing image height. The effect of this amount can be seen as two different kinds of distortion: *pincushion* and *barrel* distortion as shown in Figure A.5. Distortion is not lower the system resolution, also is different from coma as well.

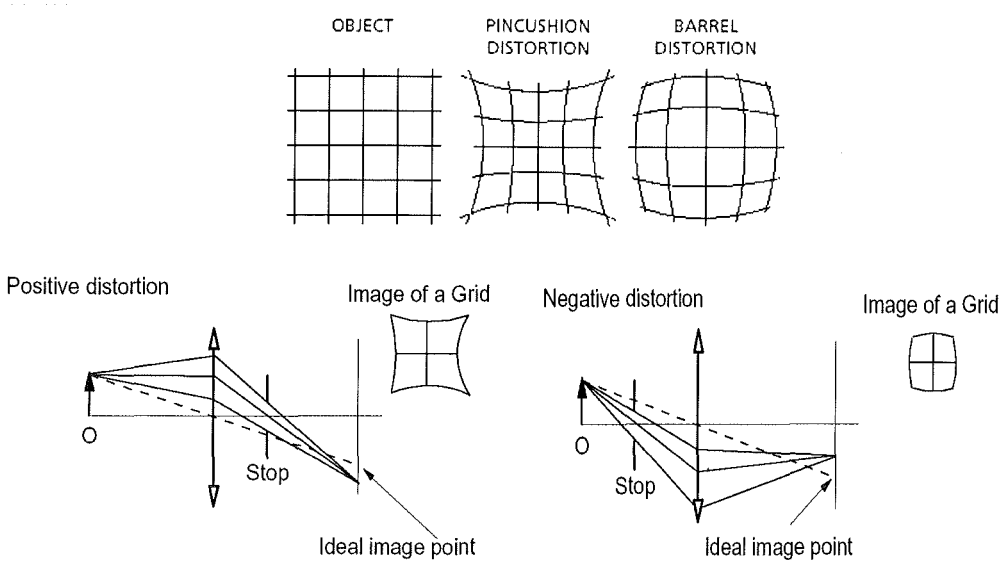

Figure A.5: Pincushion and barrel distortion, from [53]

Appendix B

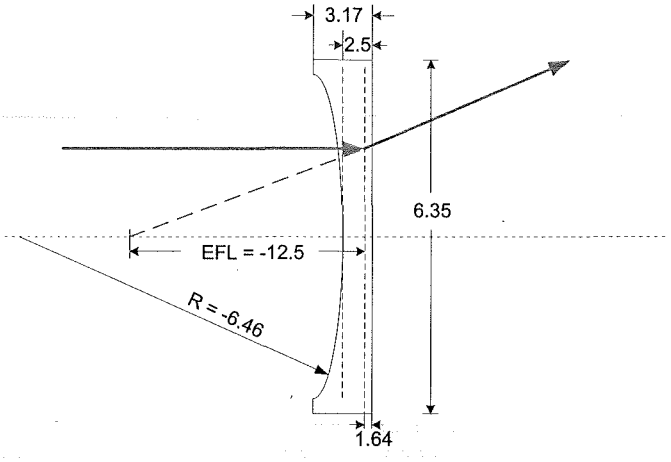

BK7: n = 1.50065204

All the dimension measured in millimeter

Figure B.1: Illustration of a Plano - Concave Lens (KPC013) [70]

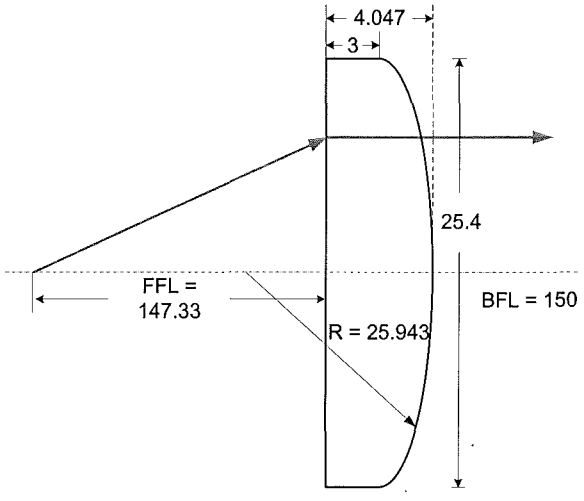

BK7: n = 1.50065204

All the dimension measured in millimeter

Figure B.2: Illustration of a Plano – Convex Lens (KPX100) [70]

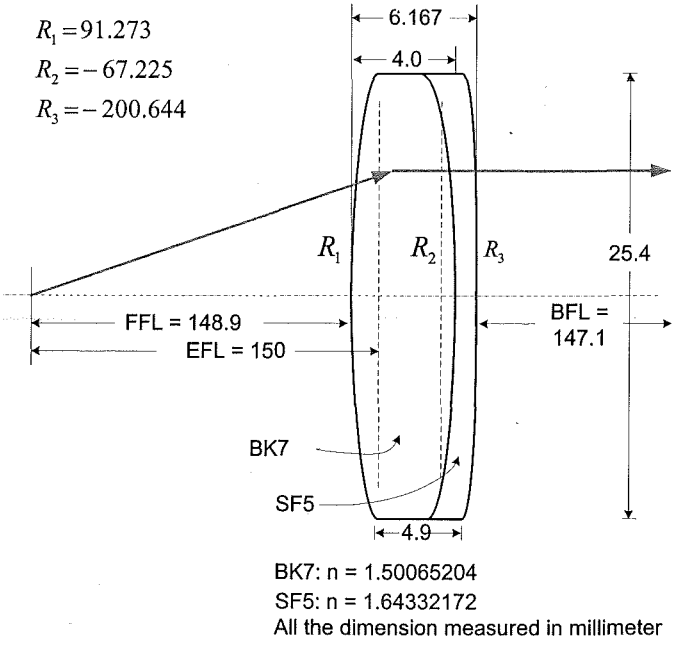

Figure B.3: Illustration of Achromatic doublet (PAC058) [70]

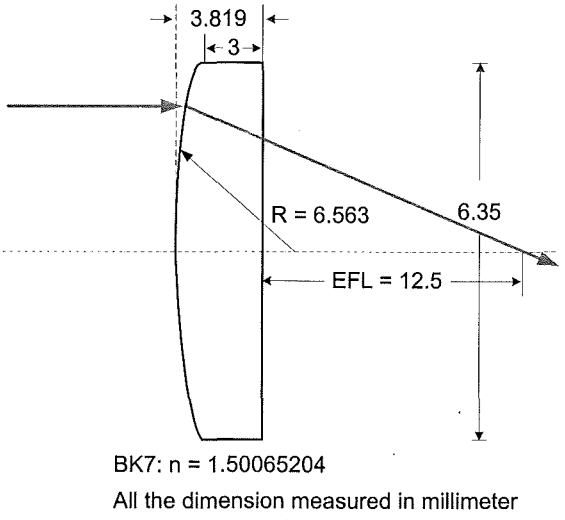

Figure B.4: Illustration of a Plano – Convex Lens (KPX013) [70]

Bibliography

[1] Stamatios V. Kartalopoulos, "Introduction to DWDM Technology", *IEEE press*, Chapter 3, 2000.

[2] Govind P. Agrawal, "Fiber-Optic Communication System", *Wiley Inter science*, 2nd edition, Chapter 1, 1997.

[3] Alex Barros, and Raj Srikanth, "Optical Networking – The final answer", *Deutsche Bank Alex Brown*, U.S., May 2000.

[4] Rajiv R. and Kumar N. S. 'Optical Networks', *Morgan Kaufmann Publishers*, 2nd edition, Chapter 3, 2002.

[5] Stamatios V. Kartalopoulos,"Introduction to DWDM Technology", *IEEE press*, Chapter 10, 2000.

[6] Cisco Systems, Inc. "Introducetion to DWDM Technology", http://www.cisco.com, Chapter 1-3, 2000.

[7] Jaafar M. H. Elmirghani and Hussein T. Mouftah, "Technologies and architectures for scalable dynamic DWDM networks", *IEEE Communications Magazine*, Vol. 38, Issue 2, pp. 58-65, February 2000.

[8] N. A. Jackman, S. H. Patel, B. P. Mikkelsen, and S. K. Korotky, "Optical cross connects for optical networking", *Bell Laboratories Technical Journal*, Vol. 4, pp. 262-281, 1999.

[9] Intelligent Pixel Inc., "IROS: The Intelligent Reconfigurable Optical Switch", Note from *Edith Cowan University*, March 2001.

[10] H. Scott Hinton, "Architectural Considerations for Photonic Switching Networks", *IEEE Journal*, Vol. 6, No. 7, pp. 1209-1226, August 1988.

[11] Wooten, E. L., Kissa, K. M., Yi-Yan, A., Murphy, E. J., Lafaw, D. A., Hallemeier, P. F., Maack, D., Attanasio, D. V., Fritz, D. J., McBrien, G. J., "A review of Lithium Niobate

Modulators for fiber-optic communication systems", *IEEE Journal in Quantum Electronics*, Vol. 6, No. 1, pp. 69-82, February 2000.

[12] Arjun Kar-Roy and Chen S. Tsai, " 8×8 Symmetric Nonblocking Integrated Acoustooptic Space Switch Module on $LiNbO_3$ ", *IEEE Phontonics Technology Letters*, Vol. 4, No. 7, pp. 1041-1135, July 1992.

[13] Krahenbuhl, R.; Kyburz, R.; Vogt, W.; Bachmann, M.; Brenner, T.; Gini, E.; Melchior, H., "Low-loss polarization-insensitive InP-InGaAsP Optical Space Switches for Fiber Optical Communication", *IEEE Photonics Technology Letters*, Vol.8, No. 5, pp. 632-634, 1996.

[14] K. Hamamoto, T. Anan, K. Komatsu, M. Sugimoto and I. Mito, "First 8 × 8 semiconductor optical matrix switches using GaAs/AlGaAs electro-optic guided-wave directional coupler", *Electron Letters*, Vol. 28, No. 5, pp. 441-443, 1992.

[15] Helin, P.; Bourouina, T.; Mita, M.; Reyne, G.; Fujita, H. "Free Space Micromachined Optical Switches with Submillisecond Switching Time for Large-Scale Optical Cross-connects". *IEEE Photonics Technology Letters*, Vol. 10, No. 4, April 1998.

[16] John Barthel and Tom Chuh, "Optical Switches enable dynamic optical add/drop modules", *Penn Well Corporation*, August 2001.

[17] John Barthel and Tom Chuh, "Matrix Optical Switches enable Wavelength-selective Crossconnects", *Penn Well Corporation*, August 2001.

[18] Hagelin, P. M., Krishnamoorthy, U., Heritage, J. P., Solgaard, O. "Scalable optical cross-connect switch using micromachined mirrors". *IEEE Photonics Technology Letters*, Vol.12, No.7, July 2000.

[19] Peter De Dobbelaere , Ken Falta, Li Fan, Steffen Gloeckner and Susant Patra, OMM Inc, "Digital MEMS for Optical Switching", *IEEE communications*, Vol. 40, No. 3, pp. 88-95, March 2002.

[20] Patrick B. Chu, *et al*, Tellium Inc, "MEMS: The path to Large Optical Crossconnects", *IEEE communications*, Vol. 40, No. 3, pp. 80-87, March 2002.

[21] David J. Bishop, C. Randy Giles, and Gray P. Austin, Lucent Technologies, "The Lucent LambdaRouter: MEMS Technology of the Future Here Today", *IEEE Communications*, Vol. 40, No. 3, pp. 75-79, March 2002.

[22] Crossland, W. A., Manolis, I. G., Redmond, M. M.; Tan, K., Wilkinson, T. D., Chu, A., Handerek, V. A., Holmes, M. J., Parker, T., Bonas, I. G., Robertson, B., Warr, S. T., Stace, C., White, H. J., Woolley, R. A., Henshall, G., Reconfigurable Optical Switches for aerospace and telecommunications Systems (ROSES), "Holographic Optical Switching: The 'ROSES' demonstrator". *Journal of Lightwave Technology*, Vol. 18, No. 12, pp. 1845 -1854, Dec 2000.

[23] W. A. Crossland, K. L. Tan, I. G. Manolis, M. M. Redmond, T. D. Walkson, G. Henshall, R. A. Woolley, C. Stace, H. J. White, and S. T. Warr, "Beam Steering Optical Switches using LCOS: The "ROSES" Demonstrator", *IEE,* Savoy Place, LondonWC2R 0BL, UK, 2000.

[24] T. D. Wilkinson, W. A. Crossland, R. J. Mears, and D. C. O'Brien, "Dynamic holographic interconnects that use ferroelectric liquid-crystal spatial light modulators", Applied Optics, Vol. 33, No. 14, pp. 2795-2803, May 1994.

[25] R. Moignard, Y. Defosse, "Single-mode fiber optical crossbar routing switch with ferroelectric liquid-crystal-VLSI technology and free-space optics", *Applied Optics*, Vol. 36, No. 17, pp. 3866-3876, June 1997.

[26] Hirofumi Y. and Masayasu Y. "4X4 free-space optical switching using real-time binary phase-only holograms generated by a liquid-crystal display", *Optics Letters*, Vol. 16, No. 18, pp. 1415-1417, September 1991.

[27] K. M. Johnson, D. J. McKnight, and I. Underwood, "Smart Spatial Light Modulators Using Liquid Crystal On Silicon", *IEEE Journal of Quantum Electronics*, Vol. 29, pp. 699-714, 1993.

[28] H. S. Hinton, "Progress in Smart Pixel Technologies", *IEEE Journal of Selected Topics in Quantum Electronics*, Vol. 2, pp. 14-23, 1996.

[29] G. Moddel, K. M. Johnson, W. Li, R. A. Rice, L. A. Pagano-Stauffer, and M. A. Handschy, "High-speed binary optically addressed spatial light modulator," *Applied Physics Letter*, Vol. 55, pp. 537-539, 1989.

[30] Yves-Alain Peter, "Micro-optical fiber switch for a large number of interconnects", PhD Thesis, *University of Neuchatel*, Chapter 3, January 2001.

[31] J. N. Lee, "Optical Modulators", in Handbook of Photonics, Gupta, M. C., Boca Raton: CRC Press, pp. 393-434, 1997.

[32] P. M. Alt, "Single-Crystal Silicon for High Resolution Display," Proceedings of the 1997 International Display Research Conference, Society for Information Display, Toronto, pp. M-19, September 1997.

[33] K. E. Alameh, S. Ahderom, M. Raisi, K. Lo, and R. Mavaddat, Opto-VLSI, "Applications of Liquid Crystal Spatial Light Modulators in Optical Communications", Note from *Edith Cowan University*, May 2002.

[34] Crossland, W. A., Redmond, M. M., Wilkinson, T. D., Robertson, B., Warr, S. T., "High Tilt Angle FLC SLM for Optical Interconnection". *IEE, Savoy Place*, London WC2R 0BL, UK, 2000.

[35] W. A. Crossland, T. D. Wilkinson, I. G. Manolis, M. M. Redmaond, and A. B. Davey, "Telecommunications applications of LCOS devices", In proceedings, 9th International Topical Meeting on Optics of Liquid Crystals, OLC, 2001.

[36] J. A. Breslin, J. K. Low, I. Underwood, "Smart pixel with four level amplitude or phase modulation", Digest of the LEOS Summer Topical Meetings - Smart Pixels, pp. 33-34, 1998.

[37] H. Dammann, "Spectral characteristics of stepped-phase gratings", *Optics*, Vol. 53, pp. 409-417, 1979.

[38] Kim L. Tan, Stephen T. Warr, Brian Robertson, Ilias G. Manolis, Timothy D. Wilkinson, Maura M. Redmond, William A. Crossland, and Robert J. Mears, "Dynamic Holography for optical Interconnections. II. Routing holograms with predictable location and intensity of each diffraction order", *Journal of the Optical Society of America*, Vol. 18, pp. 205-215, 2001.

[39] B. Fracasso, "In Proceedings, OSA Photonics in Switching Meeting", *Monterey*, CA, paper PThB3, July 2001.

[40] F. B. McCormick, "Free-Space Interconnection Techniques", *AT&T Bell Laboratories*, Photonics in Switching, Volume II, Chapter 4, 1993.

[41] McCormick, F. B., F. A. P. Tooley, J. L. Brubaker J. M. Sasian, "Optomechanics of a free space switch: the syste", *Proc SPIE,* Optomechamics and Dimensional Stability 1533, pp. 97-114, 1991.

[42] F. A. P. Tooley, S. M. Prince, M. R. Taghizadeh, F. B. McCormick, M. W. Derstine, and S. Wakelin "Implementation of a Hybrid Lens", *Applied Optics*, Vol. 34, No.28, October 1995.

[43] McCormick F. B., F. A. P. Tooley, J. L. Brubaker, T. J. Cloonan, A. L. Lentine, R. L. Morrison, S. J. Hinterlong, M. J. Herron, S. L. Walker, and J. M. Sasian, "Experimental investigation of a free space optical switching network using S-SEEDs", *Apply Optics*, Vol. 31 No. 26, pp. 5431-5446, 1992.

[44] Lohmann, A. W. "Scaling laws for lens systems", *Applied Optics*, Vol. 28, No. 23, pp. 4996-4998, 1989.

[45] F. B. McCormick, F. A. P. Tooley, T. J. Cloonan, J. L. Brubaker, A. L. Lentine, R. L. Morrison, S. J. Hinterlong, M. J. Herron, S. L. Walker, and J. M. Sasian, "S-SEED-Based Photonic Switching Network Demonstration", *AT&T Bell Laboratories*, Naperville, Illinois 60566, pp. 48-55, 1997

[46] Kawai, S. "Free space multi-stage optical interconnection networks using micro lens arrays", *Top Meeting on Photonics Switching, Kobe, Japan, Institute of Electronics, Information, and Communication Engineers, paper* 14D-1, 1990.

[47] Restall, E. J., B. Robertson, M. R. Taghizadeh, and A. C. Walker, "Two dimensional spatially variant optical interconnects", *Optical Computing* 1991, Technical Digest Series, *Optical Society of America*, Washington DC, Vol. 6, pp. 49-52, 1991.

[48] M. R. Taghizadeh and J. Turuen, "Syntheic diffractive elements for optical interconnection", *Optics Compute Process* 2, pp. 221-242, 1992.

[49] M. C. Hutley, P. Savander, and M. Schrader, "The use of microlenses for making spatially variant optical interconnections", *JEOS Pure Applied Optics* 1, pp. 337-346, 1992.

[50] A. Lohmann, "Image formation of dilute arrays for optical information processing", *Optics Communications,* Vol. 86, pp. 365-370, 1991.

[51] T. D. Wilksion, "Outline optical switch design", Note from *Edith Cowan University*, December 2000.

[52] Bahaa E. A. Saleh, Malvin Carl Teich, "Fundamentals of Photonics", *Wiley & Sons, Inc.* chapter 3, 1991.

[53] Melles Griot, "Fundamental Optics", *Melles Griot Inc.*, www.mellesgriot.com, 2000.

[54] D. Marcuse, "Loss Analysis of Single-Mode Fiber Splices", *Bell System Technical Journa*l, Vol. 56, No. 5, pp. 703-718, May-June 1977.

[55] Gerd Keiser, "Optical Fiber Communications", *McGraw-Hill Inc.*, 2nd edition, Chapter 2, 1991.

[56] Haiyin Sun, "Thin lens equation for a real laser beam with weak lens aperture truncation", *Optics Engineering*, Vol. 37, No. 11, pp. 2906-2913, 1998.

[57] P. Belland and J. P. Crenn, "Changes in the Characteristics of a Gaussian Beam Weakly Diffracted by a Circular Aperture", *Applied Optics*, Vol. 21, No. 3, pp. 522-527, February 1982.

[58] Haiyin Sun, "Thin Lens Equation for a Real Laser Beam with Weak Lens Aperture Truncation", Optics Engineering, Vol. 37, No. 11, pp. 1906-1913, November 1998.

[59] Sidney. A. Self, "Focusing of Spherical Gaussian Beams", *Applied Optics*, Vol. 22, No. 5, pp. 658-661, March 1983.

[60] Daniel M., Zacarias M., "Handbook of Lens Design", *Marcel Dekker Inc.*, Chapter 9, 1994.

[61] Rayces, J. L., "Exact Relation Between Wave Aberration and Ray Aberration", *Optica Acta*, 11, pp. 85-88, 1964.

[62] Eugene Hecht, Adelphi University, "Optics", *Wesley Longman, Inc.* 3rd edition, chapter 6, 1998.

[63] Warren J. Smith, "Modern Optical Engineering", *McGraw-Hill, Inc.* 3rd Edition, Chap 15, 2000.

[64] Daniel J. Reiley and Jose M. Sasian, "Optical Design of a Free-Space Photonic Switching System", *Applied Optics*, Vol. 36, No. 19, pp. 4497-4504, July 1997.

[65] Stephen Thomas W., "Free-Space Switching for Optical Fiber Networks", PhD thesis, *Christ's College, Cambridge*, July 1996.

[66] Kim L. Tan, William A. Crossland, and Robert J. Mears, "Dynamic Holography for optical Interconnections I. Noise floor of Low-cross-talk holographic Switches". *Journal of the Optical Society of America*, Vol. 18, No. 1, pp. 195 – 205, January 2001.

[67] E. G. Churin, P. Bayvel, J. E. Midwinter and A. M. Hill "The Influence of Aperture Size and Shape on Crosstalk Level in Free-Space Grating Demultiplexers for WDM Networks". *IEEE Photonics Technology Letters*, Vol. 8, No. 10, pp. 1337 – 1339, October 1996.

[68] Warren J. Smith, Genesee Optics Software, Inc. "Modern Lens Design", *McGraw-Hill, Inc.*, Chap 2, 1992.

[69] *ZEMAX*, Optical Design Program, Version 10, *Focus Software, Inc.* Jun 2002.

[70] *Newport Inc*, "Photonics Fiber Optics", http://www.newport.com, 2002.

[71] Stenfan Haselbeck, Horst Schreiber, Johannes Schwider, and Norert Streibl, "Microlenses fabricated by melting a photoresist on a base layer", *Optical Engineering*, Vol. 32, No. 6, pp. 1322-1324, June 1993.

[72] Zoran D. Popovic, Robert A. Sprague, and G. A. Neville Connell, "Technique for Monolithic Fabrication of Microlens Arrays", *Applied Optics*, Vol. 27, No. 7, pp. 1281-1284, April 1988.

[73] Kenneth R. Spring, and Michael W. Davidson, "Modulation Transfer Function", http://www.microscopyu.com/articles/optics/mtfintro.html, October 2001.

[74] Raymond G. Wilson, "Fourier Series and Optical Transform Techniques in Contemporary Optics", *Wiley Inter Science Inc.*, Chapter 6, 1995.

[75] *ZEBASE*, Optical Design Program, Version 4, *Focus Software, Inc.*, January 1999.

[76] Milton Laikin, 'Lens Design', *Marcel Dekker, Inc.*, 1995.